Computational study of the role of coordinated ligand architecture on the oxidation reactions catalysed by transition metal-based complexes

A thesis submitted

in the partial fulfilment for the award of degree of

Doctor of Philosophy

Submitted By

Lovleen Kaur (902009011)

Under the supervision of

Dr. Debasish Mandal

(Assistant Professor)

Department of Chemistry and Biochemistry

Thapar Institute of Engineering and Technology

Patiala-147004

Certificate

This is to certify that thesis entitled "**Computational study of the role of coordinated ligand architecture on the oxidation reactions catalysed by transition metal-based complexes**", is being submitted by **Ms. Lovleen Kaur** in fulfilment of the requirement for the award of the Degree of Doctor of Philosophy in the Department of Chemistry and Biochemistry, Thapar Institute of Engineering and Technology, Patiala, is a record of candidate's own independent and original research work carried out by her under my supervision and guidance. The matter presented in the thesis has not been submitted in part or full for the award of any degree in any other University or Institute.

Dr Debasish Mandal

(Supervisor)

Assistant Professor

DCBC

TIET, Patiala

Head:

Dr. Manmohan Chhibber

Professor and Head

DCBC

TIET, Patiala

Candidate's Declaration

I, hereby declare that the work presented in the thesis entitled "**Computational study of the role of coordinated ligand architecture on the oxidation reactions catalysed by transition metal-based complexes**", in fulfilment of the requirement for the award of the Degree of Doctor of Philosophy in the Department of Chemistry and Biochemistry, Thapar Institute of Engineering and Technology, Patiala, is a record of my work carried out under the supervision of Dr Debasish Mandal, Assistant Professor, Department of Chemistry and Biochemistry, Thapar Institute of Engineering and Technology, Patiala, India. The matter presented in the thesis has not been submitted in part or full for the award of any degree in India or abroad.

Lovleen Kaur

Lovleen Kaur

This thesis is dedicated to my husband

Harsimran Singh Gill

Acknowledgements

I would like to extend my deepest gratitude to my guide, Dr. Debasish Mandal, for his unwavering support, invaluable guidance, and constant encouragement throughout my research. His expertise and dedication have been instrumental in the completion of this thesis.

I sincerely acknowledge Dr. Padmakumar Nair, Honourable Director, Dr. N. Tejo Prakash, Dean of Research and Development Centre (DoRDC), and Dr. Bhupendrakumar Chudasama, Associate dean RDC, T.I.E.T, Patiala,for providing all the necessary facilities that have been immensely helpful in carrying out this research.

My sincere appreciation to Dr. Manmohan Chhibber, Professor and Head, Department of Chemistry and Biochemistry, Thapar Institute of Engineering and Technology, Patiala for his ever-helping attitude and encouragement.

I extend my deep sense of gratitude to my doctoral committee members Dr. Amjad Ali, Dr. Bhupesh Goyal, and Dr Dheeraj Kumar Singh for their valuable suggestions and discussions that helped me in my research work.

I am profoundly grateful to my parents, Lakhwinder Singh and Manpreet Kaur, for their endless love, sacrifices, and encouragement. Their belief in me has been a source of strength and motivation. My heartfelt thanks go to my in-laws, Harpreet Singh and Nardeep Kaur, for their support and understanding. Their kindness and encouragement have been a significant part of my journey. Special thanks to my siblings, Arshdeep and Avneet, for their constant support and encouragement. Their presence and camaraderie have been invaluable. I would also like to thank my aunt, Rajwant Kaur, for her care and support during my time of need. Her compassion and assistance have been deeply appreciated.

I am grateful to my labmates, Akanksha Katoch, Amanpreet Kaur, Dr. Pooja Soam and Abhinash Mohapatra for their collaboration, support, and

friendship. Their contributions and camaraderie have made the research experience more enjoyable and productive. I would also like to acknowledge my fellow Thaparians, Sukhandeep, Jemini and Pahulpreet, for their friendship and support. Our shared experiences and interactions have enriched my time at TIET. To my friends, Navneet, Gaganpreet and Gurpreet, thank you for your unwavering support and encouragement. Your friendship has been a great source of comfort and motivation.

Lastly, I extend my sincere appreciation to the Thapar Institute of Engineering and Technology (TIET) for providing the resources and facilities necessary for my research. The support and opportunities offered by the institute have been crucial in the successful completion of this thesis.

Thank you all for being an integral part of this journey.

Lovleen Kaur

Table of Contents

Abbreviations i-iii

Symbols iii-iv

Abstracts v-ix

Chapter 1

Introduction and Literature Review

1.1 Transition Metal Complexes and Applications 1

1.2 Iron Complexes in Catalysis 2

1.3 Types of Iron Complexes 3-5

1.3.1 Nature of the ring 3-4

a) Heme Iron complexes 3

b) Non-heme Iron complexes 3-4

1.3.2 Nature of the Iron-Oxygen Bond 4-5

a) Oxo complexes 4

b) Peroxo complexes 4

c) Superoxo complexes 4-5

1.4 Fe(IV)O Complexes in Biology 5-7

1.5 Fe(IV)O Complexes in Biomimetics 7-15

1.5.1 Electron and proton transfer mechanism during C-H activation 8

1.5.2 The Electronic Rearrangement 8-9

1.5.3 Two State Reactivity 10-11

a) Single State Reactivity (SSR) 10

b) Two State Reactivity (TSR) 10

c) Multi-State Reactivity (MSR) 11

1.5.4 The Role of Ligand Architecture 11-15

1.6 Research Gap 16

1.7 Objectives 16

References 17-20

Chapter 2

Methodology

2.1 Computational Chemistry 21

2.2 Theoretical Details 22-29

2.2.1 Approximations 22-24

1. The Born-Oppenheimer Approximation 22

2. The Hartree-Fock (HF) Approximation 22-23

3. Post HF methods 23

a) Moller Plesset Perturbation Theory (MPn) 23

b) Configuration Interaction (CI) 23

4. DFT 23-24

2.2.2 Functionals 25-26

1. Local Density Approximation 25

2. Generalised Gradient Approximation 25

3. Hybrid functionals 25-26

2.2.3 Basis Set 26-27

1. STO 26

2. GTO 26

3. Split Valence Basis Set 27

2.2.4 Additional Functions 27

1. Polarisation Functions 27

2. Diffuse Functions 27

2.2.5 Solvation models 27-28

2.2.6 Quantum Tunneling 28-29

2.3 Tools 29-30

References 30-32

Chapter 3

Role of "S" Substitution on C−H Activation Reactivity of Iron (IV)−Oxo Cyclam Complexes: A Computational Investigation

3.1 Introduction 33-35

3.2 Computational Details 35-36

3.3 Results and Discussions 36-48

3.3.1 Conformational Stability 36

3.3.2 Spin State Reactivity and Electron Transfer Pathways 37-38

3.3.3 SNO Analysis 38

3.3.4 Two State Reactivity and Reactivity Trend 39-43

3.3.5 Reactions of TMC and S-substituted TMC with DHA 43-44

3.3.6 Reactivity Analysis 44

3.3.7 Discussion about the Oxidants 44-45

3.3.8 Distortion Energy 45-46

3.3.9 Spin Density 46

3.3.10 The Energy of Electron Acceptor Orbital 47-48

3.3.11 Triplet-quintet Energy Difference 48

3.4 Conclusions 48-49

References 49-52

Chapter 4

A Density Functional Theory Analysis of the C-H Activation Reactivity of Iron(IV)-Oxo Complexes with 'O' Substituted Tetramethyl-cyclam Macrocycle

4.1 Introduction 53-56

4.2 Computational Details 56-57

4.3 Results 58-65

4.3.1 Spin State Reactivity 59

4.3.2 Reactivity Pattern 60-62

4.3.3 LUMO Energies 62

4.3.4 Spin Density 63

4.3.5 Distortion Energies 63-64

4.3.6 Quantum Chemical Tunneling 64-65

4.4 Conclusions 65-66

References 66-69

Chapter 5

Computational studies on the impact of commutes in ligand structure on C-H activation in non-heme and heme Iron(IV)-oxo complexes

Section A: Impact of Ring Size Modifications on the C-H Activation Reactivity of Non-heme Iron(IV)−Oxo Complexes: A Computational Study with TMC Macrocycles

5.1 Introduction 70-73

5.2 Computational Details 73-74

5.3 Results and Discussions 74-84

5.3.1 Spin State Reactivity 75

5.3.2 Spin State Energy Difference 75-76

5.3.3 Transition State (TS) Parameters 77

5.3.4 Reactivity Pattern 77-79

5.3.5 Reactivity of the Complexes Without Axial Ligands 80

5.3.6. Comparison with Experiment 81

5.3.7 Insights into the Reactivity 82-84

a) Steric Hindrance 82

b) Distortion Energy 82-83

c) The Energy of the Electron Acceptor Orbital 83-84

d) Quantum Mechanical Tunneling 84

5.4 Conclusions 84-85

References 85-87

Section B: Insights into C-H Activation Reactivity of Fe (IV)O Porphyrinoid Complexes: A Computational Investigation

5.5 Introduction 88-89

5.6 Computational Details 90

5.7 Results and Discussions 91-96

5.7.1 Structural Parameters 91

5.7.2 Spin States 91-92

5.7.3 Reactivity Pattern 93

5.3.4 TS Parameters and Distortion Energy 94

5.3.5 Nature of the Acceptor Orbitals 94-95

5.3.6 Core Size of the Macrocycle 96

5.7.7 KIE 96

5.8 Conclusions 96-97

References 97-98

Chapter 6

Conclusions and Outlooks

6.1 Conclusions 99

6.2 Outlooks 99-100

Lists of Conferences and Workshops 101

List of Abbreviations

DFT	Density Functional Theory
V_2O_5	Vanadium oxide
$Ag(NH_3)_2^+$	Diamminesilver cation
$Ag(CN)_2^-$	Dicyanoargentate anion
TMC	Tetramethyl Cyclam
TM	Transition Metal
TauD	Taurine/α-ketoglutarate dioxygenase
N4Py	N,N-bis(2-pyridylmethyl)-N-(pyridin-2-ylmethyl)amine
O_2	Dioxygen
ATP	Adenosine Triphosphate
DNA	Deoxyribonucleic Acid
His	Histidine
Succ	Succinate
Glu	Glutamate
H_2O	Water
CO_2	Carbon Dioxide
CYP450	Cytochrome P450
PheH	Phenylalanine Hydroxylase
Cpd I	Compound I
Cpd II	Compound II
TMC	1,4,8,11-tetramethyl-1,4,8,11-tetraazacyclotetradecane
BnTPEN	N-benzyl-N,N',N'-tris(2-pyridylmethyl)ethylenediamine
dpaq	2-[bis(pyridin-2-ylmethyl)]amino-N-quinolin-8-yl-acetamide
TMP	5,10,15,20-tetramesitylporphyrin
Pc	Phthalocyanine
Pz	Porphyrazine
HAT	Hydrogen Atom Transfer
PCET	Proton-Coupled Electron Transfer
EER	Exchange Enhanced Reactivity
SSR	Single State Reactivity
TSR	Two State Reactivity
MSR	Multistate Reactivity
R	Reactant
TS	Transition State
IH	Intermediate
N_3	Azide
CF_3COO^-	Trifluoroacetate

CH_3CN	Acetonitrile
NO_3^-	Nitrate
TFA	Trifluoroacetic Acid
Ac	Acetate
Bz	Benzoate
Hc	Hydrocinnamate
mV	Millivolt
KIE	Kinetic Isotope Effect
HF	Hartree Fock
MPn	Moller Plesset Perturbation Theory where n = order
CI	Configuration Interaction (CI)
G.S.	Ground State
LDA	Local Density Approximation
GGA	Generalised Gradient Approximation
B	Becke
LYP	Lee-Yang-Parr
B3LYP	Becke, 3-parameter, Lee-Yang-Parr
STO	Slater-type orbitals
GTO	Gaussian-type orbitals
CGF	Contracted Gaussian Functions
SCRF	Self-Consistent Reaction Field
CPCM	Conductor-like Polarizable Continuum Model
SMD	Solvation Model based on Density
THC	Tetrahydro Cyclam
ZPVE	Zero-point vibrational energy
IRC	Intrinsic Reaction Coordinate
NCI	Non-covalent Interactions
CDO	Cysteine dioxygenase
OvoA	Ergothioneine biosynthesis enzymes
ax	Axial
DHA	Dihydroanthracene
LANL2DZ	Los Alamos National Laboratory 2 Double Zeta
ECP	Effective Core Potential
SDD	Stuttgart Dresden
$CF_3SO_3^-$	Triflate
kcal/mol	Kilocalories per mole
eV	Electron Volt
ET	Electron Transfer

PT	Proton Transfer
CH_3	Methyl Group
PES	Potential Energy Surface
LUMO	Lowest Unoccupied Molecular Orbital
QMT	Quantum Mechanical Tunneling
NCMe	Acetonitrile
OAT	Oxygen Atom Transfer
w.r.t	With respect to
CCDC	Cambridge Crystallographic Data Centre
TIET	Thapar Institute of Engineering and Technology
av	Average
KIE	Kinetic Isotope Effect
Por	Porphyrin

List of Symbols

H^+	Proton (Hydrogen ion)
e^-	Electron
.+	Radical cation
σ	Sigma
π	Pi
α	Alpha spin
β	Beta spin
ΔE_{T-Q}	Spin State Gap
2°	Secondary
Å	Angstrom
$\hat{H}$	Hamiltonian operator
Ψ	Wavefunction
$\hat{F}$	Fock operator
ϕ	Molecular orbital
ε	Energy

ρ	Electron Density
ζ	Effective nuclear charge
r	Radius
*	Polarisation function
+	Diffuse Function
k	Rate Constant
κ	Transmission Constant
δ	Sigma
ΔG	Gibbs free energy change
K	Kelvin
°	Degrees
i	Imaginary Frequency
a.u.	Atomic unit
$\%V_{bur}$	Buried Volumes
$\Delta E^{\ddagger}_{dis}$	Distortion Energy
a_{1u}/ a_{2u}	Radical State

Abstracts

Chapter 1

This chapter offers a concise overview of the broad applications of transition metal complexes, with a focus on reaction catalysis by iron (Fe) complexes. In particular, the chapter delves into oxidation reactions mediated by Fe(IV)O species, both heme and non-heme, emphasizing the rapidly growing field of C-H activation. The literature relevant to this process has been systematically reviewed, depicting how biological enzymes inspired biomimetic complexes to carry out these reactions. Various concepts, such as Two State Reactivity, and mechanisms of the proposed transfers have been deliberated. A detailed discussion on the influence of factors such as ligand architecture, on these activation processes is provided. Ligand architecture, including modifications to both the axial and equatorial coordination environments, plays a pivotal role in governing the reactivity of these complexes. Studies have shown that alterations to these ligands, such as heteroatom substitutions, can significantly impact reaction dynamics, influencing parameters like redox potentials and activation barriers. Furthermore, an assessment of gaps in the current literature is presented, with particular emphasis on recent advancements in the field. These insights are crucial for guiding the rational design of next-generation catalysts with improved performance and selectivity. The chapter concludes by outlining the objectives of the current research, aiming to address these identified gaps.

Chapter 2

This chapter provides an in-depth introduction to the essential principles and methodologies of computational chemistry. It begins by explaining quantum mechanics (QM) as the theoretical basis for many computational methods, particularly highlighting the Schrodinger equation as the core equation governing quantum systems. While the exact solution of this equation is only feasible for single-electron systems, approximations are necessary for multi-electron systems. The Born-Oppenheimer approximation is then discussed followed by Hartree-Fock (HF) theory, which is introduced as an ab initio method for solving the Schrodinger equation, though its limitations in accounting for electron-electron corelations are addressed. Post-HF methods, developed to include electron correlation, are described as important advancements to improve accuracy, despite their higher computational cost. The chapter further elaborates on Density Functional Theory (DFT), which is based on the electron density rather than wave functions, making it a widely used approach due to its balance between computational efficiency and

accuracy. The chapter explores the use of functionals like B3LYP, which has been proven to show results with great accuracy in this field. Other factors such as basis sets and solvent models employed have been discussed. Additionally, the chapter discusses the advanced computational tools used in modern chemistry, such as Gaussian 16 for geometry optimization, frequency analysis, and thermochemistry. Visualization tools like Chemcraft is highlighted for their ability to provide molecular structures, bond lengths, atomic charges, and spin densities. Other tools, such as KiSThelP software, are described as valuable for studying tunneling effects and kinetic analysis. Overall, the chapter not only outlines the theoretical frameworks but also demonstrates the practical tools and techniques of computational chemistry, setting the stage for the more detailed studies presented in later sections.

Chapter 3

A comprehensive DFT investigation has been presented in this chapter to address the role of equatorial sulfur ligation in C-H activation. A nonheme iron-oxo compound with four nitrogen atoms constituting the equatorially connected macrocyclic framework (represented as N_4) $[Fe(IV)O(THC)(CH_3CN)]^{2+}$(THC = 1,4,8,11-tetrahydro1,4,8,11-tetraazacyclotetradecane), has been considered as the base compound. Other complexes have been anticipated by the sequential replacement of this nitrogen by sulfur i.e., N_4, N_3S_1, N_2S_2, N_1S_3, and S_4. Generally, the anti-conformers (with respect to equatorial N-H and Fe=O) turned out to be the most stable. It was found that with the enrichment of the equatorial sulfur atom, reactivity increases successively, i.e., we get the trend $N_4 < N_3S_1 < N_2S_2 < N_1S_3 < S_4$. Our investigations have also verified the available experimental results, where it has been reported that N_2S_2 is more reactive than N_4 in their mixed conformation. In search of insight into this typical pattern of reactivity, the interplay of several factors has been recognised, such as the distortion energy - distortion energy decreases for the transition states with the addition of sulfur; the spin density - the spin density on the oxygen atom increases, implying that the radical character of the abstractor increases on sulfur ligation; the energy of the electron acceptor orbital - the energy of the LUMO (σ^*z^2) decreases continuously with the sulfur substitution; and the triplet-quintet oxidant energy gap—the energy gap decreases consistently with S-enrichment in the equatorial position. The computational predictions reported here, if further validated by experiments, will definitely encourage the synthesis of sulfur-ligated bioinspired complexes instead of the ones constituting nitrogen exclusively.

Chapter 4

In this chapter, we present a meticulous computational study to foresee the effect of an oxygen-rich macrocycle on the reactivity of C-H activation. For this study, a widely studied nonheme Fe(IV)O molecule with a TMC (1,4,8,11-tetramethyl 1,4,8,11-tetraazacyclotetradecane) macrocycle that is equatorially attached to four nitrogen atoms (designated as N_4) and acetonitrile as an axial ligand has been taken into account. For the goal of hetero-substitution, the step-by-step replacement of the N_4 framework by O atoms, i.e., N_4, N_3O_1, N_2O_2, N_1O_3, and O_4 systems, has been considered, and dihydroanthracene (DHA) has been used as the substrate. In order to neutralise the system and prevent the self-interaction error in DFT, counterions called triflates have also been included in the calculations. Studying the energetics of these C-H bond activation reactions and the potential energy surfaces mapped therefore reveals that the initial hydrogen abstraction, which is the rate-determining step, follows the two-state reactivity (TSR) patterns, which means that the originally excited quintet state falls lower in the transition state and product. The reaction follows the hydrogen atom transfer (HAT) mechanism, as indicated by the spin density studies. The results revealed a fascinating reactivity order, in which the reactivity increases with the enrichment of the oxygen atom in the equatorial position, namely, the order follows $N_4 < N_3O_1 < N_2O_2 < N_1O_3 < O_4$. The impact of oxygen substitution on quantum mechanical tunneling and H/D kinetic isotope effect studies have also been investigated. When analysing the causes of this reactivity pattern, a number of variables have been identified, including the reactant like transition structure, spin density distribution, the distortion energy, and the energies of the electron acceptor orbital, i.e., the energy of LUMO ($\sigma^*_{z^2}$), which validate the obtained outcome. Our results also show very good agreement with earlier combined experimental and theoretical studies considering TMC and TMCO-type complexes. The DFT predictions reported here will undoubtedly encourage experimental research in this biomimetic field, as they provide an alternative with higher reactivity in which heteroatoms can be substituted for traditional nitrogen atoms.

Chapter 5

In the first part of this chapter, a DFT investigation has been presented to demonstrate the relevance of the macrocyclic ligand ring size of the high-valent non heme Fe(IV)O complex-catalyzed C-H activation process. Tetramethylcyclam (TMC) with varying ring size measures in terms of n = 12, 13, 14, 15, and 16 in $[Fe(IV)O(n\text{-}TMC)(CH_3CN)]^{2+}$ has been considered as the oxidant and dihydroanthracene as the general substrate. Computations were also carried out

to determine the effect of the axial ligand-acetonitrile on the C-H activation reactivity. It was discovered that the complexes without axial ligands turned out to be more reactive compared to their axially coordinated counterpart. The most intriguing finding, however, was that reactivity increased steadily with ring size increments, giving us the trend 12<13<14<15<16. Behind this typical pattern of reactivity, several factors played a role, including the energy of electron acceptor orbital which sequentially decreases, distortion energy to achieve the transition state which also decreases as we move on from n=12 to 16. The triplet-quintet energy difference of the oxidants also has a part to play, as it decreases with increased ring size, with the quintet becoming more and more dominant. The current studies were also able to corroborate the experimental data that was published regarding Fe(IV)O(13-TMC) (without axial syn form) having a higher C-H activation reactivity than Fe(IV)O(14-TMC) (with axial anti-form). On the whole, this computational presentation gives us a reactivity pattern relying on the ring size commutes and can lead to successful experimental results if pursued based on this reaction.

The second part consists of the heme complexes, presenting a detailed comparative analysis of C-H activations catalysed by three different Fe(IV)O porphyrinoid complexes. The study considers the usual heme porphyrin (complex I) as the base compound, porphyrazine (complex II), which is obtained by replacing carbon with nitrogen at the meso position, and phthalocyanine (complex III), which is obtained through the peripheral benzoannulation of porphyrazine. The main focus here is to explore the impact of bridging groups and peripheral functionalisation in heme systems on reactivity. Chloride is used as the axial ligand for all complexes, and DHA is used as the substrate. Factors such as distortion energy and different electron acceptor orbitals significantly affect the overall reactivity. The effect of substitution on quantum mechanical tunneling using H/D kinetic isotope effect studies is also included. The results reveal a fascinating reactivity order: mesonitrogen substitution enhances reactivity, while additional benzo-annulation hinders reactivity, leading to the order complex II > complex I > complex III. In comparison to the usual model compound I, which is Fe(IV)O-porphyrin π cation radical with an –SH axial ligand, complex II was found to be more reactive. These findings support the use of accessible iron frameworks derived from porphyrin in C-H activation processes.

Chapter 6

This chapter provides conclusion drawn from the research work presented in previous chapters by using DFT to investigate the reactivity and mechanisms of Fe(IV)Oxo complexes, focusing on ligand architecture modifications. Key findings include that hetero-substitution, such as replacing nitrogen with sulfur in macrocyclic ligands, significantly enhances C-H activation reactivity. Additionally, changes in the coordination sphere, including ring size and axial ligand removal, further optimise catalytic efficiency. Studies on heme complexes reveal that structural changes, such as nitrogen substitution and benzo-annulation, influence reactivity patterns. Theoretical results align well with experimental data, confirming the reliability of the reactivity trends.

The outlook section proposes expanding research to other metal frameworks, such as manganese and metal-oxygen species, and continuing to explore ligand modifications in heme-type complexes for further catalytic optimization.

Chapter 1

Introduction and Literature Review

1.1 Transition Metal Complexes and Applications

Transition metal complexes serve a substantial role in the realm of inorganic chemistry due to their unique ability to bind with a variety of ligands, which they owe to their d orbitals.[1] These transition metal complexes are fundamental to numerous biological systems, materials science applications, and function as catalysts in both industrial and synthetic chemistry.[2] They play vital roles in various fields, including medicinal chemistry (e.g., cisplatin for cancer treatment), industrial catalysis (e.g., V_2O_5 in the contact process), and analytical chemistry (e.g., $Ag(NH_3)_2^+$ in Tollens' reagent) as depicted in Fig. 1.1.[3] The versatility of such complexes is showcased in various oxidation states with diverse geometries as well as electronic configurations among various coordination numbers.

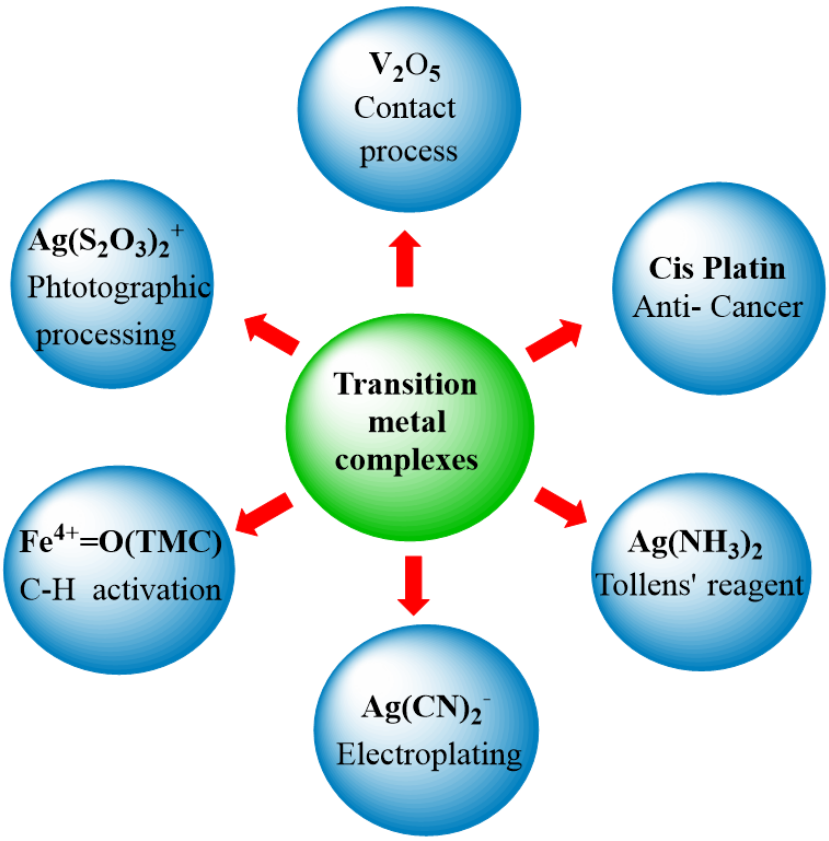

Figure 1.1: Conventional uses of TM complexes.

Within catalysis, they activate reactants and induce diverse reactions by enabling them to occur under milder conditions, saving energy and reducing environmental impact.

1.2 Iron Complexes in Catalysis

Over the last four decades, researchers have studied different TM complexes ranging from groups 3 to 10 encompassing Mn and Fe-based complexes.[4-7] Iron has been found to be an essential component of the active sites of various catalytic processes, among diverse oxidation states (III, IV, and V).[8-10] Advantages such as cost effectiveness and non-toxicity have paved the way for its potential and future opportunities.[11] Also, its bioavailability is another factor leading to extensive exploration not just in biological processes but in the field of biomimetic chemistry as well. Hence, these complexes are an ideal subject for thorough investigation and have served as the foundation for our research. Several key reactions catalysed by these complexes include oxidation, cyclisation, cyclopropanation, and hydrogenolyses.[12-14] One of the prominent categories is oxidation reactions, which include transformations such as oxidative coupling, alkene epoxidation, alcohol oxidation along with aliphatic and aromatic hydroxylation, among others (Scheme 1.1).[15,16] In our thesis we would focus on such hydroxylation reactions in detail, which are the C-H activation processes. It is a pivotal process in modern chemistry, where an otherwise inert C-H bond is selectively cleaved and transformed into a more reactive or functionalised entity.[17] This transformation is often mediated by transition metal catalysts.

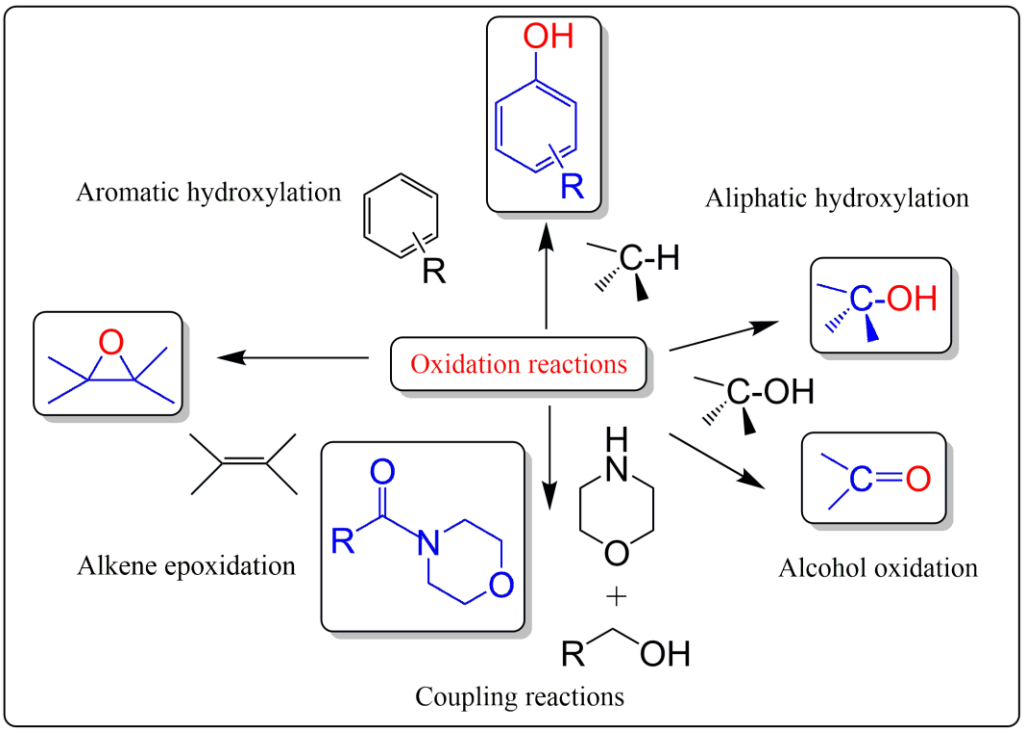

Scheme 1.1: Various types of oxidation reactions catalysed by Fe complexes.

1.3 Types of Iron Complexes

Based on their structural parameters, iron complexes can be classified into distinct classes. According to the nature of the ligand ring structure, they can be classified as heme and non-heme complexes.[18,19]

1.3.1 Nature of the ring

In this classification the characteristics of the rings involved in the Fe complexes vary and can be heme or non-heme.

a) **Heme Iron complexes**: Heme iron complexes serve as the prosthetic group or active sites of several critical enzymes, such as cytochromes, catalases, and peroxidases.[20-23] Structurally, they consist of a central iron coordinated to a porphyrin ring, which is a large, heterocyclic macrocycle composed of four pyrrole subunits linked by methine bridges, such as in cytochrome P450 enzymes (Fig. 1.2 (a)).[23-26] A range of bioinspired systems have been developed that closely resemble the heme structure. While the unmodified ring is referred to as porphyrin,[27] extensive research has led to the exploration of various structural modifications, culminating in a diverse array of analogues, such as phthalocyanine,[28] as represented in the subsequent Fig. 1.2(b).

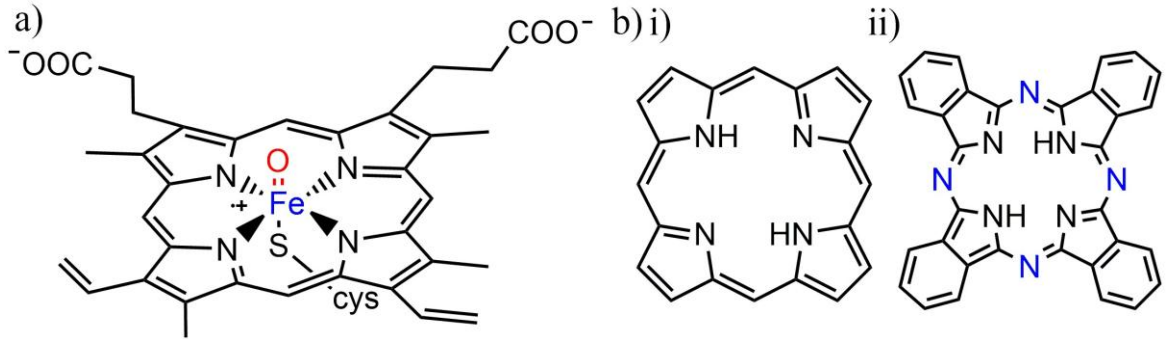

Figure 1.2: a) Active site in cytochrome P450, b) Heme frameworks i) Porphyrin and ii) Phthalocyanine.

b) **Non-heme Iron complexes**: In contrast, these complexes serve as the active sites in various non-heme enzymes (e.g., TauD, taurine/α-ketoglutarate dioxygenase). Unlike porphyrin rings, they do not coordinate directly with porphyrin structures but instead interact with non-porphyrin ligands such as amino acid residues, water, or other heteroatoms within their frameworks,[29] as illustrated in Fig. 1.3. Despite the absence of the porphyrin ring, non-heme complexes are equally important and provide a wider range of reactions.[30-33]

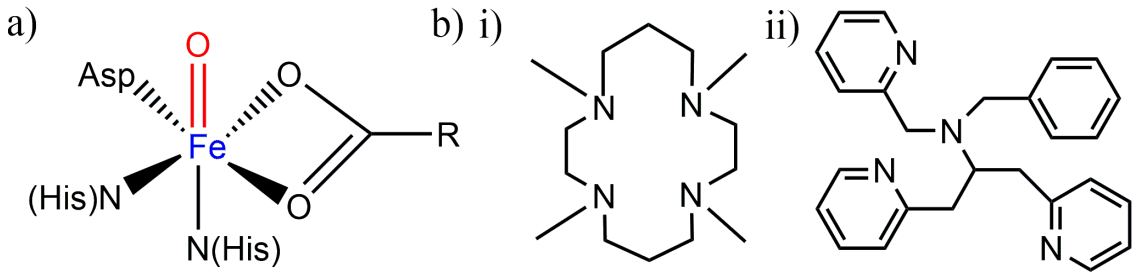

Figure 1.3: a) Active site of TauD and b) Non heme frameworks i) TMC and ii) N4Py.

Further, if O is bonded to the Fe atom, such complexes can vary based on the characteristics of the metal oxygen bond into oxo, superoxo, and peroxo complexes.[34,35]

1.3.2 Nature of the Iron-Oxygen Bond

An essential aspect in oxidation catalysis of the iron complexes is their ability to form Fe oxo, peroxo, and superoxo species. The difference lies in the Fe-Oxygen bond described as below:

a) Oxo complexes: In these complexes, the Fe centre has a double bond linking it to an O atom, as illustrated in Fig. 1.4(a).[36-42]

b) Peroxo complexes: These complexes feature the Fe linked to an O_2 in a bridging arrangement, leading to a peroxo ligand that remains intact as shown in Fig. 1.4(b).[43,44]

c) Superoxo complexes: The complexes also involve a Fe ion coordinated to an O_2 entity, but in an end-on fashion, with the O_2 unit acting as a superoxo ligand as shown in Fig. 1.4(c).[45]

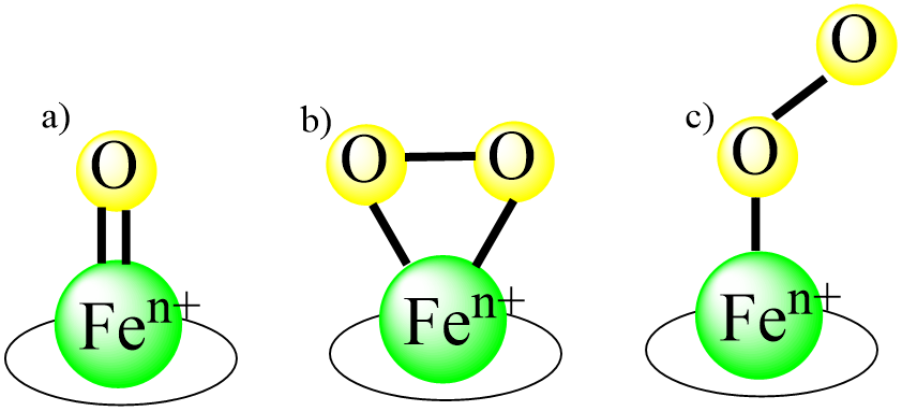

Figure 1.4: Types of metal complexes a) Oxo b) Peroxo and c) Superoxo

It has been studied how steric hinderance in different ring sizes possible along Fe and other metal complexes have a part to play regarding the formation peroxo/superoxo complexes. Thermodynamics is another important governing factor.[46] In general, nucleophilic reactions are studied for metal-peroxo species while electrophilic are more popular in superoxo. In our

studies we have focussed on Oxo complexes, which are recognized as crucial intermediates in C-H activation processes.

1.4 Fe(IV)O Complexes in Biology

Biologically, iron enzymes, catalyse multiple metabolic processes in living species, including oxygen transport, ATP production, DNA synthesis, and electron transport.[47] A few such enzymes, along with the active structures and key reactions, are presented here in Table 1.1

Table 1.1: A compilation of fundamental Fe(IV)O complexes found in natural enzymes.

Iron Enzymes	Catalytic Reactions	References
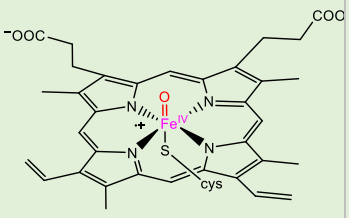 Cytochrome P450	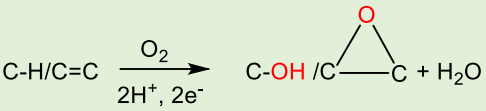	48
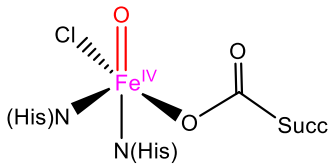 Halogenase CytC3	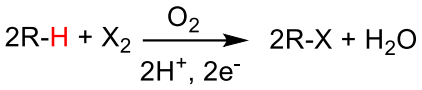	49
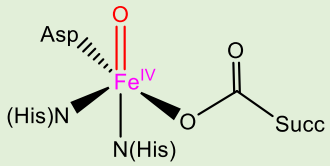 α-ketoglutarate dependent dioxygenases	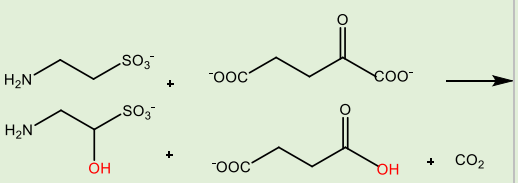	50
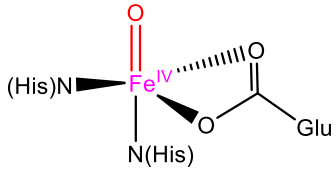 Phenylalanine Hydroxylase	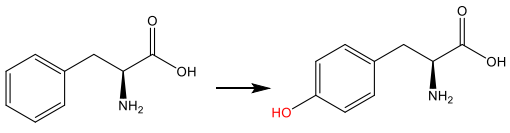	51

One point of commonality among these is the Fe(IV)Oxo counterpart in their active sites. The very first mononuclear Fe(IV)Oxo based enzymatic intermediate was characterised in 2003,

which is alpha-ketoglutarate-dependent taurine dioxygenase. This enzyme catalyses the hydroxylation of taurine.[50] The proposed mechanism is presented here in Scheme 1.2.

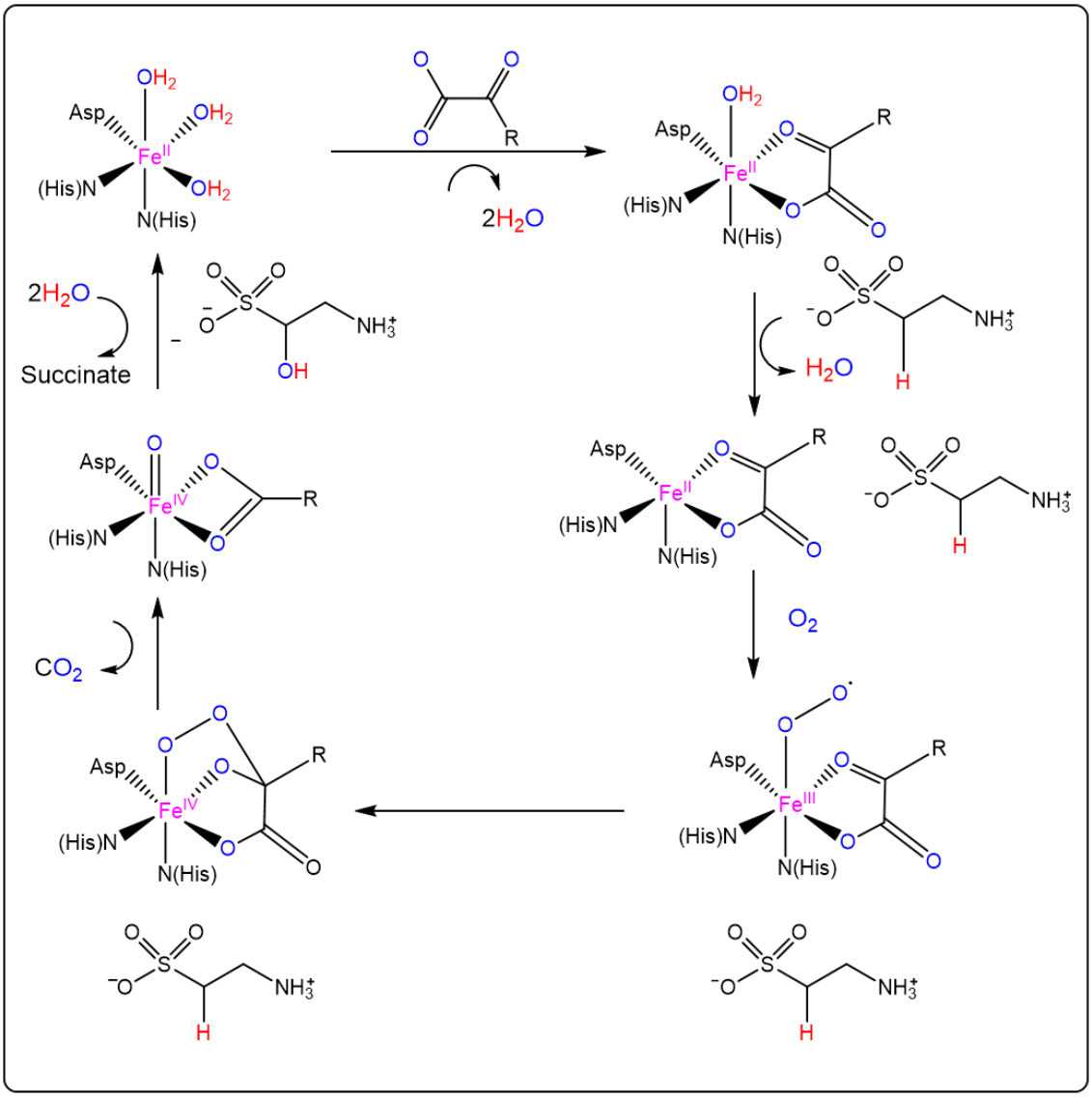

Scheme 1.2: Mechanism followed by alpha-ketoglurate dependent taurine-dioxygenase.

Initially, two H_2O molecules are displaced followed by the binding of the substrate expels another H_2O molecule, forming a 5-coordinated Fe centre that ultimately facilitates the activation of O_2. Fe(III)superoxo intermediate then attacks the electrophilic C atom of alpha-ketoglutarate ligand giving us the intermediate, Fe alkyl-peroxo. Subsequent bond cleavage steps ultimately lead to the exclusion of CO_2 and succinate, generating the active species responsible for the activation. Since then, such intermediates of several enzymes have been vastly explored.[52-55] Understanding the important roles of these enzymes in biological systems is crucial, as it helps elucidate the fundamental mechanisms driving these phenomena.

Among heme complexes, such a mechanism is shown by CYP450 (Compound I).[48] A schematic representation (Scheme 1.3) has been shown herein.

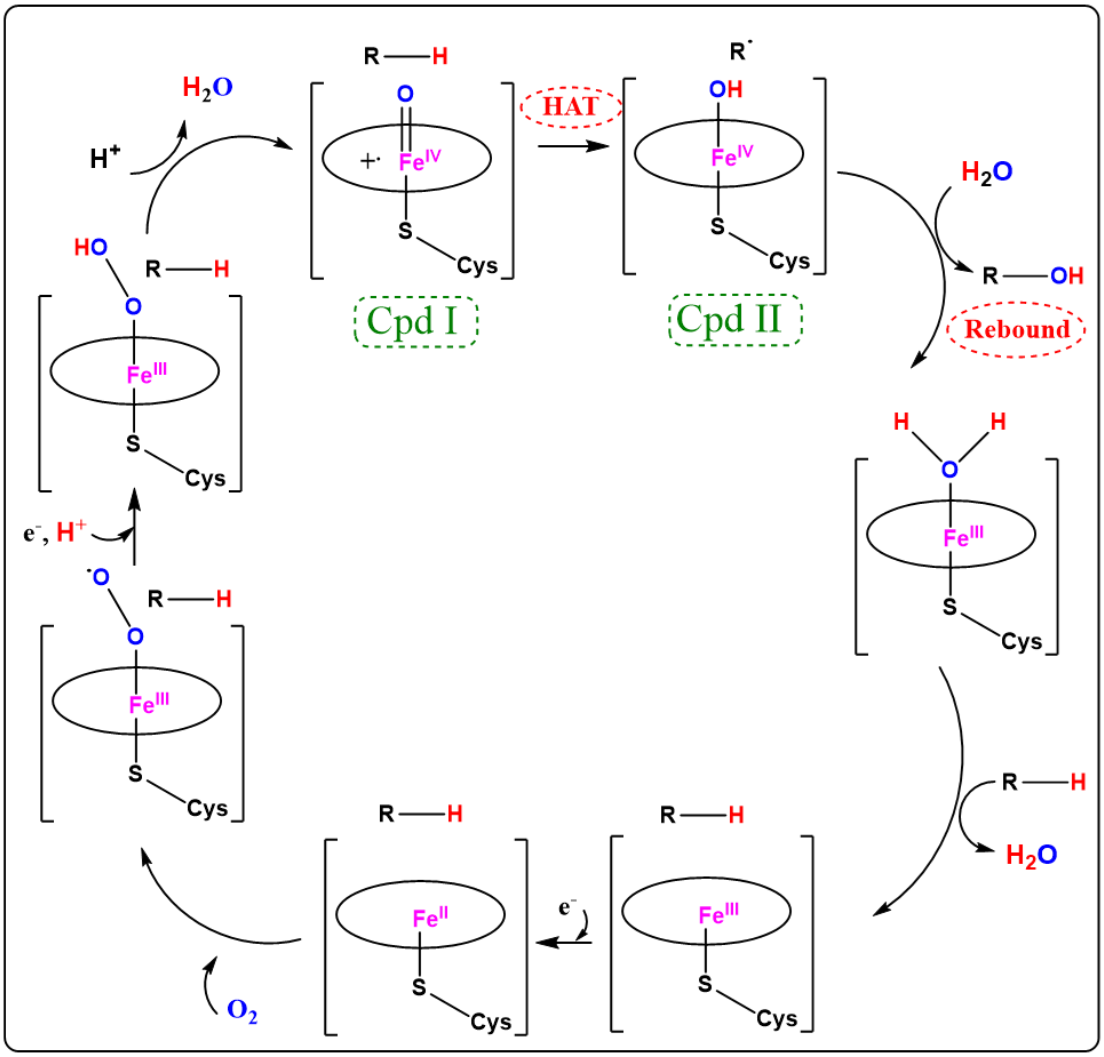

Scheme 1.3: Cytochrome P450 in C-H activation.

Cpd I refers to Fe(IV)O porphyrin π-radical cations, whereas the 1 e^- reduced version are marked as Cpd II.

These enzymes, along with enormous others, have long developed the interest of biochemists, inorganic chemists, and researchers due to their potency and versatility.[56-62]. Motivated by these findings, Fe(IV)Oxo species have been synthesized in laboratories worldwide to replicate their active cores. [42]

1.5 Fe(IV)O Complexes in Biomimetics

A plethora of researchers specialising in biological, bioinorganic, and oxidation chemistry have synthesised catalysts consisting of the ferryl unit. The primary biomimetic model system to be

characterised in this category was the tetraazamacrocyclic ligand TMC, as depicted by Rohde et al.[63] Ever since, over 90 synthetic non-heme complexes in this category have been documented in attempts to mimic enzymatic intermediates in terms of spectroscopy, function, or structure.[64,65] Some of them are exemplified here in Fig. 1.5.

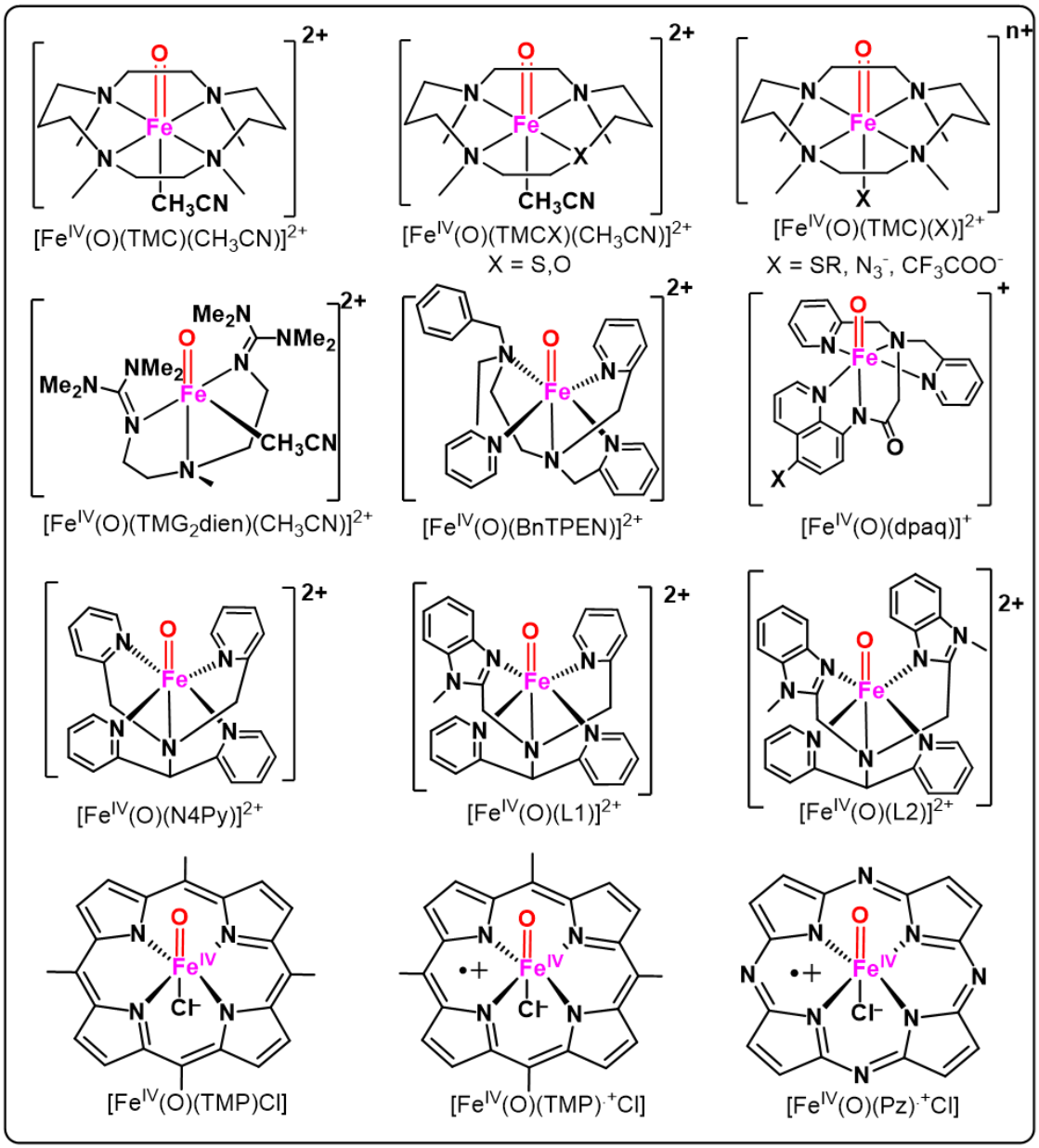

Figure 1.5: A few Fe(IV)O complexes.

A significant number of these macrocycles possess a shared ligand structure, which is mostly derived from either the TMC or other rings such as N4Py along with BnTPEN.[66-70] Hence, the following section will highlight some of the important aspects.

1.5.1 Electron and proton transfer mechanism during C-H activation

The transfer of both a proton (H^+) and an electron (e^-) takes place in a couple of ways, broadly bifurcated into HAT and PCET types of mechanisms.[71] HAT reactions have been characterized as the concurrent transfer of both an electron and a proton especially involving the same donor as well as the acceptor atoms[72] as shown in Scheme 1.4.

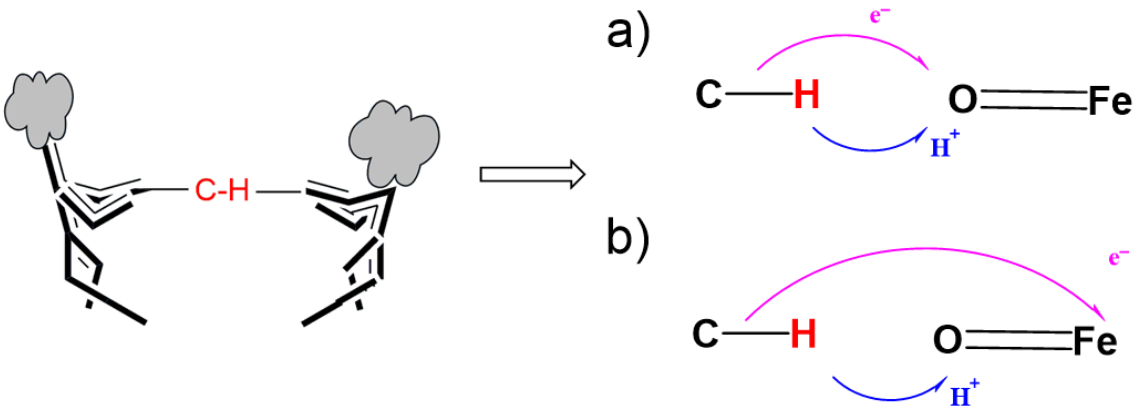

Scheme 1.4: a) HAT, and b) PCET mechanism

Hence, it is also referred to as true hydrogen transfer, and there is no significant molecular charge redistribution. Another category, PCET, involves different donor and acceptor atoms for the proton and electron.[73] Here, the transfer still takes place in a concerted step, but to different sites, and hence charge redistribution is involved.[74] Studies of frontier molecular orbitals direct towards the type of transfer that has taken place in such reactions. Some governing factors include steric reasons. i.e., in C-H activation processes without steric hinderance, HAT has been reported.[75] However, when direct Fe=O access was prevented, PCET reactions were observed instead.

1.5.2 The Electronic Rearrangement

It is well-established that the unique reactivity Fe(IV)O oxidants can be explained by their spin state, whether low or high spin. [76,77] The electron arrangement for S=1 (Triplet State) is $(\sigma_z)^2$ $(\pi_{x,y})^4$ $(\delta_{xy})^2$ $(\pi^*_{xz,yz})^2$ $(\sigma^*_{x^2-y^2})^0$ $(\sigma^*_{z^2})^0$ and $(\sigma_z)^2$ $(\pi_{x,y})^4$ $(\delta_{xy})^1$ $(\pi^*_{xz,yz})^2$ $(\sigma^*_{x^2-y^2})^1$ $(\sigma^*_{z^2})^0$ for S=2 (Quintet State) as shown in the Figure 1.6. below. So, the quintet state emerges when an electron from the $(\delta_{xy})^2$ is facilitating to the $(\sigma^*_{x^2-y^2})^0$ orbital due to the EER[78]. To investigate C-H activation processes, the incoming substrate can transfer electrons to these orbitals through two common pathways, depending on the spin states previously discussed.[79] Fig. 1.6(a) illustrates the low-spin pathway (S = 1), where a β electron from the σ_{C-H} bond is transferred to one of the π* orbitals of the central metal, referred to as the π trajectory.

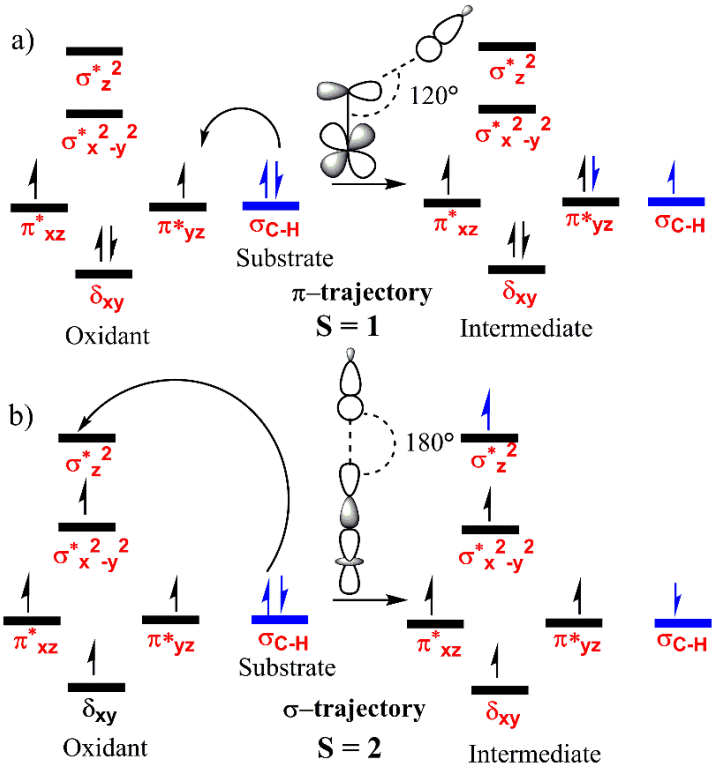

Figure 1.6: General electron rearrangement diagram for hydrogen abstraction catalysed by the Fe(IV)O complexes for the spin states a) S = 1 and b) S = 2.

In this case, the substrate aligns with a Fe−O−H angle of approximately 120°. Fig. 1.6(b) depicts the high-spin pathway, where an α electron from the σ_{C-H} bond moves to the σ_z^{2*} anti-bonding orbital of Fe−O. For this pathway, the substrate must approach the oxidant from the upper side, with a Fe−O−H angle of about 180° termed as the σ trajectory.

1.5.3 Two State Reactivity

Different types of reactivity depending on spin states involved are possible,[80] as addressed below:

a) Single State Reactivity (SSR): This category involves the reaction proceeding solely via one specific spin state, it is termed as SSR process. The other spin state, if involved, shows a significantly different energy level compared to the ground state. The arrangement through the reaction has been represented in Fig. 1.7(a) below.

b) Two State Reactivity (TSR): This occurs when the reaction can proceed through two different spin states. This might involve two closely lying spin states as shown in Fig. 1.7(b) or another possibility involves a transition across the different states in the reaction surface[76] as depicted in Fig. 1.7(c).

c) Multi-State Reactivity (MSR): In more complex scenarios, the reaction may involve more than two spin states, with the possibility of interconversions among several electronic configurations throughout the reaction pathway as depicted in Fig. 1.7(d).

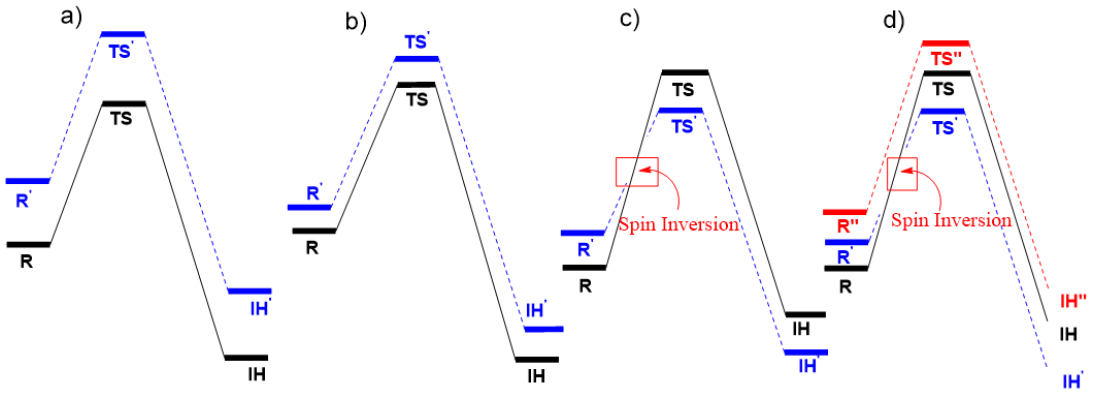

Figure 1.7: a) SSR, b) and c) TSR, d) MSR respectively where R is the reactant, TS the transition state and IH the intermediate along the reaction dynamics.

1.5.4 The Role of Ligand Architecture

Now that we have a grasp of the mechanistic details, we must focus on pathways for better reactivities which involves subjecting the complexes to various degrees of freedom, such as stereochemistry and ligand architecture.[80-84] This section provides a detailed discussion on how the architecture of ligands significantly influences the C-H activation. The precise control of the reactions relies on a deep understanding of their coordinated ligand architecture. Careful design of a complex ligand framework is essential to balance factors like thermodynamic stability and structural adaptability, along with the chemical reactivity. The starting point is the primary coordination sphere, which comprises the ligand donor atoms.[85-93] This encompasses both axial and equatorial frameworks, where the axial framework refers to the ligands positioned along the axis of the central metal atom, while the equatorial framework includes those arranged in the plane perpendicular to the axis. Our overview presented here provides detailed insights into how the synthesis, characterisation, and reaction kinetics of Fe(IV) Oxo complexes, mediated by these ligand donor atoms, have been explored in this field to date.

Sastri et al. established that the behaviour of $[Fe(IV)O(TMC)(X)]^{n+}$ can be tuned by varying the axial ligands, structures depicted in Fig. 1.8. Reactivity for C-H activation turned out to be in the order SR > N_3 > $OOCCF_3$ > $NCCH_3$, as evident from the subsequent lower reduction potential values.[94] The reactivity order can be explained by the dip of the ΔE_{T-Q} energy gap due to the electron-donating nature of the axial ligand, which elevates the overall reactivity.

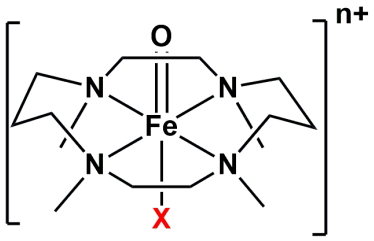

Figure 1.8: [Fe(IV)O(TMC) (X)] where X = SR, N_3^-, CF_3COO^- and CH_3CN.

Among heme complexes, an example studied by Takahashi et al. includes Fe(IV)Oxo complex as explored in CpdI which is $[Fe(IV)O(TMP)^{\bullet+}(X)]$. Axial ligands were selected from the range of anionic ligands represented by X as shown in Fig. 1.9.

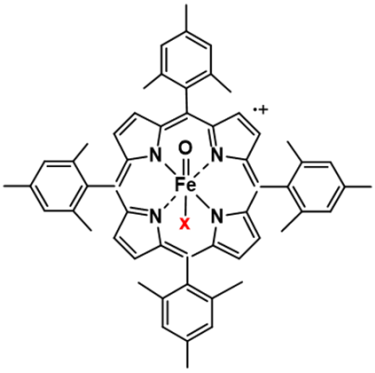

Figure 1.9: $[Fe(IV)O(TMP)^{\cdot+}(X)]$ where X = NO_3, Cl, F, TFA, Ac, Bz, Hc where all are mono-anionic.

Trend X = NO_3 < TFA < Ac < Cl < Hc < Bz < F was observed. It was reported that the stronger the ligation of these ligands, the [Fe(III)TMP(X)] became more stable, leading to higher reactivity in the corresponding $[Fe(IV)O(TMP)^{+\cdot}(X)]$ complex.[95]

Now shifting focus to the equatorial framework, while N_4 tetradentate donor complexes have been extensively studied, recent research has started to explore heterosubstitution with other atoms, such as S and O. In an experimental study on the N_4 and N_2S_2, complex by Deutscher et al., they synthesised and characterised the complexes[96] depicted in Fig. 1.10.

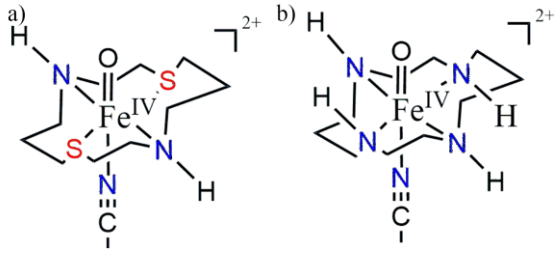

Figure 1.10: a) N_4 and b) N_2S_2 framework.

Interesting trends were minor elongation (0.2 Å) of the ferryl bond and a positive increase in the $Fe^{2+/3+}$ redox potential on switching from N_4 to N_2S_2 leading to better C-H activation barriers with cis sulfur ligation. The experimental barrier difference between the two was 5 kcal mol^{-1}. KIE studies were also carried out using xanthene substrate, which depicted that value being $N_4 = 20$ and $N_2S_2 = 1.47$, signifying that the former has an HAT mechanism whereas later followed the PCET mechanism.

For further demonstration of the relevance of equatorially bound sulfur ligands in nonheme metalloenzymes Satpathy et al. synthesised and characterised a N_5 Fe(IV)O macrocycle and compared the results with the corresponding N_4S_1 ligated Fe(IV)O complex[97] as depicted in Fig. 1.11.

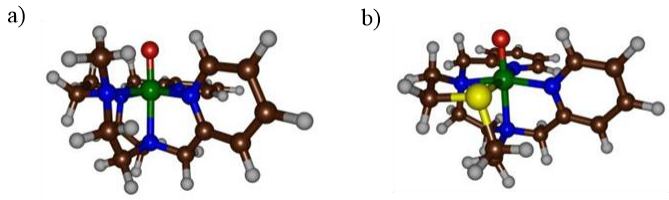

Figure 1.11: DFT structures of a) N_5 and b) N_4S_1 framework. (Adapted from Reference 97)

The reaction mechanism of C−H activation using CHD as the substrate was studied. The studies revealed that both complexes have a S=1 spin ground state (> 5 kcal mol^{-1}) with $\delta_{xy}^2\ \pi^*_{xz}{}^1\ \pi^*_{yz}{}^1$ orbital occupation for L.S. A rate enhancement of a factor of two was reported, however, an experimental value of 3.5 was observed. The study highlighted that the equatorial sulfur ligand in N_4S_1 influences the reduction potentials of the Fe(IV) complexes, enabling quicker second electron transfer alongside 1st HAT and hence hydride transfer. This is followed by the proton transfer mechanism. However, in N_5, two consecutive hydrogen atom abstraction reactions take place. This had a diminishing effect on the tunneling contribution, resulting in a reduced KIE value.

Further on, moving on to oxygen substitution, Ray and co-workers substituted one of the NMe donors in TMC with an O donor atom $[FeIV(O)(TMCO)(OTf)]^+$ as shown in Fig. 1.12.[98]

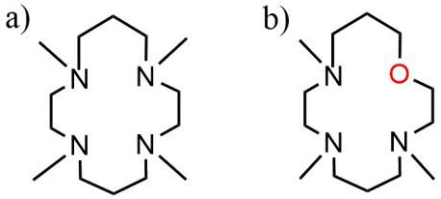

Figure 1.12: TMC with i) N_4 and ii) N_3O framework

This substitution resulted in 5-6x better reactivity and HAT transfer. The main reason behind this pattern of increased reactivity by the incorporation of O was attributed to the better electrophilicity of the metal centre and also to the fact that the more reactive state became readily available. This was due to the shifts in the d_{xy} and $d_{x^2-y^2}$ orbital energy gap.

In conclusion, extensive investigations into the C-H activation kinetics of ligand donor atoms have been conducted, as referenced in studies, covering both heme and non-heme complexes. Moving on to the 2° coordination sphere, factors such as variations in the extended ligand framework are known to have an impact on the electronic and steric parameters, and these aspects have also garnered significant attention. We are therefore taking into consideration both theoretical and experimental work conducted in this regard in the recent decade. We investigate patterns of reactivity as well as the myriads of factors that contribute to patterns of reactivity.

In a study by Mitra et al., 1 (L1) and then 2 pyridyl units (L2) of N4Py were swapped by (N-methyl)benzimidazolyl, as depicted in Fig. 1.13.[99]

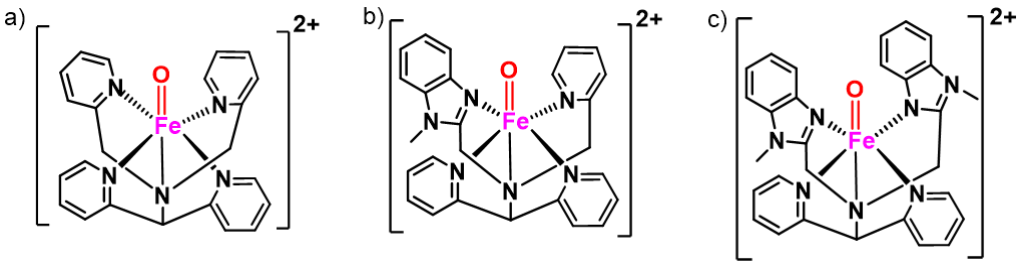

Figure 1.13: a) $[FeIV(O)(N4Py)]^{2+}$, b) $[FeIV(O)(L1)]^{2+}$, and c) $[FeIV(O)(L2)]^{2+}$.

This substitution led to the weakness in the ligand field evident from redox potential and spectral data. HAT (proceeding via high spin transition state) thereby showed an increase of 1 degree per replacement.

Another type of modification was altering the ring size of the TMC ligand studied by Hong et al.[100] 13 and 14 TMC were compared, as depicted in Fig. 1.14.

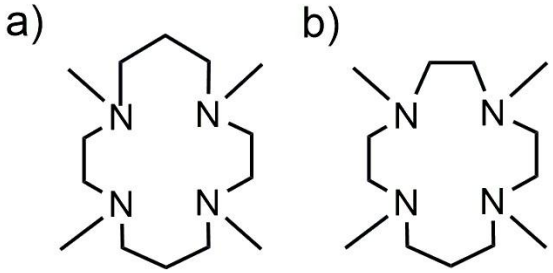

Figure 1.14: TMC with a) n = 13 and b) n = 14 framework.

The former showed a higher reduction potential ($Fe^{IV/III}$) and being 3 x 10^3 more reactive than the latter.

All of these studies along with their nature have been summarised in the Table 1.2.

Table 1.2: Different types of ligand architecture studied in TMC complexes.

Oxidants	Nature of the ring	Ligation	Nature of studies	References
$[Fe(IV)O(TMC)(X)]^{n+}$ X = SR, N_3^-, CF_3COO^-, CH_3CN	Non-heme	Primary Axial	Experimental + Computational	94
$[Fe(IV)O(TMP)^{+\cdot}(X)]$ X = NO_3, Cl, F, TFA, Ac, Bz, Hc	Heme	Primary Axial	Experimental + Computational	95
$[Fe(IV)O(THC)(CH_3CN)]^{2+}$ THC = N_4 and N_2S_2	Non-heme	Primary Equatorial	Experimental	96
$[Fe(IV)O(X)]^{2+}$ X = N_4S_1 and N_5	Non-heme	Primary Axial + Equatorial	Experimental + Computational	97
$[Fe(IV)O(TMC)(CH_3CN)]^{2+}$ TMC = N_4 and N_3O_1	Non-heme	Primary Equatorial	Experimental + Computational	98
$[Fe(IV)O(X)]^{2+}$ X = N4Py, L1, and L2	Non-heme	Secondary	Experimental	99
$Fe(IV)O(TMC)(CH_3CN)]^{2+}$ n = 13 and 14	Non-heme	Secondary	Experimental	100

Our understanding of such systems needs to grow in order to further shed light on their sophisticated nature and their essential role in biomimetic chemistry as many complexes still require in-depth study, particularly from a computational perspective. These insights can guide the rational design and optimisation of catalysts with enhanced performance and selectivity.

1.6 Research Gap

Regarding this proposition, there are two ways to perceive the gap in exploration.

1) Primarily, there are enormous experimental investigations available in the literature on the study of M=O based species as Fe^{n+}=O assigned to carry out diversified chemical reactions. Yet only the experimental studies are not enough to examine the all-possible pathways and keen mechanistic details of such complexes. This problem can be overcome by insightful computational mechanistic and kinetics investigations alongside the experimental results which also helps in corroborating the achieved results.

2) Secondly, the theoretical investigations already available do not meet the ever-growing demand for new potential enzyme mimics of the sort that need to be tremendously investigated. Our goal in this thesis will be to outline the ways in which these mechanisms may work for these potential metal oxo species.

Our studies will involve thorough theoretical investigations. Further, experimental executions to uphold these results may also be done, although our results, even solely computational, will surely be suitable to prognosticate the said inspections profoundly. This will provide experimentalists with a direction towards possible novel complexes in this field.

1.7 Objectives

The below mentioned objectives will be considered in the following disquisition:

1. Computational study of the reactivities as well as mechanisms of metal oxo complexes with commutes in ligand architecture.

2. Computational study of the out turns of chemical reactivities with ligand donor atom replacement in the coordination sphere of the metal oxo species.

References

1. B.M. Gardner, C.C.C.S. Johansson and T.J. Colacot, *Industrial Milestones in Organometallic Chemistry*, **2020**, 1-22.
2. B. McCloy, *Some Applications of Transition Metal Complexes*, **1995**.
3. M. L. Crawley and B. M. Trost, *Applications of Transition Metal Catalysis in Drug Discovery and Development: An Industrial Perspective*, **2012**.
4. V. A. Larson, B. Battistella, K. Ray, N. Lehnert and W. Nam, *Nat. Rev. Chem.*, **2020**, 4, 404–419.
5. S. Sahu and D. P. Goldberg, *J. Am. Chem. Soc.*, **2017**, 138, 11410–11428.
6. E. Masferrer-Rius, M. Borrell, M. Lutz, M. Costas and R. J. M. Klein Gebbink, *Adv. Synth. Catal.*, **2021**, 363, 3783–3795.
7. K. Rydel-Ciszex, *Reac. Kinet. Mech. Cat.*, **2021**, 133, 579–600.
8. E. B. Bauer, *Isr. J. Chem.*, **2017**, 57, 1131–1150.
9. B. Mondal, L. Roy, F. Neese and S. Ye, *Isr. J. Chem.*, **2016**, 56, 763–772.
10. M. Guo, T. Corona, K. Ray and W. Nam, *ACS Cent. Sci.*, **2019**, 5, 13–28.
11. K. Rydel Ciszex, T. Pacześniak, I. Zaborniak and P. Błoniarz, K. Surmacz, A. Sobkowiak, P. Chmielarz, *Processes*, **2020**, 8, 1683.
12. A. J. Jasniewski and L. Que, *Chem. Rev.*, **2018**, 118, 2554-2592.
13. F. Weigend, *Phys. Chem. Chem. Phys.*, **2006**, 8, 1057–1065.
14. J. C. Hsieh, *Chem. Rec.*, **2021**, 21, 3370–3381.
15. W. Nam, *Acc. Chem. Res.*, **2007**, 40, 522–531.
16. T. Z. H. Gani and H. J. Kulik, *ACS Catal.*, **2018**, 8, 975−986.
17. K. M. Altus and J. A. Love, *Commun. Chem.*, **2021**, 4, 1–11.
18. C. Krebs, D. G. Fujimori, C. T. Walsh and J. M. Bollinger, in *Accounts of Chemical Research*, **2007**, 40, 484–492.
19. S. Shaik, D. Kumar, S. P. de Visser, A. Altun and W. Thiel, *Chem. Rev.*, **2005**, 105, 2279–2328.
20. G. F. Hendry and T. G. Jones, *J. Med. Gene.*, **1980**, 17, 1-14.
21. F. Ogliaro, M. Filatov and S. Shaik, *Eur. J. Inorg. Chem.*, **2000**, 2455–2458.
22. K. L. Stone, R. K. Behan and M. T. Green, *Proc. Natl. Acad. Sci. U. S. A.*, **2005**, 102, 16563–16565.
23. D. Mandal, D. Mallick and S. Shaik, *Acc. Chem. Res.*, **2018**, 51, 107–117.
24. M. S. Liao, J. D. Watts and M. J. Huang, *J. Phys. Chem. A*, **2005**, 109, 7988–8000.
25. S. Shaik, D. Kumar, S. P. de Visser, A. Altun and W. Thiel, *Chem. Rev.*, **2005**, 105, 2279–2328.
26. D. Mallick and S. Shaik, *J. Am. Chem. Soc.*, **2017**, 139, 11451−11459.
27. A. Mukhopadhyaya and Md E. Ali, *J. Phys. Chem. A*, **2024**, 128, 12, 2339–2348.
28. K. M. Paolesse, R. Kadish, K. M. Smith and R. Guilard, *Porphyr. Handbook.*, **2000**, 2, 201–232.
29. P. Afanasiev, E. V. Kudrik, F. Albrieux, V. Briois, O. I. Koifman and Alexander B. Sorokin, *Chem. Commun.*, **2012**, 48, 6088–6090.
30. E. I. Solomon, T. C. Brunold, M. I. Davis, J. N. Kemsley, S.-K. Lee, N. Lehnert, F. Neese, A. J. Skulan, Y.-S. Yang, J. Zhou, *Chem. Rev.*, **2000**, 100, 235–349.

31. C. Wegeberg, M. L. Skavenborg, A. Liberato, J. N. McPherson, W. R. Browne, E. D. Hedegård and C. J. McKenzie, *Inorg. Chem.*, **2021**, 60, 1975–1984.
32. J. L. Lee, D. L. Ross, K. S. Barman, J. W. Ziller and A. S. Borovik, *Inorg. Chem.*, **2021**, 60, 13759–13783.
33. G. Mukherjee, J. K. Satpathy, U. K. Bagha, M. Q. E. Mubarak, C. V. Sastri and S. P. De Visser, *ACS Catal.*, **2021**, 11, 9761–9797.
34. X. Engelmann, I. Monte-Pérez, and K. Ray, *Angew. Chem., Int. Ed.*, **2016**, 55, 7632–7649.
35. H. Hirao, F. Li, L. Que and K. Morokuma, *Inorg. Chem.*, **2011**, 50, 6637–6648.
36. G. D. Whittemore and C. D. L. Thomas, *Chem. Soc. Rev.*, **2018**, 47, 3595–3614.
37. M. Kumar, M. K. Gupta, M. Ansari and A. Ansari, **2024**, 4349–4362.
38. A. Katoch and D. Mandal, *Dalton Trans.*, **2022**, 51, 11641–11649.
39. A. Katoch and D. Mandal, *Dalton Trans.*, **2023**, 53, 2386–2394.
40. L. Kaur and D. Mandal, *Inorganica Chim. Acta*, **2024**, 572, 122292.
41. L. Kaur and D. Mandal, *Inorg. Chem.*, **2022**, 61, 14582–14590.
42. H. Fujii, *Coord. Chem. Rev.*, **2002**, 226, 51–60.
43. A. R. McDonald and L. Que, *Coord. Chem. Rev.*, **2013**, 257, 414–428.
44. D. Schröder, S. Shaik and H. Schwarz, *Acc. Chem. Res.*, **2000**, 33, 139–145.
45. H. Schwarz, S. Shaik, *Acc. Chem. Res.*, **2000**, 33, 139–145.
46. S. Fukuzumi, Y. M. Lee and W. Nam, *Dalton Trans.*, **2019**, 48, 9469–9489.
47. J. Cho, R. Sarangi and W. Nam, *Acc. Chem. Res.*, **2012**, 45, 1321–1330.
48. W. Nam, *Acc. Chem. Res.*, **2007**, 40, 522–531.
49. S. Shaik, S. Cohen, Y. Wang, H. Chen, D. Kumar and W. Thiel, *Chem. Rev.*, **2010**, 110.
50. R. P. Hausinger, *Crit. Rev. Biochem. Mol. Biol.*, **2004**, 39, 21–68.
51. M. L. Matthews, C. M. Krest, E. W. Barr, F. H. Vaillancourt, C. T. Walsh, M. T. Green, J. M. Bollinger, *Biochemistry.*, **2009**, 48,
52. A. J. Panay, M. Lee, C. Krebs, J. M. Bollinger Jr, and P. F. Fitzpatrick, *Biochemistry.*, **2011**, 50, 1928–1933.
53. S. J. Lippard, J. P. T. Silverman, *Chem. Rev.*, **2015**, 115, 717–748.
54. R. P. Hausinger, *Crit. Rev. Biochem. Mol. Biol.*, **2004**, 39, 21–68.
55. J. C. Price, E. W. Barr, B. Tirupati, J. M. Bollinger and C. Krebs, *Biochemistry*, **2003**, 42, 6795–6806.
56. J. M. Bollinger, J. C. Price, L. M. Hoffart, E. W. Barr and C. Krebs, *Eur. J. Inorg. Chem.*, **2005**, 4245–4254.
57. X. Shan and L. Que, *J. Inorg. Biochem.*, **2006**, 100, 421–433.
58. W. Nam, *Cytochrome P450. Comprehensive Coordination Chemistry II.*, **2004**, 281–307.
59. X. Li, V. Postils, W. Sun, A. S. Faponle, M. Sol, Y. Wang, W. Nam and S. P. de Visser, *Chem. Eur. J.*, **2017**, 23, 6406–6418.
60. P. R. O. de Montellano, *Curr. Opin. Chem. Biol.*, **2000**, 4, 221–227.
61. E. Kent Barefield, *Coord. Chem. Rev.*, **2010**, 254, 1607–1627.
62. D. J. Lowe, R. N. Thorneley, *Biochem. J.*, **1984**, 224, 877–886.
63. R. N. Thorneley, D. J. Lowe, *Biochem. J.*, **1984**, 224, 903–909.

64. J. U. Rohde, J. H. In, M. H. Lim, W. W. Brennessel, M. R. Bukowski, A. Stubna, E. Münck, W. Nam and L. Que, *Science.*, **2003**, 299, 1037–1039.
65. S. Kal, S. Xu and L. Que, *Angew. Chemie - Int. Ed.*, **2020**, 59, 7332–7349.
66. S. P. de Visser, J. U. Rohde, Y. M. Lee, J. Cho and W. Nam, *Coord. Chem. Rev.*, **2013**, 257, 381–393.
67. Y. M. Lee, S. N. Dhuri, S. C. Sawant, J. Cho, M. Kubo, T. Ogura, S. Fukuzumi and W. Nam, *Angew. Chemie - Int. Ed.*, **2009**, 48, 1803–1806.
68. J. Kaizer, E. J. Klinker, N. A. Oh, J. Rohde, W. J. Song, A. Stubna, J. Kim, E. Munck, W. Nam and L. Que, *J. Am. Chem. Soc.*, **2004**, 126, 472–473.
69. E. Andris, K. Segers, J. Mehara, L. Rulíše and J. Roithová, *Angew. Chemie*, **2020**, 132, 23337–23344.
70. J. England, J. Prakash, M. A. Cranswick, D. Mandal, Y. Guo, E. Münck, S. Shaik and L. Que, *Inorg. Chem.*, **2015**, 54, 7828–7839.
71. S. T. Kleespies, W. N. Oloo, A. Mukherjee and L. Que, *Inorg. Chem.*, **2015**, 54, 5053–5064.
72. A. Sirjoosingh and S. Hammes-Schiffer, *J. Phys. Chem. A*, **2011**, 115, 2367–2377.
73. J. M. Mayer, *Acc. Chem. Res.*, **2011**, 44, 36–46.
74. J. E. M. N. Klein and G. Knizia, *Angew. Chemie - Int. Ed.*, **2018**, 57, 11913–11917.
75. J. M. Mayer, D. A. Hrovat, J. L. Thomas, W. T. Borden, *J. Am. Chem. Soc.*, **2002**, 124, 11142.
76. H. Park and D. Lee, *Chem. - A Eur. J.*, **2020**, 26, 5916–5926.
77. S. P. de Visser, *J. Am. Chem. Soc.*, **2006**, 128, 15809–15818.
78. D. Usharani, D. Janardanan, C. Li and S. Shaik, *Acc. Chem. Res.*, **2013**, 46, 471–482.
79. H. Chen, W. Lai and S. Shaik, *J. Phys. Chem. Lett.*, **2010**, 1, 1533–1540.
80. C. Geng, S. Ye and F. Neese, *Angew. Chemie - Int. Ed.*, **2010**, 49, 5717–5720.
81. H. Hirao, D. Kumar, L. Que, Jr., S. Shaik, *J. Am. Chem. Soc.*, **2006**, 128, 8590–8606.
82. G. M. Jones, B. A. Smith, J. K. Kirkland, and K.D. Vogiatzis, *Inorg. Chem. Front.*, **2023**, 10, 1062-1075.
83. S. P. de Visser, *J. Am. Chem. Soc.*, **2006**, 128, 15809–15818.
84. S. Shaik, H. Chen and D. Janardanan, *Nat. Chem.*, **2011**, 3, 19–27.
85. L. Roy, *Chempluschem*, **2019**, 84, 893–906.
86. S. P. de Visser, R. Latifi, L. Tahsini and W. Nam, *Chem. - An Asian J.*, **2011**, 6, 493–504.
87. Z. Tang, Y. Wang, X. Cui, Y. Yang, J. Tian, X. Fei and S. Lv, *Inorganica Chim. Acta*, **2016**, 443, 235–242.
88. J. O. Bigelow, J. England, J. E. M. N. Klein, E. R. Farquhar, J. R. Frisch, M. Martinho, D. Mandal, E. Münck, S. Shaik and L. Que, *Inorg. Chem.*, **2017**, 56, 3287–3301.
89. T. Kamachi, T. Kouno, W. Nam and K. Yoshizawa, *J. Inorg. Biochem.*, **2006**, 100, 751–754.
90. A. R. McDonald, Y. Guo, V. V. Vu, E. L. Bominaar, E. Münck and L. Que, *Chem. Sci.*, **2012**, 3, 1680–1693.
91. D. Kumar, G. N. Sastry and S. P. de Visser, *J. Phys. Chem. B*, **2012**, 116, 718–730.
92. Y. Wang, K. Han, *J. Biol. Inorg. Chem.*, **2010**, 15, 351–359.

93. P. J. Cappillino, J. S. McNally, F. Wang and J. P. Caradonna, *Dalton Trans.*, **2012**, 41, 474–483.
94. C. V. Sastri, J. Lee, K. Oh, J. L. Yoon, J. Lee, T. A. Jackson, K. Ray, H. Hirao, W. Shin, J. A. Halfen, J. Kim, L. Que, S. Shaik and W. Nam, *Proc. Natl. Acad. Sci. U. S. A.*, **2007**, 104, 19181–19186.
95. A. Takahashi, D. Yamaki, K. Ikemura, T. Kurahashi, T. Ogura, T., M. Hada, H. Fujii, *Inorg. Chem.*, **2012**, 13, 51.
96. J. Deutscher, P. Gerschel, K. Warm, U. Kuhlmann, S. Mebs, M. Haumann, H. Dau, P. Hildebrandt, U. P. Apfel and K. Ray, *Chem. Commun.*, **2021**, 57, 2947–2950.
97. J. K. Satpathy, R. Yadav, U. K. Bagha, D. Kumar, C. V. Sastri and S. P. de Visser, *Inorg. Chem.*, **2024**, 1–17.
98. I. M. Pérez, X. Engelmann, Y. M. Lee, M. Yoo, E. Kumaran, E. R. Farquhar, E. Bill, J. England, W. Nam, M. Swart and K. Ray, *Angew. Chemie - Int. Ed.*, **2017**, 56, 14384–14388.
99. M. Mitra, H. Nimir, S. Demeshko, S. S. Bhat, S. O. Malinkin, M. Haukka, J. Lloret-Fillol, G. C. Lisensky, F. Meyer, A. A. Shteinman, W. R. Browne, D. A. Hrovat, M. G. Richmond, M. Costas and E. Nordlander, *Inorg. Chem.*, **2015**, 54, 7152–7164.
100. S. Hong, H. So, H. Yoon, K. Bin Cho, Y. M. Lee, S. Fukuzumi and W. Nam, Dalt. Trans., **2013**, 42, 7842–7845.

Chapter 2

Methodology

2.1 Computational Chemistry

Computational chemistry is a sophisticated branch of chemistry that employs theoretical models and techniques to probe the properties, structures, and reactivity of molecular systems.[1] By utilizing sophisticated algorithms, mathematical techniques, and powerful computational resources, this discipline allows researchers to predict molecular behaviour, investigate reaction pathways, and develop new materials and pharmaceuticals without solely relying on laboratory experiments as shown in Fig. 2.1.

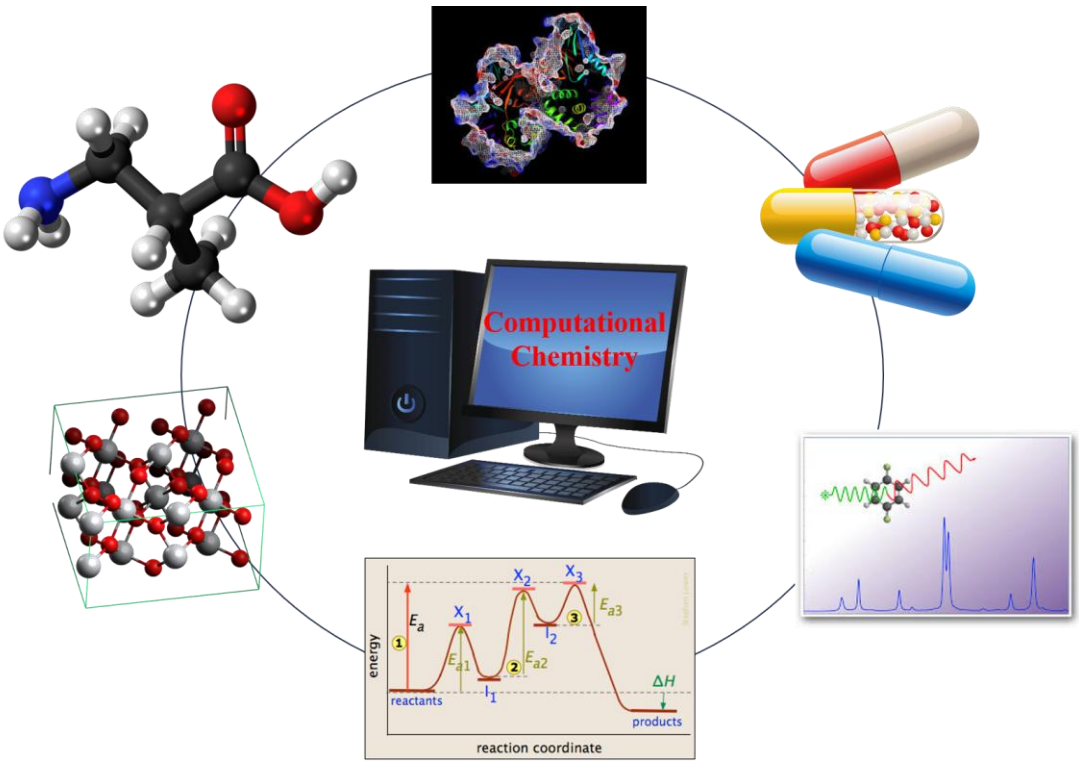

Figure 2.1: A broad overview showcasing the extensive applications of Computational Chemistry.

It is a vital part of contemporary scientific research, offering the ability to study complex chemical systems with accuracy, speed, and cost-effectiveness. Central to this discipline are the principles of quantum mechanics.[2] A wealth of literature is available for in-depth exploration of these fundamental concepts,[3-6] with some key points summarised here.

2.2 Theoretical Details

The Schrodinger wave equation is a base of quantum mechanics, providing a fundamental framework for describing the behaviour of quantum systems.[7-9] Erwin Schrodinger introduced this equation in 1926. The equation is pivotal in determining the wavefunction, Ψ, that

encapsulates every probabilistic insight about the system's state, such as the spatial distribution and energy levels. The simplest way to express Schrodinger equation is the following Equation 1.

$$\hat{H}\Psi = E\Psi \quad (Eq. 1)$$

Wherein $\hat{H}$ represent the Hamiltonian operator, Ψ the wave function, and E depicts energy. While a precise solution to this equation is achievable for basic systems like 1 e^- systems, it cannot be exactly solved for multi-electron systems.[10] As a result, the study of chemically significant systems depends on methods that pursue approximate solutions. The main approximations have been discussed as follows:

2.2.1 Approximations

1. The Born-Oppenheimer Approximation

This approximation was introduced in 1927.[11] The core concept behind this approximation is that the much faster motion of electrons compared to the nucleus allows for the separation of nuclear and electronic movements in molecules.[12] This assumption is reasonable given that the mass of a nucleus, such as a hydrogen atom with a single proton, is around 1800 times greater than that of an e^-. Consequently, the e^- moves within a field created by stationary nuclei having negligible kinetic energy. Mathematically, it can be depicted as Equation 2.

$$\Psi_T = \Psi_e \Psi_n \quad (Eq. 2)$$

where e is for electronic and n for nuclear counterparts.

2. The Hartree-Fock (HF) Approximation

This method is a fundamental ab initio approach used in quantum chemistry to approximate the electronic ψ and energy of a molecular system.[13] It assumes that each e^- moves in an average field originated by all other electrons, rather than interacting directly with each electron; hence, it approximates the many-e^- wave function as a Slater determinant of 1 e^- wave functions (orbitals).[14]

This method solves the H-F equations, which are evolved from minimising the energy functional w.r.t 1 e^- orbitals. The resulting equation is:

$$\hat{F}\phi_i(r) = \varepsilon_i\phi_i(r) \quad (Eq. 3)$$

where $\hat{F}$ is the Fock operator, are $\phi_i(r)$the molecular orbitals, and ε_i are the orbital energies.

However, despite its status as the standard in ab initio methods, the absence of electron-electron correlation limits the accuracy of its results, thereby necessitating a deeper exploration of alternative methods.[15]

3. Post HF methods

These methods are advanced techniques enhanced for better accuracy of molecular calculations by addressing the limitations of the Hartree-Fock approximation, particularly its lack of electron correlation, which refers to the phenomenon where the movements of electron pairs in atoms or molecules are interconnected. The equation that best describes it is:

$$E_{Cor} = E_T - E_{HF} \quad (Eq. 4)$$

These techniques include:

a) Moller Plesset Perturbation Theory (MPn)

In MPn methods, such as MP2, the H-F wave function serves as an initial stage, and then perturbation theory is used to refine the calculations to better depict electron corelations. This approach was initially outlined by Moller and Plesset[16] in 1934 and later evolved in1975.[17,18.]

b) Configuration Interaction (CI)

These methods address electron correlation by considering multiple electronic configurations.[19,20] The key idea is to include a linear combination of Slater determinants, not just the HF determinant. By including both the ground state and excited states, CI provides a more accurate account of how electrons interact with each other.

Post-HF methods involve complex calculations that scale poorly with system size. For instance, the computational price of these methods typically rises rapidly with the number of e^- and basis functions, often following a steep polynomial scaling.[21] This makes them impractical for large molecules or systems with many atoms. This paved the way for other methods which can offers a more balanced approach between computational efficiency and accuracy.

4. DFT

Unlike conventional techniques that resolve the Schrodinger equation by addressing wave functions, DFT reformulates the problem in terms of electron density.[22] It investigates the electronic structure of many-body systems by solving the Kohn-Sham equations to obtain the electron density. As depicted in Fig. 2.1.

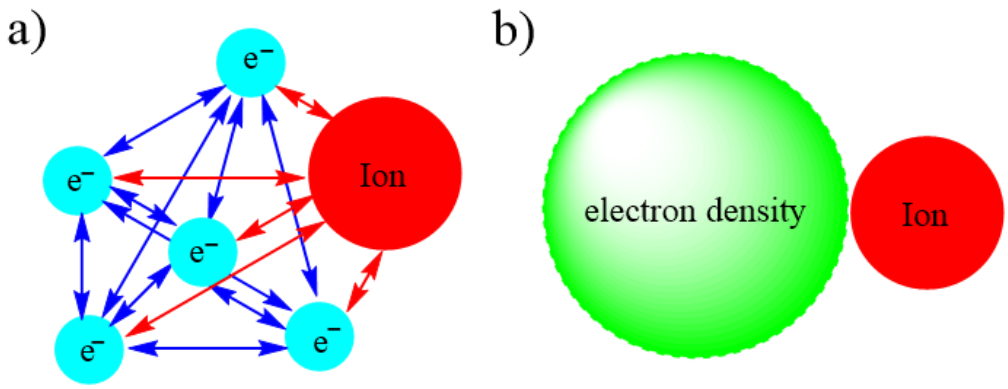

Figure 2.2: a) Many bodies perspective, and b) DFT perspective

The foundation of this is built upon two theorems[22] as elaborated below.

i) Hohenberg-Kohn Theorems

These fundamental theorems laid the groundwork for current DFT. The 1st theorem implies that the G.S. electron density contains every insight about the system's external potential and, therefore, about the system's Hamiltonian. This means that the many-e^- wave function and all observable properties can, be derived from the ρ alone. Mathematically, it is expressed as follows:

$$E_O = E_O[\rho] \quad (Eq. 5)$$

Eo stands for the lowest energy state of an e^-.

Second theorem further, establishes that the correct G.S. electron density minimises the total energy functional. However, since the exact form of the energy functional, particularly the kinetic energy and exchange-correlation energy, was unknown and very difficult to approximate directly. Kohn-Sham Theorems become necessary to be inculcated as follows.

ii) Kohn-Sham Theorems

Kohn and Sham introduced the idea of a theoretical system of non-interacting e^- that has the same G.S. electron density as the original interacting system.[23] Kohn-Sham equations are much simpler and provide a practical route.

One of the primary benefits of DFT is its computational efficiency; by emphasising on the ρ rather than the many-body wave function, it reduces the complexity and cost of calculations compared to traditional methods.[24,25] Additionally, it strikes a favourable balance between precision and computational requirements; hence has been employed exclusively in this thesis.

2.2.2 Functionals

In DFT, a functional refers to a mathematical expression that describes how the energy of a system depends on the ρ. These functionals are used to approximate the exchange-correlation energy. There are various types of functionals, each designed to handle different aspects of electron correlation and exchange interactions.[26]

Commonly used categories include:

1. Local Density Approximation

LDA is one of the most popular and commonly used approximations for better describing the exchange-correlation functional.[27] It assumes the exchange-correlation energy density at a point relies only on the ρ at that point. It is often used when electron density is relatively uniform.

2. Generalised Gradient Approximation

GGA28, is an improved method for calculating the exchange-correlation functional. It incorporates not only the ρ but also its gradient, providing improved accuracy for systems with varying electron densities.[28,29] GGA functionals are generally more accurate than LDA for a wider range of chemical systems. Two frequently employed GGA functionals include the Becke (B) exchange functional[30] and the Lee-Yang-Parr (LYP) correlation functional.[31] Despite their improvements over LDA, GGA functionals still have limitations. For instance, they may not accurately describe dispersion interactions (van der Waals forces) or systems with strong electron correlation effects.

3. Hybrid functionals

These functionals blend exact exchange with the exchange-correlation energy derived from density functional approximations. Among the hybrid functionals, B3LYP (where 3 is 3-parameter) stands out as one of the most popular and effective.[32] Specifically, B3LYP uses:

a) Becke's 3-Parameter Functional: This part mixes exact Hartree-Fock exchange with gradient-corrected exchange contributions, providing a refined treatment of exchange interactions.

b) LYP Correlation Functional: This component enhances the description of electron correlation effects, improving accuracy compared to simpler density approximations.

c) Optimised Parameters: B3LYP uses specific parameters to balance the amount of exact exchange and other functional components, optimizing the performance for a variety of systems.

B3LYP is a commonly used hybrid exchange-correlation B3LYP functional demonstrating exceptional concurrence with experimental findings in multiple instances.[33,34] This functional B3LYP is successful in various contexts for the modelling of C-H activation reactivity catalysed by Fe-O complexes.[35-37] It has proven its potential specifically, on the TMC macrocycle.[38-40] Also, a rigorous benchmark concluding that B3LYP functional performs the best among the functionals is avaialable[41]; hence, we have chosen this functional in particular throughout our studies.

2.2.3 Basis Set

A basis set refers to an agglomeration of basis functions representing a molecular orbital. These functions serve as a basis for expanding the molecular orbitals, thereby enabling the approximation of electronic wave functions.[42] In general, with the increment in the number of basis functions in a basis set, higher accuracy is shown but it rises up the computational expense balance as well. So, attaining the correct balance between the two is crucial. STOs and GTOs are the most widely used basis functions when constructing basis sets.

1. STO

STOs are the exact description of hydrogen-like radical functions and contains factor of $e^{-\zeta r}$, where ζ is the effective charge of nucleus and r is distance between the electron and the atomic nucleus.[43,44] The minimal basis set represents each atomic orbital with a single STO or CGF. For eg, keeping it bare minimum, a single 1s basis function represents a H atom, while 5 basis functions represent a C atom, such as 1s, 2s, and 3-2ps.i. e p_x, p_y and p_z.

2. GTO

GTOs are functions where the radial part is a Gaussian function i.e., they have a radial dependency $e^{-\zeta r2}$.[45] GTOs decay as a Gaussian function with distance from the nucleus, which is not as physically accurate as the exponential decay of STOs.

STOs are more physically accurate for describing atomic orbitals but are computationally expensive to use because of the difficulty in evaluating molecular integrals. Whereas the GTOs although being less physically accurate on their own but are much easier to handle computationally. To achieve the necessary accuracy, GTOs are often used in linear combinations to approximate STOs in quantum chemistry calculations.

3. Split Valence Basis Set

These are expanded versions which >1 STO or CGF with different orbital exponents is utilised to define the valence orbitals.[46] Generally, valence orbitals are of more relevance chemically because core orbitals are more or less unaffected. So, these valence orbitals being of primary importance are usually split to provide a better description. This means that a single basis function represents core orbitals, whereas two or more basis functions represent valence orbitals. To exemplify, in the 6-31G basis set, wherein core orbitals are depicted by 1 CGF (6 primitive GTOs) and valence orbitals by 2 basis functions: one CGF (3 primitive GTOs, and 1 primitive Gaussian function)

2.2.4 Additional Functions

1. Polarisation Functions

These increase the accuracy of the basis set since the orbitals have enhanced flexibility. Taking a H atom with s-type orbitals and spherically symmetric functions for significance, its electron dispersion is almost never spherical, especially in a molecular system. Thus, the addition of p-type functions causes the orbital to shift, providing a more accurate representation of the electron distribution. Similarly, any number of higher-order angular momentum functions can be applied to the atoms of a system. Pople-type basis functions[47] include polarization functions by incorporating a '*' or extra functions in parenthesis. A single '*' represents that all atoms other than H receive a single set of polarization functions, whereas a '**' indicates that all atoms receive polarization functions. Such as, 6-31G** and 6-31G(d,p).

2. Diffuse Functions

These are added for the purpose of increasing radial distribution and allowing orbitals to extend further from the nucleus.[48,49] Incorporating diffuse functions is crucial for characterising weakly bound systems, including anions, excited states, and non-equilibrium geometries with stretched bonds and intermolecular interactions. For example, hydrogen bonding, since the electrons are less securely bonded. These are symbolised by a '+', as in 6-31+G.single '+' indicates the addition of a diffuse function to rest of the atoms, while a double '+' indicates the addition of diffuse functions to all atoms.

2.2.5 Solvation models

Since, reactions take place in solution rather than the gas phase, solvation models in computational chemistry are essential.[50-52] These accurately simulate the behaviour of molecules in condensed solvent phases. Solvation can be addressed computationally using two

fundamental approaches: explicit and implicit methods[53] as depicted in Fig. 2.3. Explicit solvation, also referred as micro solvation involve surrounding the solute molecule with solvent molecules[54] whereas the Implicit solvent models treat the solvent as a continuous medium rather than discrete molecules[54].

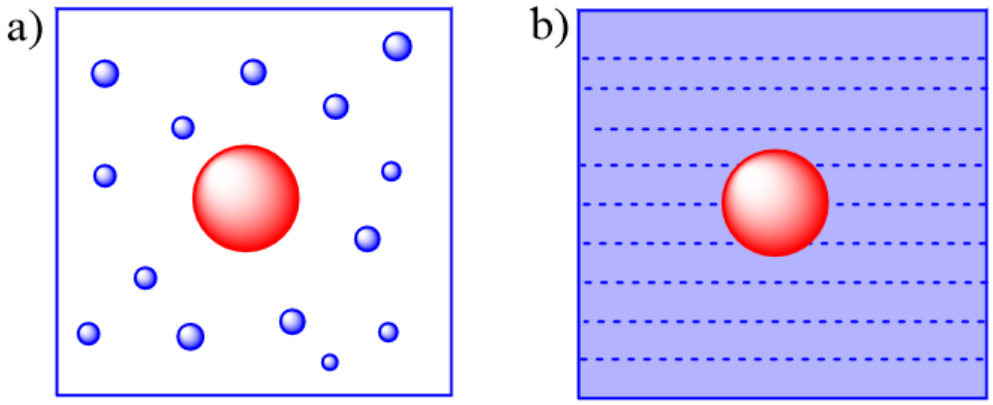

Figure 2.3: Depiction of solvent models a) Explicit and b) Implicit.

Latter are often used in conjunction with quantum mechanical calculations and are computationally less demanding. We have used SCRF models in our thesis to calculate the effect of a solvent on a solute by treating the solvent as a reaction field that polarises the solute's charge distribution.[55] Some examples include CPCM where the solute is modelled as a molecular cavity embedded in the continuum, and the solvent's effect is represented by the polarizable surface surrounding this cavity.[56] Another example includes SMD which is designed to model solvation effects based on the density of the solute and solvent.[57] This model uses empirical data and parameterizations to estimate solvation energies and properties from the solute's electronic density and solvent characteristics.

2.2.6 Quantum Mechanical Tunneling

Quantum mechanics permits particles such as protons or hydrogen atoms to traverse potential barriers that would be insurmountable based on classical energy considerations.[38] This phenomenon arises from the wave-like nature of particles, which allows them to exhibit a probabilistic behaviour rather than deterministic trajectories. As a result, particles can "tunnel" through energy barriers, effectively bypassing the classical requirement to possess sufficient kinetic energy to overcome the barrier.[58-60] This quantum mechanical effect is known as tunneling as shown in Fig. 2.4 and it enables particles to penetrate potential barriers that they would not be able to cross if their behaviour were governed solely by classical physics.

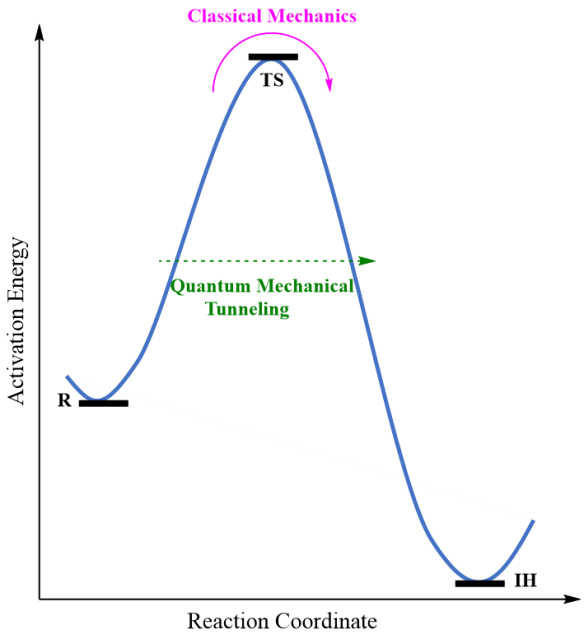

Figure 2.4: Classical representation of tunneling, where R, TS, and IH represent Reactant, Transition State and Intermediate along the reaction coordinate.

The Eckart tunneling calculations were performed where the Eckart-based method employs an analytical potential energy function that is fitted using the computed and zero-point vibrational energy (ZPVE) corrected energies of the R, P, and TS, along with the imaginary frequency of IRC in mass-weighted coordinates.[61] The κ is determined by integrating the barrier penetration probability as a Boltzmann-averaged function of the energy. The impact of this transmission coefficient κ on the activation barrier is given by the Equation 6:

$$\Delta\Delta E^{\ddagger}_{tun} = -RT \ln \kappa(T) \quad (Eq.\ 6)$$

where R = universal gas constant, T = absolute temperature.

2.3 Tools

The interest in the computational field is fuelled by the availability of widely-used tools for Quantum chemical calculations, visualisation and analysing. The selection of these tools is based on criteria such as cost, performance, usability, and time delivery. In our studies presented in this thesis, preeminent steps include geometry optimisation, frequency expounds and thermochemistry calculations with the help of Gaussian 16.[62] It can perform a variety of electronic structure calculations using DFT methods. We have used a wide range of visualisation tools, such as Gaussview[63] and Chemcraft[64] to investigate the finer details of structural factors like bond lengths, angles, atomic charge shifts, and spin densities. Furthermore, additional computations, such as orbital analysis, have been performed to gain a deeper understanding of the mechanical details. Kinetic software such as KiSThelP has also

been used to further shed light on tunneling.[65] Further, softwares such as Multifwn can be used in inspections such as for studying non covalent Interactions.[69] All these steps and tools have been summarised in Fig. 2.5.

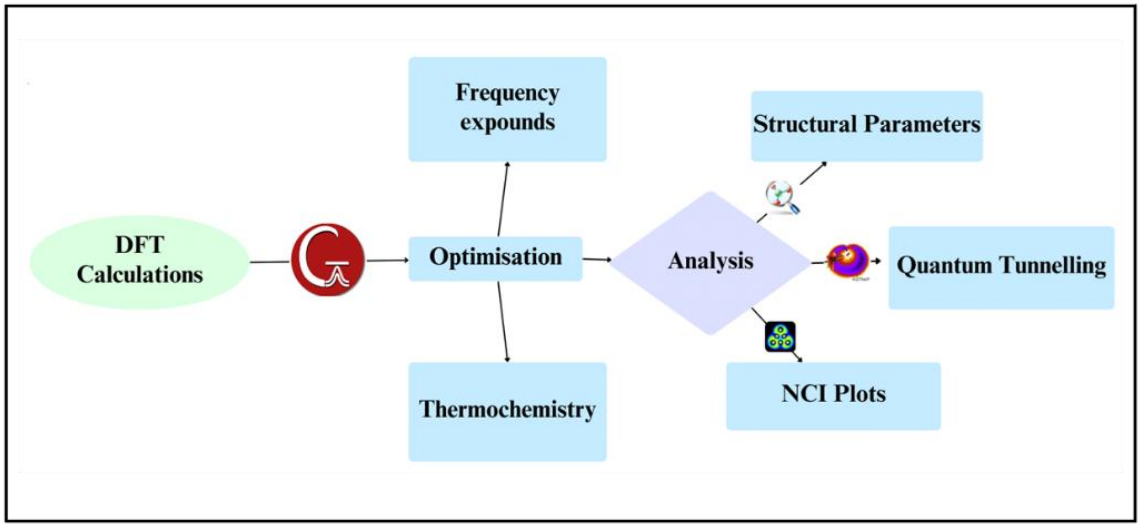

Figure 2.5: Overview of the steps and tools used in the thesis.

References

1. Jensen, *Introduction to Computational Chemistry*, 2nd ed, John Wiley and Sons, **2007**.
2. D. B. Cook. *Handbook of Computational Quantum Chemistry*. Dover Publications, **2005.**
3. R. G. Parr and W. Yang, *Density-Functional Theory of Atoms and Molecules*, Oxford University Press, **1995**.
4. David C. Young. *Computational Chemistry: A Practical Guide for Applying Techniques to Real World Problems*. John Wiley & Sons, **2001.**
5. E. G. Lewars., *Computational Chemistry: Introduction to the Theory and Applications of Molecular and Quantum Mechanics*, 3rd ed. Springer., **2016.**
6. C. J. Cramer. *Essentials of Computational Chemistry: Theories and Models*. John Wiley & Sons, **2004.**
7. E. Schrodinger, *Ann. Phys.*, **1926,** 384, 361–376.
8. A. Szabo, N. S. Ostlund, *Modern Quantum Chemistry: Introduction to Advanced Electronic Structure Theory*, Dover Publications, **1996**.
9. P. W. Atkins, R. S. Friedman, *Molecular Quantum Mechanics*, Oxford University Press, **2011.**
10. I.N. Levine**,** *Quantum Chemistry*, 7th ed, Pearson, **2013.**
11. M. Born, J. R. Oppenheimer, *Ann. Phys.* **1927,** 84, 457–484.
12. B. T. Sutcliffe, R. G. Woolley, R. G. , *J. Chem. Phys.* **2012,** 137, 22A544.
13. D. R. Hartree, *Proc. Camb. Philol. Soc.* **1928**, 24, 89-110.
14. C.C.J. Roothaan**,** *Rev. Mod. Phys.* **1951,** 23, 69–89.
15. R. J. Bartlett and M. Musiał, *Chem. Rev.*, **2007**, 107, 4866-4896.
16. C. Moller and M. S. Plesset, *Phys. Rev.*, **1934**, 46, 618–622.

17. J. S. Binkley, J. A. Pople, *J. Chem. Phys*., **1975**, 63, 754-762.
18. J. F. Stanton and R. J. Bartlett, *J. Chem. Phys*., **1993**, 98, 7027-7033.
19. H. F. Schaefer and W. J. Hehre, *J. Chem. Phys*., **1969**, 51, 2375-2383.
20. M. Shavitt, *Mol. Phys*., **1998**, 94, 3-39.
21. P. Pulay, *Chem. Phys. Lett.*, **1983**, 100, 151-154.
22. P. Hohenberg and W. Kohn, *Phys. Rev*., **1964**, 136, B864-B871.
23. W. Kohn and L. J. Sham, *Phys. Rev*., **1965**, 140, A1133-A1138.
24. J. P. Perdew and Y. Wang, *Phys. Rev. B*, **1992**, 45, 13244-13249.
25. A. D. Becke, *J. Chem. Phys.*, **1995**, 102, 1039-1045.
26. C. E. Dykstra, G. Frenking, K. S. Kim, G.E Scuseria ,*Theory and Applications of Computational Chemistry: The First Forty Years*, Elsevier: Amsterdam, NL, **2005**.
27. D. M. Ceperley and B. J. Alder, *Phys. Rev. Lett*., **1980**, 45, 566-569.
28. J. P. Perdew and Y. Wang, *Phys. Rev. B*, **1986**, 33, 8800-8802.
29. J. P. Perdew, K. Burke, and M. Ernzerhof, *Phys. Rev. Lett*., **1996,** 77, 3865-3868.
30. A. D. Becke, *J. Chem. Phys.*, **1993**, 98, 1372–1377.
31. C.Lee, W.Yang, R. G. P., *Phys. Rev.* **1988**, 37,785–78.
32. A. J. Cohen, P. Mori-Sanchez, and W. Yang, J. *Chem. Phys.*, **2008**, 128, 034112.
33. J. P. Perdew, K. Burke, and M. Ernzerhof, *J. Chem. Phys*., **1996**, 105, 9384-9391.
34. S. C. Chan, Z. Z. Ang, P. Gupta, R. Ganguly, Y. Li, S. Ye and J. England, *Inorg. Chem*., **2020**, 59, 4118–4128.
35. M. J. Baird, A. S. Borovik, and G. M. Bernard, *J. Am. Chem. Soc.*, **2001**, 123, 7106-7112.
36. J. M. D. Smith, R. D. Hall, and R. H. Crabtree, *J. Am. Chem. Soc.*, **2004**, 126, 12412-12420.
37. M. B. Smith, L. M. Schreiber, and J. R. Long, *Coord. Chem. Rev., 2006,* 250, 743-764.
38. D. Mandal and S. Shaik, *J. Am. Chem. Soc.*, **2016**, 138, 2094–2097.
39. M. Kumar, M. K. Gupta, M. Ansari and A. Ansari, *Dalt. Trans*., **2024**, 4349–4362.
40. D. Mandal, D. Mallick and S. Shaik, *Acc. Chem. Res.*, **2018**, 107–117.
41. A. Altun, J. Breidung, F. Neese and W. Thiel, *J. Chem. Theory Comput.*, **2014**, 10, 3807–3820.
42. J. C. Slater, *Phys. Rev.*, **1951**, 81, 385-390.
43. T. H. Dunning Jr., *J. Chem. Phys.*, **1989**, 90, 1007-1023.
44. T. Marino, M. G. Fortino, N. Russo, M. Toscano and M. E. Alberto, *Int. J. Mol. Sci.*, **2021**, 22, 1234-1245.
45. Y. Wang, X. Jin, H. S. Yu, D. G. Truhlar and X. He, *Proc. Natl. Acad. Sci. U. S. A.*, **2017**, 114, 8487–8492.
46. D. E. Woon and T. H. Dunning Jr., *J. Chem. Phys*., **1994**, 100, 2975-2988.
47. J. A. Pople, *Int. J. Quantum Chem.,* **1967**, 1, 269-276.
48. J. R. D. Feller, *J. Chem. Phys.*, **1996**, 105, 6211-6219.
49. L. S. Turner, A. J. Morrison, and J. R. Williams, *Inorg. Chem*., **2022**, 61, 1428-1441.
50. M. J. Frisch, G. W. Trucks, H. B. Schlegel, et al., *J. Chem. Phys.*, **1996**, 104, 6377-6384.
51. L. K. Anderson and H. J. Fisher, *J. Phys. Chem. B*, **2021**, 125, 11632-11643.
52. K. L. Zhang, M. R. Cooper, and P. J. Knight, *Phys. Chem. Chem. Phys*., **2023**, 25,4850-4863.
53. G. A. Voth and A. L. Garcia, *J. Chem. Phys*., **1995**, 102, 663-678.

54. 57 K. Mathew, R. Sundararaman, K. Letchworth-Weaver, T. A. Arias and R. G. Hennig, *J. Chem. Phys*., **2005***,* 123, 164112.
55. A. V. Marenich, R. M. Olson, C. P. Kelly, C. J. Cramer and D. G. Truhlar, *J. Chem. Theory Comput.*, **2007**, 3, 2011–2033.
56. E. L. Moreira, *Int. J. Quantum Chem*., **2013**, 113, 1511-1521.
57. J. M. Thomas and A. R. Cossi, *Chem. Rev.*, **2013**, 113, 845-877.
58. R. H. Fowler and E. A. Guggenheim, *Trans. Faraday Soc.*, **1939**, 35, 155-167.
59. D. Mandal, R. Ramanan, D. Usharani, D. Janardanan, B. Wang and S. Shaik, *J. Am. Chem. Soc.*, 2015, **137**, 722–733.
60. L. Gagliardi, M. J.Behrens, L.T Richards, *Coord. Chem. Rev*., **2019,** 394, 34-47.
61. J. Eckart, *Phys. Rev*., **1930**, 35, 1303-1307.
62. Gaussian 16, Revision C.01, M. J. Frisch, G. W. Trucks, H. B. Schlegel, G. E. Scuseria, M. A. Robb, J. R. Cheeseman, G. Scalmani, V. Barone, G. A. Petersson, H. Nakatsuji, X. Li, M. Caricato, A. V. Marenich, J. Bloino, B. G. Janesko, R. Gomperts, B. Mennucci, H. P. Hratchian, J. V. Ortiz, A. F. Izmaylov, J. L. Sonnenberg, D. Williams-Young, F. Ding, F. Lipparini, F. Egidi, J. Goings, B. Peng, A. Petrone, T. Henderson, D. Ranasinghe, V. G. Zakrzewski, J. Gao, N. Rega, G. Zheng, W. Liang, M. Hada, M. Ehara, K. Toyota, R. Fukuda, J. Hasegawa, M. Ishida, T. Nakajima, Y. Honda, O. Kitao, H. Nakai, T. Vreven, K. Throssell, J. A. Montgomery, Jr., J. E. Peralta, F. Ogliaro, M. J. Bearpark, J. J. Heyd, E. N. Brothers, K. N. Kudin, V. N. Staroverov, T. A. Keith, R. Kobayashi, J. Normand, K. Raghavachari, A. P. Rendell, J. C. Burant, S. S. Iyengar, J. Tomasi, M. Cossi, J. M. Millam, M. Klene, C. Adamo, R. Cammi, J. W. Ochterski, R. L. Martin, K. Morokuma, O. Farkas, J. B. Foresman, and D. J. Fox, Gaussian, Inc., Wallingford CT, **2016.**
63. Gaussian, Inc., GaussView, Version 6, Gaussian, Inc., Wallingford, CT, **2016.**
64. G. A. Andrienko. *Chemcraft Molecular Visualization Program*, version 1.8.
65. T. Lu, F. Chen, *J. Comput. Chem.*,**2012**, 33, 580-592.
66. S. Canneaux, F. Bohr, and E. Hénon, *J. Comp. Chem.*, **2014** ,35, 82-93.

Chapter 3

Role of "S" Substitution on C−H Activation Reactivity of Iron (IV)−Oxo Cyclam Complexes: A Computational Investigation

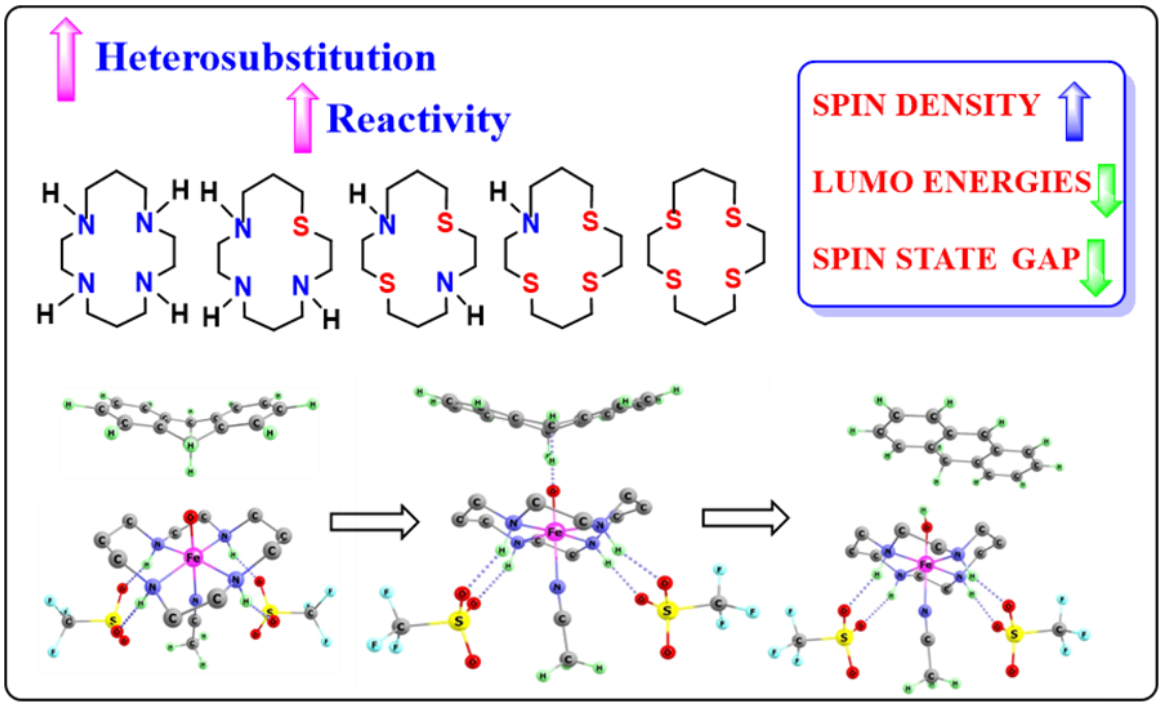

3.1 Introduction

The advancement of transition metal oxo complexes as intermediates in a variety of catalytic reactions has been pivotal in the field of bioinorganic C-H activation chemistry latterly with groups 3 to 10 being extensively explored.[1–9] Fe(IV)=O complexes have been investigated vastly.[10] They act as bio-inspired catalysts for several important reactions such as dioxygen activation and C–H activation resulting in hydroxylation/halogenation/epoxidation, and other products.[11–18] In 2003, the first high-resolution structure of a mononuclear nonheme Fe(IV)=O complex was reported in the reaction of Fe(II)(TMC)$(CF_3SO_3)_2$ (TMC = 1,4,8,11-tetramethyl 1,4,8,11-tetraazacyclotetradecane) and the intermediate was characterised as an Fe(IV)O with Fe–O double-bond character and a triplet (S=1) Fe(IV) ground oxidation state.[19] Since then, a number of mononuclear nonheme iron(IV)-oxo complexes bearing tetradentate N_4 ligand entities have been studied such as TMC, and amino-pyridyl and even porphyrin units.[20–25] TMC is recognised as one of the most popular macrocyclic fragments for the Fe(IV)O complexes

which has been extensively investigated by many experimental and computational groups.[26–28] A number of ligand frameworks which mimic enzyme reactivity have also been reported, demonstrating how altering ligand architecture (axial and equatorial position) leads to increased selectivity and reactivity.[29–31]Multiple investigations on $[(TMC)Fe(IV)O(NCCH_3)]^{2+}$ have been performed largely because the 6th ligand acetonitrile in the axial position is conveniently supplanted by other ligands[32] e.g., N_3^- and SR^- etc wherein rates of hydrogen atom transfer from DHA(Dihydroanthracene) hiked upon the introduction of more electron-donating axial ligands.[33] There are several sulfur-ligated Fe(IV)=O centres also being found as key oxidants in the catalytic cycles of various heme and non-heme iron oxygenases e.g., Cysteine dioxygenase (CDO)[34] that catalyses the transformation of L-cysteine to cysteine sulfinic acid and ergothioneine biosynthesis enzymes (OvoA)[35] etc. Ligation of sulfur atoms has been reported several times as they are suggested to be reactive intermediates for a wide range of chemical transformations including oxygenation[36], hydroxylation[37] and C–S bond formation reactions.[38] Fe(IV)O porphyrin π cation radical (Cpd I) intermediates containing a thiolate ligand trans to the oxo group have been characterised in a number of heme enzymes.[37] A lot of investigations have also been presented related to the replication of CDO active sites towards synthetic analogues. Limberg and his co-workers have synthesised trispyrazolylborato iron cysteinato complex, a model of CDO.[39] The structures and mechanisms of dioxygen activation catalysed by the above complexes have also been reported by Sallmann et.al.,[40] The ligand effects on bio-inspired CDO model complexes have also been characterised.[41] De Visser and his co-workers also reported the S-Oxygenation mechanism catalysed by a CDO Model Complex where cis-Sulfur ligands connected to central metal iron.[42,43]An iron(II) complex bearing an N_3S_2 thioether ligand has been presented by J. Annaraj et al. depicting how S ligations impacted the reactions.[44] (Scheme 3.1(a)). At the outset of a study performed by J. Deutscher et al., a mononuclear oxo iron (IV) complex having 2S ligations at the equatorial position of cyclam ligand has been investigated as a paradigm for S-ligated iron-oxo intermediates in non-heme iron oxygenase's[45] (Scheme 3.1(b)). So, it is quite obvious from the aforementioned studies that 'S' ligation to metal oxo has an important role in the reactivity of the complexes. This expedited the requirement of an intense investigation to generalise the role of 'S' ligation. So, herein, we have presented rigorous density functional theory investigations of the C-H abstraction reactivity of the Fe(IV)O complexes ligated with 4 nitrogen present on the equatorial position of the macrocycle (N_4). The investigations have been extended using derivative complexes obtained by sequential replacement of N by S i.e., N_4, N_3S_1, N_2S_2, N_1S_3, and S_4 (Scheme 3.1(c)).

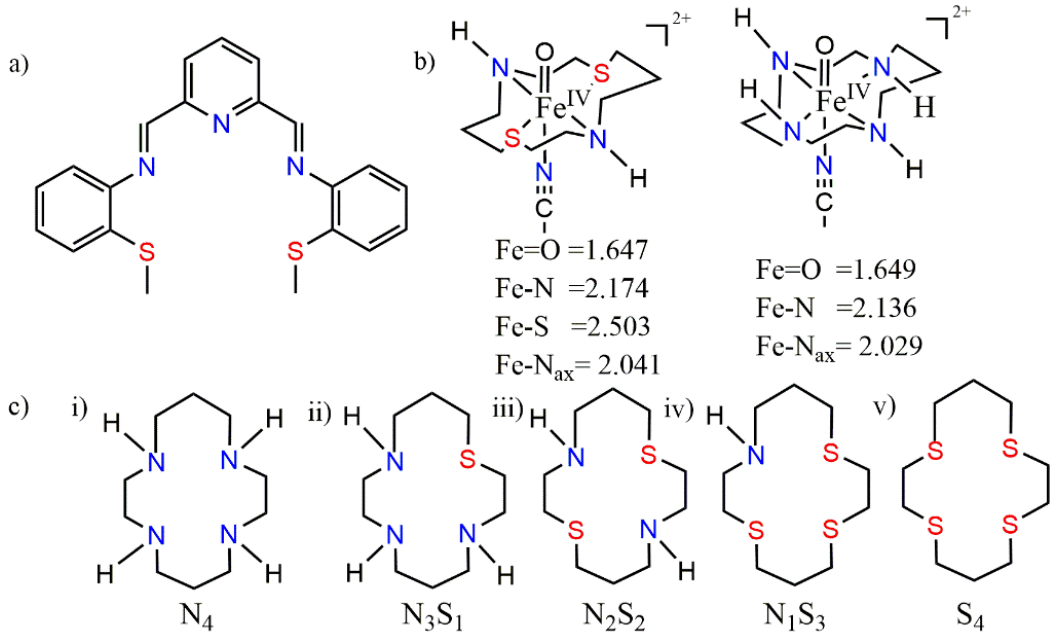

Scheme 3.1: Proposed structures of a) N_3S_2[44] b) N_2S_2 and N_4[45] where parameters for the S=2 states are in Å c) Various frameworks studied from N_4 to S_4.

DHA is used as the general substrate. Detailed mechanistic investigations have also been performed to obtain keen insights into the reactivity towards DHA. Sequential replacement of nitrogen by sulfur which contains 0 to 4 thioether sulfur coordination sites poised cis to the oxo group provided us important insight into how cis-Sulfur coordination influences the reactivity of the Fe(IV)=O complexes. There are many possible factors controlling the reactivity e.g., possible spin state pathway[46], spin density on the abstractor[16], deformation energy to obtain the transition states,[47] etc which have been analysed carefully. Cyclam macrocycle is close to the popular TMC ligands where the methyl groups at 1, 4, 8, and 11 positions of TMC have been substituted by hydrogen atoms. So, we have extended our investigations including iron-oxo-TMC complexes to verify whether they both provide similar trends or not.

3.2 Computational Details

Geometry optimizations for all the species have been conducted using the unrestricted DFT-B3LYP method,[48,49] B3LYP being the functional used (Becke's three-parameter exchange with Lee-Yang and Parr's correlation functional). An extensive benchmark in support of this functional for a model C-H activation reaction catalysed by iron−oxo complexes proves that it provides the best results.[50] We have used the LANL2DZ (for Fe)[51] with ECP and pople's double zeta 6-31G*(for the rest of the atoms)[52,53] basis set labelled as B1. Further energy refinement with the help of single point calculations has also been done using 6-31++G(2d,2p), for all atoms along with ECP containing SDD for iron. (labelled as B2) in presence of acetonitrile

solvent computed using self-consistent reaction field (SCRF) and Truhlar's solvation model density (SMD) approximation.[54,55] An elaborate study of the $[Fe^{IV}(O)N_4Py]^{2+}$ complex has shown that the usage of counterions in order to neutralise the charge of the oxidants caused secondary interactions to vanish[56], so to deal with these effects, here we neutralised the charge of the iron (IV)−oxo reagents with triflate ($CF_3SO_3^-$) counterions huddled at the bottom parts of the axial ligands. Although, the use of both counter ions and solvent is appropriate during optimization, it is found difficult and time-consuming due to the constant movement of counter ions in the presence of the solvent. So, gas-phase optimization in the presence of counter ions and incorporation of solvent effect in single point is followed here which was successfully reported in an earlier C-H activation mechanism catalysed by $[Fe(IV)OTMC]^{n+}$ complexes.[57,58] A subsequent frequency calculation has also been carried out at the same B1 level to confirm the nature of the optimised structures as local minima (no imaginary frequency) or transition states (one imaginary frequency), and to evaluate the zero-point vibrational energy (ZPVE), as well as thermal and entropic corrections to the Gibbs free energy at T = 298 K. An intrinsic reaction coordinate (IRC) calculation has also been carried out to further verify if the transition states are connecting the proper minima or not.[59] Spin natural orbitals have been analysed for the correct identification of the electronic state. All the computations have been performed using Gaussian 16 program packages[60] and for the visualization and the generation of natural orbitals, Chemcraft software has been used.[61] We have used the B3LYP/B2//B3LYP/B1 zero-point corrected energy for the discussion of energetics unless otherwise specified.

3.3 Results and Discussions

3.3.1 Conformational Stability

At first, we performed investigations on the different conformations in terms of the H atom attached to the N donor being syn, jumble, and anti to the oxygen of the Fe=O unit. Results conclude the stability order, anti > syn > mixed for N_4. In case of N_3S_1, again anti-showed better stability. For N_2S_2, the order anti > mixed > syn is seen. However, for N_1S_3 syn conformation was more stable. To have a consistent discussion the lowest energy conformation of all the complexes i.e., anti for N_4, N_3S_1, N_2S_2, and syn for N_1S_3 have been considered to explore their reactivity patterns. However, barriers have also been calculated for anti N_1S_3 conformation to see if there is any variation in the reactivity trend. The geometries along with energies are presented in Fig. 3.1

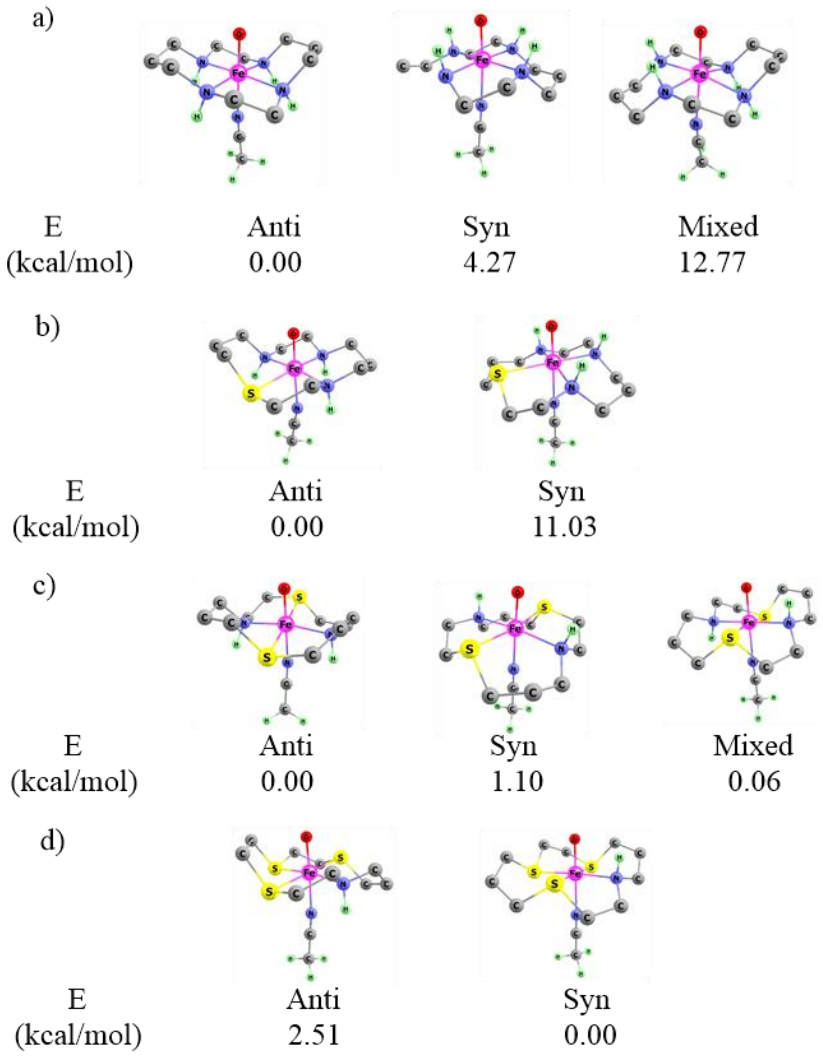

Figure 3.1: The various possible conformations of the complexes in a) N_4, b) N_3S_1, c) N_2S_2 and d) N_1S_3.

3.3.2 Spin State Reactivity and Electron Transfer Pathways

We then moved forward to determine the favourable spin states of the central metal, Fe, as Fe (IV) complexes can have both low spin (S = 1, triplet state) and high spin (S = 2, quintet state) state. The hydrogen atom transfer (HAT) mechanism proceeds through H-abstraction with simultaneous electron rearrangement [62-63] depending on the spin state pathways. The following scheme can explain the HAT mechanism more specifically i.e., hydrogen goes to the O whereas electron transpires to metal d orbital as depicted in Scheme 3.2.

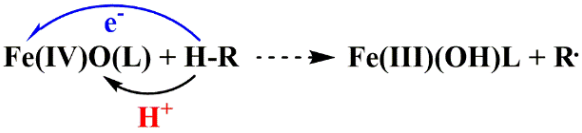

Scheme 3.2: General arrangement of the HAT transfer**.**

The electron rearrangement in both the spin state has already been presented in the Figure 1.6. where we discussed we can have two kinds of paths for this reaction mechanism depending on the spin state.[64–66] The upper panel demonstrated the low spin i.e., S=1 pathways where a β electron from the σ_{C-H} bond is shifted to one of the π* orbital of the central metal – represented as π pathway/trajectory. The lower panel described the high spin path where one α electron from the σ_{C-H} bond of the substrate moves to the σ^*_{dz2} anti-bonding orbital of Fe=O. This pathway is counted as σ pathway or σ trajectory. Generally, for the Fe(IV)O complexes, reactants at the S=2 state possess higher energy compared to S=1 which becomes lower through the transition state implying two state reactivity (TSR).[64-68] The TSR phenomenon sometimes may become more prominent due to the steric inhibition of π trajectory[69] or less prominent in absence of steric congestion.[57,58]

3.3.3 SNO Analysis

To confirm the orbitals involved in the electron transfer for the high spin state S=2 state, a thorough sno analysis has been studied as compiled in Fig. 3.2.

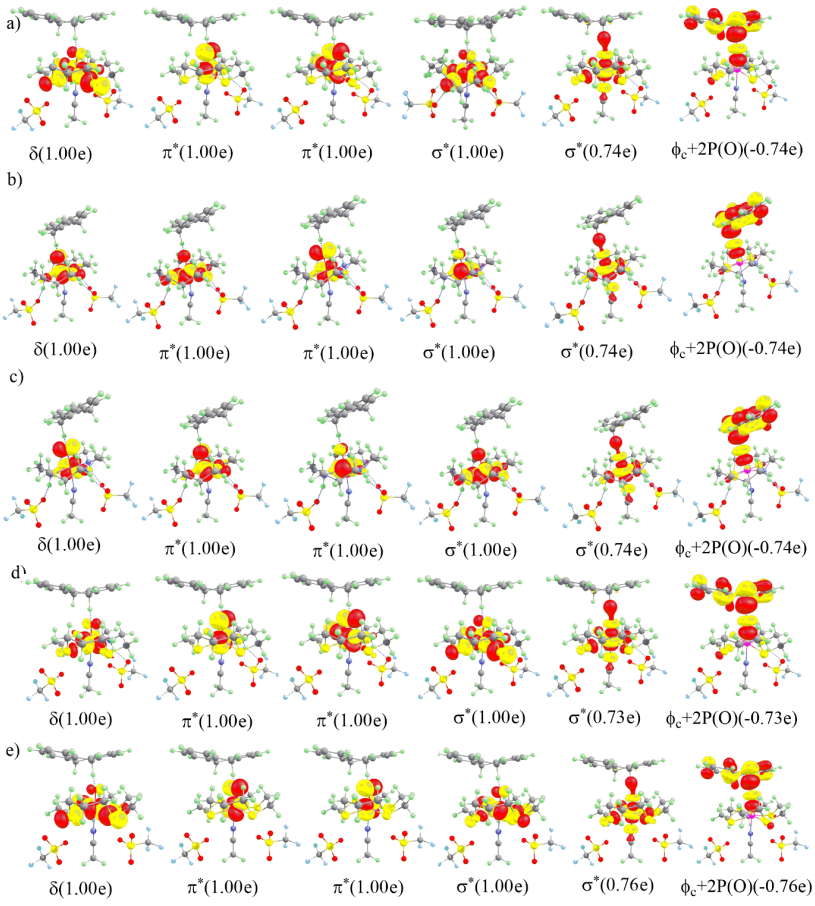

Figure 3.2: Spin Natural orbitals and their occupations in transition states for ^{5}TS of a) N_4 , b) N_3S_1 , c) N_2S_2, d) N_1S_3 and e) is S_4 framework.

3.3.4 Two State Reactivity and Reactivity Trend

The potential energy surface for all the reactions have been collected in Fig. 3.3.

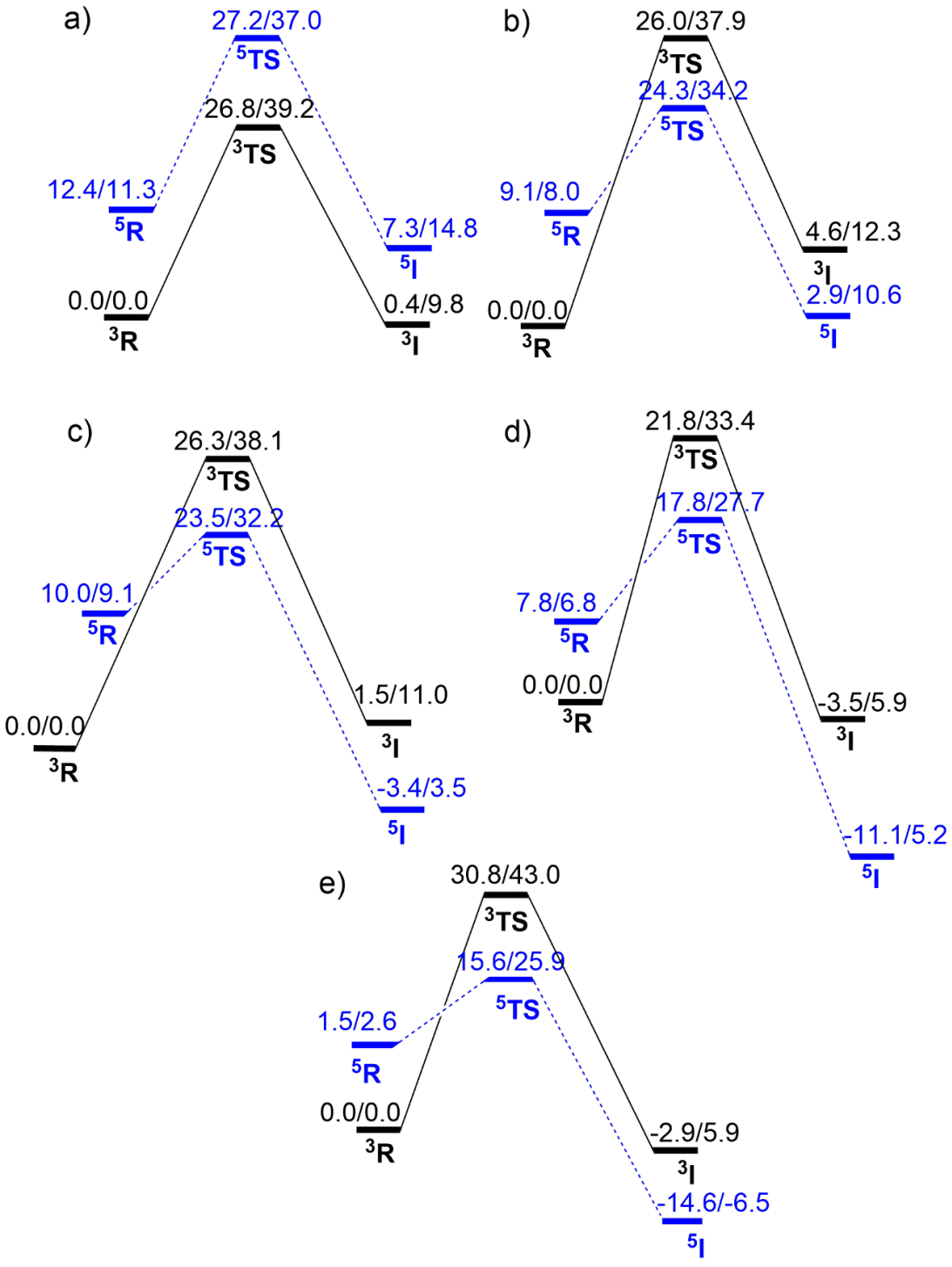

Figure 3.3: The potential energy surface for the C-H activation catalysed by Fe(IV)O complex framed with a) N_4 b) N_3S_1 c) N_2S_2 d) N_1S_3 and e) S_4 macro cyclic ligands. The black and blue line represents the S=1 and S=2 state pathways, respectively. The energy values are given as $\Delta E(B2+ZPE)/\Delta G_{298K}(B2)$. The PESs are plotted with respect to the energy of ^3R + DHA.

In general hydrogen atom abstraction pattern by non-heme Fe(IV)=O complexes, the quintet transition state is found lower in energy than the triplet transition state, due to the favourable increase in exchange interactions on the quintet energy surface over the course of the reaction, a manifestation of the exchange-enhanced reactivity (EER) concept.[70] The current study also shows no exception as the PES reflected that the S=2 pathways are found either almost degenerate with S=1 (26.8 kcal mol^{-1} and 27.2 for S=1 and S=2, respectively) for N_4 or lower than the S=1 pathways in all other complexes. After consideration of the free energy, the TSR pattern is found to be more prominent in the case of N_4 complex too as the S=2 barrier is found lower than the S=1 by ~2.2 kcal mol^{-1}. N_3S_1 and N_2S_2 and S_4 show the same behaviour irrespective of the energy or free energy. For all complexes, the quintet intermediate is found to be more stable as compared to the triplet with respect to the energy or the free energy trends. So, taking into account the higher energy quintet reactant and crossover between the spin states from transition states to the intermediates, it has been concluded that the reactions follow the expected two state reactivity phenomenon wherein rate determining steps proceeds on the surface with spin inversion i.e., from reactants to transition structures. As the quintet state has been found to be more reactive than the corresponding triplet state in all the cases thereby it guides the reaction route. A noteworthy trend has been observed for the barrier of C-H abstractions catalysed by the Fe(IV)=O complexes coordinated with N_4 to S_4 macrocyclic ligands. From Figure 3.3 it is clear that reactivity increases with the replacement of N by S. The trend looks like N_4 (27.2 kcal mol^{-1} or 26.8 kcal mol^{-1} in S=1 state) > N_3S_1 (24.3 kcal mol^{-1}) > N_2S_2 (23.5 kcal mol^{-1}) > N_1S_3 (17.8 kcal mol^{-1}) > S_4 (15.6 kcal mol^{-1}). In free energy also the trend looks same i.e., N_4 (37.0 kcal mol^{-1}) > N_3S_1 (34.2 kcal mol^{-1}) > N_2S_2 (32.2 kcal mol^{-1}) > N_1S_3 (27.7 kcal mol^{-1}) > S_4 (25.9 kcal mol^{-1}). These geometry optimizations have been carried out in the gas phase with single point calculations using solvent acetonitrile. However, to validate the results we have reoptimised for N_4 framework and observed ΔG_{298K}(B2) are identical for the triplet/quintet states in the gas phase (39.2/37.0 kcal mol^{-1}) and solvent phase (39.3/37.7 kcal mol^{-1}), respectively. The barrier for anti N_1S_3 framework for S=2 is observed to be 34.9/32.2 kcal mol^{-1} which is slightly higher compare to its syn form although it fits the aforementioned reactivity trend. Further details for different levels of theory are presented here in Table 3.1 where B1 is 6-31G*/LANL2DZ(Fe) whereas B2 is 6-31++G(2d,2p)/SDD(Fe). Also, G_{Dis}(298K) implies dispersion corrected free energy.

Table 3.1: Relative energies (in kcal mol^{-1}) of oxidants, TS and intermediates computed at different levels of theory.

Reactions	Spin State	Species	B1 + ZPE	B2 + ZPE	G (298K)	G_{Dis}(298K)
N_4	S=1	^{3}R+S	0.0	0.0	0.0	0.0
		^{3}TS	22.7	26.8	39.2	25.8
		^{3}IH	-1.1	0.4	9.8	-1.3
	S=2	^{5}R+S	17.4	12.4	11.3	13.4
		^{5}TS	24.8	27.2	37.0	28.4
		^{5}IH	14.5	7.3	14.8	4.9
N_3S_1	S=1	^{3}R+S	0.0	0.0	0.0	0.0
		^{3}TS	22.9	26.0	37.9	24.9
		^{3}IH	1.4	4.6	12.3	0.9
	S=2	^{5}R+S	13.0	9.1	8.0	10.0
		^{5}TS	20.6	24.3	34.2	21.4
		^{5}IH	3.3	2.9	10.6	-1.7
N_2S_2	S=1	^{3}R+S	0.0	0.0	0.0	0.0
		^{3}TS	17.3	26.3	38.1	23.0
		^{3}IH	-4.5	1.5	11.0	-1.7
	S=2	^{5}R+S	10.7	10.0	9.1	11.4
		^{5}TS	23.6	23.5	32.2	20.6
		^{5}IH	6.1	-3.4	3.5	6.1
N_1S_3(syn)	S=1	^{3}R+S	0.0	0.0	0.0	0.0
		^{3}TS	14.2	21.8	33.4	20.9
		^{3}IH	-4.9	-3.5	5.9	-6.2
	S=2	^{5}R+S	9.4	7.8	6.8	8.0
		^{5}TS	19.9	17.8	27.7	14.6
		^{5}IH	2.5	-11.1	5.2	-8.3
N_1S_3	S=1	^{3}R+S	0.0	0.0	0.0	0.0
		^{3}TS	17.3	23.0	34.9	20.6
		^{3}IH	-4.9	-2.5	7.0	-4.9
	S=2	^{5}R+S	11.1	9.3	8.6	10.5
		^{5}TS	23.6	22.7	32.2	19.7
		^{5}IH	5.8	0.7	8.6	-4.3
S_4	S=1	3R+S	0.0	0.0	0.0	0.0
		3TS	17.0	30.8	43.0	29.6
		3IH	-4.3	-2.9	5.9	-7.6
	S=2	5R+S	12.2	1.5	2.6	4.2
		5TS	24.1	15.6	25.9	14.2
		^{5}IH	5.7	-14.6	-6.5	-20.4

It has also been experimentally reported that cis-thiolate ligation increases the C-H activation reactivity. To further validate our theoretical outcomes, we have also computed the C-H activation energy in accordance with 1 trans and 2 trans structures studied by J. Deutscher et al.,[45](Scheme 3.1b), and results were found in accordance with the experimental one wherein N_2S_2 was more reactive than N_4 unit as shown in the potential energy surface presented in Figure 3.4. Like N_4 in Figure 3.3, this conformation also N_4 has the S=1 state slightly more reactive as compared to the S=2. In contrast to the anti-conformation, here the N_2S_2 shows a more reactive triplet state. This may be due to the steric interaction created by the N-H group. So, in Figure 3.4, only the S=1 state has been presented. The reported experimental activation barrier for 1 trans has been found ~5.1 kcal mol^{-1} lower than the 2 trans complexes whereas our computed outcome shows this value as ~2.0 kcal mol^{-1} for the first step which can be a decent validation of our theoretical outcomes. After H-abstraction, the potential energy surface for desaturation steps has also been computed and presented in Fig. 3.4.

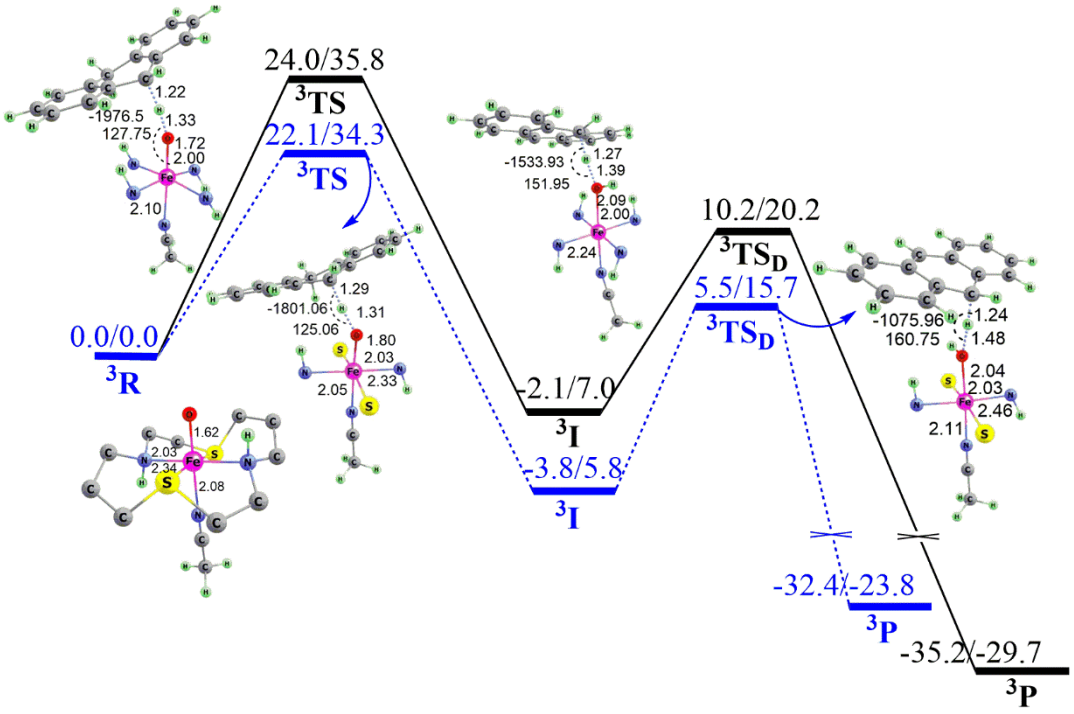

Figure 3.4: Potential energy surface of 1 trans (black) and 2 trans (blue) complexes for C-H activation and desaturation steps. The energy values are given as ΔE(B2+ZPE)/ΔG(B2).

In this step also N_2S_2 is found to be more reactive (5.5 kcal mol^{-1}) as compared to N_4 (10.2 kcal mol^{-1}). One more observation which is important to mention here is that the desaturation steps possess much lower energy of activation as compared to the H-abstraction which proves HAT is the rate determining step and therefore reactivity analysis can be conducted on the basis of the first HAT step. Further details have been presented in Table 3.2.

Table 3.2. Relative energies (in kcal mol^{-1}) of oxidants, TS and intermediates computed at different levels of theory for alternate conformation where B1 is 6-31G*/LANL2DZ(Fe) and B2 is 6-31++G(2d,2p)/SDD(Fe). $G_{Dis}(298K)$ implies dispersion corrected free energy.

Reactions	Spin State	Species	B1 + ZPE	B2 + ZPE	G (298K)	$G_{Dis}(298K)$
N_4	S=1	^{3}R+S	0.0	0.0	0.0	0.0
		^{3}TS	17.7	24.0	35.8	21.6
		^{3}IH	10.1	-2.1	7.0	-4.4
	S=2	^{5}R+S	18.6	14.8	13.7	15.5
		^{5}TS	30.1	27.8	36.5	28.0
		^{5}IH	-26.6	10.1	15.6	6.0
N_2S_2	S=1	^{3}R+S	0.0	0.0	0.0	0.0
		^{3}TS	14.7	22.1	34.3	15.7
		^{3}IH	-6.3	-3.8	5.8	-9.6
	S=2	^{5}R+S	7.0	14.2	14.4	12.7
		^{5}TS	26.7	26.2	36.6	20.2
		^{5}IH	9.0	10.3	19.9	-3.0

3.3.5 Reactions of TMC and S-substituted TMC with DHA

The investigations have been further extended to TMC in order to see if the perceived conclusion i.e., the increment of reactivity by cis Sulfur ligation is valid in that case too or not. We have considered two complexes here, N_4-TMC and N_2S_2-TMC. S_4 complex is mutual in both the TMC and cyclam cases. The computed potential energy surface for the C-H abstraction from DHA is presented in the following Fig. 3.5.

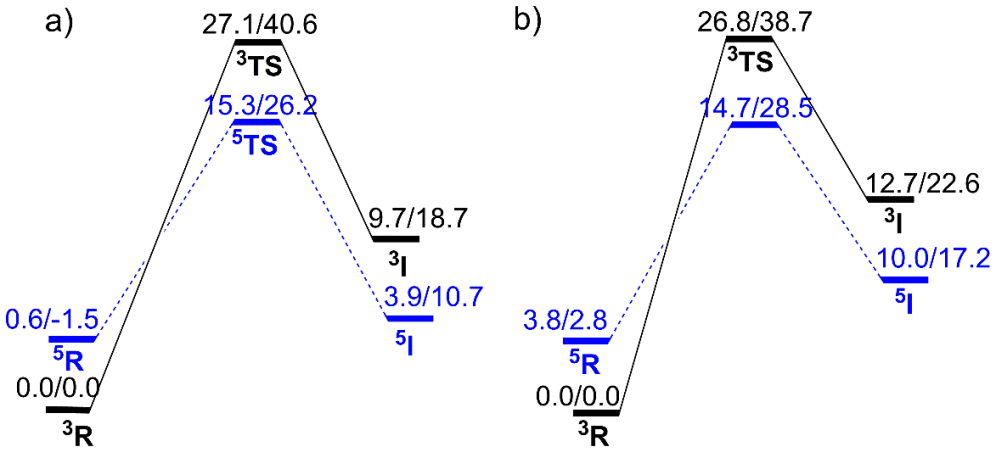

Figure 3.5: The potential energy surface for the C-H activation catalysed by Fe(IV)OTMC complex framed with a) N_4 b) N_2S_2. The black and blue line represents the S=1 and S=2 state pathways, respectively. The energy values are given as $\Delta E(B2+ZPE)/\Delta G_{273K}(B2)$. The PES's are plotted with respect to the energy of ^{3}R + DHA.

The figure shows that the activation energy in the case of N_2S_2 is slightly lower than the N_4 (by 0.6 kcal mol^{-1}) but in free energy, N_4 is found lower by 0.8 kcal mol^{-1}. The corresponding values of S_4 as given in Figure 3.3e (activation energy/activation free energy 15.6/25.9) are also found similar to the N_4 and N_2S_2. So, increment of reactivity is not so prominent here and is found almost unaffected by S-substitution.

3.3.6 Reactivity Analysis

At first, we were interested to examine if there is any type of steric interaction present in the oxidants which could restrict the abstractor oxygen to accept the hydrogen atom from the substrates. This may be reflected in the space-filling models of the optimised structures based on van der Waals radii. A qualitative inspection of the Fig. 3.6 indicated that the 'O' is more exposed in S-substituted complexes than the N_4. Although, it is not adequate to generalise the complete trend of reactivity from this analysis.

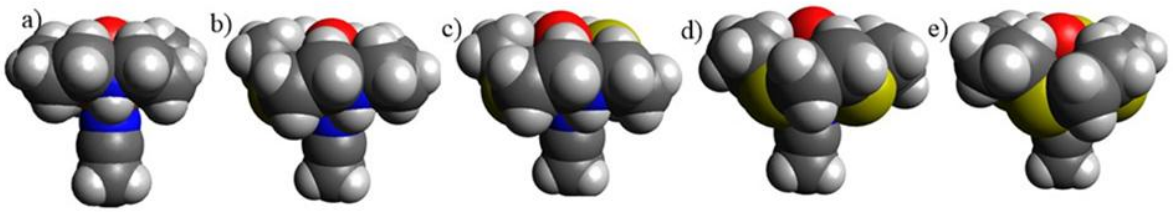

Figure 3.6: Van der Waal's images for reactants with different ligand frameworks a) N_4 b) N_3S_1 c) N_2S_2 d) N_1S_3 e) S_4.

3.3.7 Discussion about the Oxidants

The geometries of the quintet oxidants have been presented in the following Fig. 3.7.

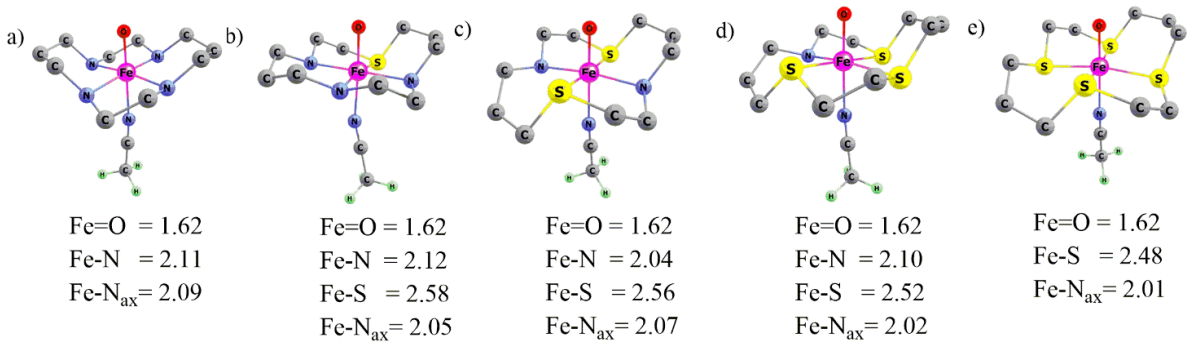

Figure 3.7: The S=2 optimised geometries of the oxidants with geometrical parameters wherein distances are in Å, angles are in degrees a) N_4, b) N_3S_1, c) N_2S_2 and d) N_1S_3 and e) S_4 framework. Hydrogen atoms were omitted to maintain the clarity.

By sequential equatorial replacement of the nitrogen by sulfur does not alter the Fe=O distances which are 1.62 Å for all five complexes. It is also evident from the experiment that on introducing two S atoms in the N_4 framework (Scheme 3.1(b)) the Fe=O distances decrease

only by 0.002 Å.[45] The axial Fe-N distance shows a decreasing trend i.e., 2.09 > 2.05 ~ 2.07> 2.02 ~2.01from N_4 to S_4 complexes.

3.3.8 Distortion Energy

As the reactions possess two state reactivity our focus is concentrated on S=2 transition states.

In the quintet transition states as available in the Fig. 3.8 the key geometrical parameters e.g., Fe=O distances are (1.72 Å) unique whereas slight alteration has been found for Fe-N_{ax} distances (2.25, 2.21, 2.22, 2.14, and 2.21 Å from N_4 to S_4 respectively).

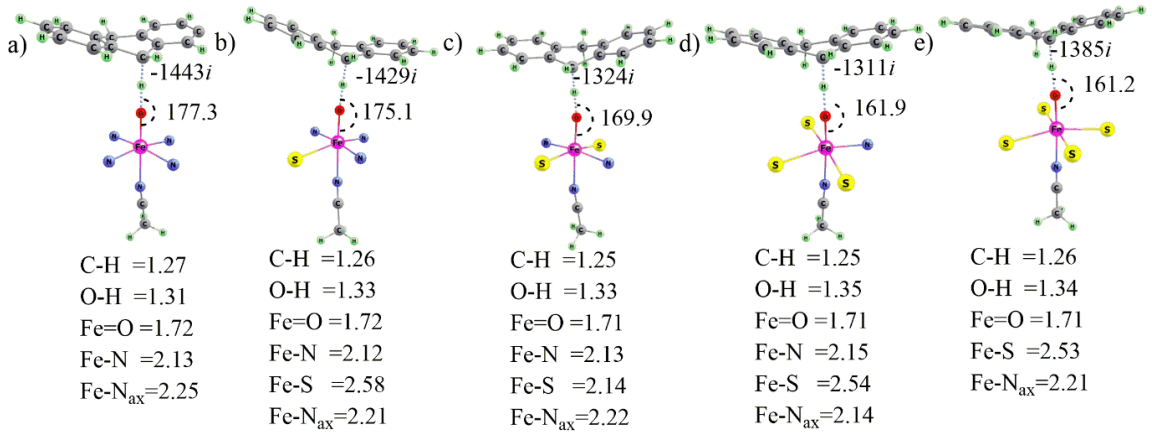

Figure 3.8: The S=2 optimised transition states with geometrical parameters wherein distances are in Å, angles are in degrees and imaginary frequencies (in *i* cm^{-1}) for H abstraction for quintet TS for a) N_4, b) N_3S_1, c) N_2S_2 and d) S_4 framework. Methylene groups were omitted to maintain the clarity.

The lowest $\Delta E^{\ddagger}_{dis}$ has been found for S_4 (9.3 kcal mol^{-1}) whereas the highest for N_4 (15.4 kcal mol^{-1}) for N_3S_1 and N_1S_3 it is almost the same (13.5 and 13.2 kcal mol^{-1}) and for N_2S_2 it is slightly higher (14.5 kcal mol^{-1}) and exists intervening between N_4 and S_4. The breaking C-H and forming O-H bond distances also do not change significantly by the S substitution. The angle between Fe-O-H shows a reducing trend from N_4 to S_4 (177.3°, 175.1°, 169.9°,161.9°, and 161.2°). These parameters may direct us towards the prediction of the distortion energy ($\Delta E^{\ddagger}_{dis}$) in the transition state. A plot of distortion energy with respect to the activation energy is plotted and presented in the Fig. 3.9. The reactivity between N_4 and S_4 is clearly understood although the complete trend is not so feasible. So, the required distortion energy could only partially explain the afforested reactivity trend.

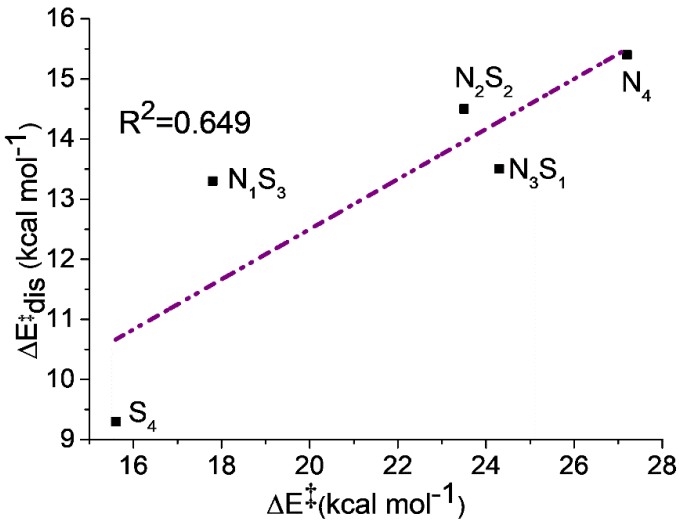

Figure 3.9: A plot of activation energy ($\Delta E^{\ddagger}$) versus distortion energy ($\Delta E^{\ddagger}_{dis}$) for the S=2 pathways.

3.3.9 Spin Density

The spin density upon the oxygen of Fe(IV)=O has shown a continuous increment from N_4 (0.220) to S_4 (0.290) which establishes that the more radical character in S_4 corresponds to a more prominent abstraction.[16] A plot of energy of activation vs. the spin density on oxygen plotted in Fig. 3.10 shows a good correlation except for the outlier N_2S_2.

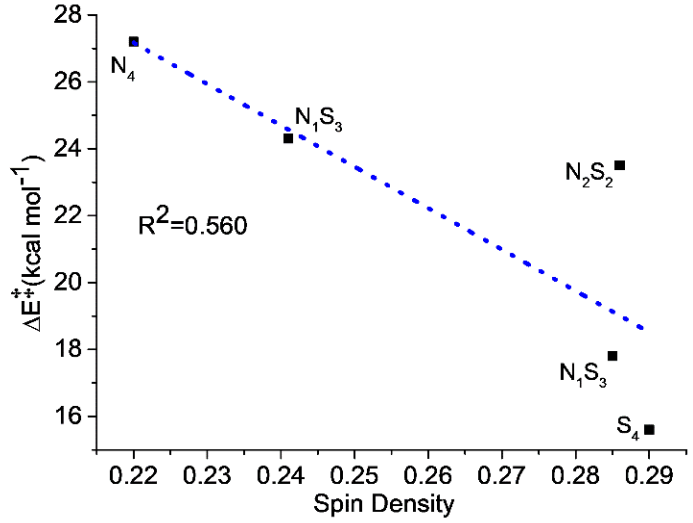

Figure 3.10: A plot of activation energy ($\Delta E^{\ddagger}$) versus spin density at the S=2 transition states.

So, we can claim that the radical character of the oxygen in Fe=O may also be responsible for the qualitative reactivity control like distortion energy.

3.3.10 The Energy of Electron Acceptor Orbital

To further excavate insight into the reactivity the energies of the electron acceptor orbitals in the oxidants have also been computed. As reactions proceed through the quintet state, the lowest unoccupied molecular orbital (LUMO) i.e., $\sigma^*_{Z^2}$ orbital play the role of acceptor orbitals The image of the LUMO's and their energies has been presented in Fig. 3.11.

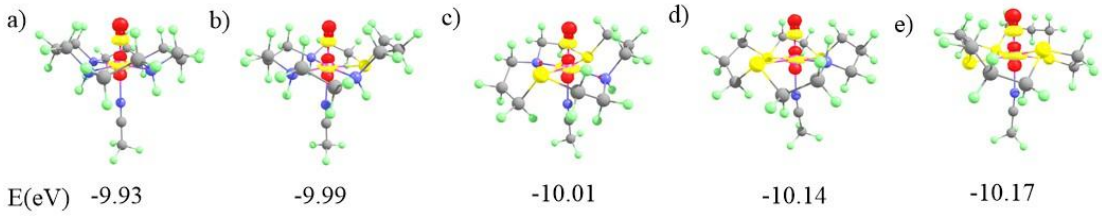

Figure 3.11: LUMO's of quintet reactants along with their energies in eV where a) N_4 , b) N_3S_1, c) N_2S_2 ,d) N_1S_3 and e) is S_4 framework.

We have also looked for the changes in the energy of activation with the energy of the acceptor orbitals providing an adequate connection between them as presented in Fig. 3.12. The energies of the LUMO show a consequent reduction on the sequential replacement of the N by S. This may be due to the influence of the thio-ligated equatorial ligand framework which decreases the distance of Fe-N_{ax} from N_4 to S_4.

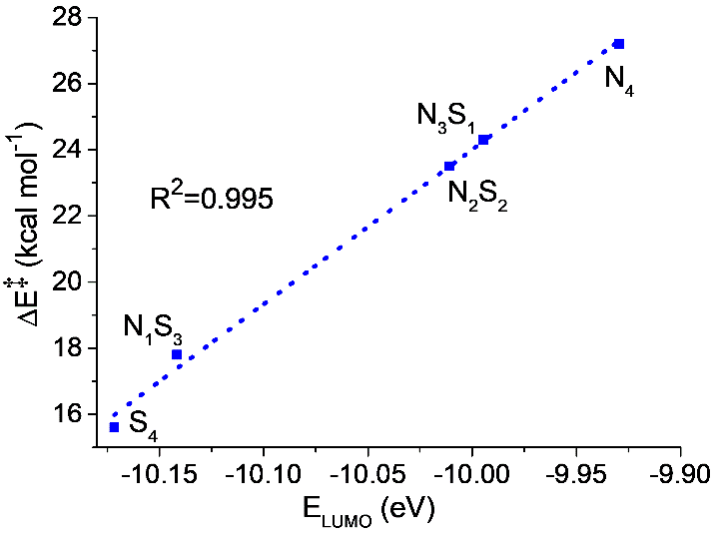

Figure 3.12: A plot of $\Delta E^{\ddagger}$ versus the energy of the LUMO (E_{LUMO}) of the oxidants at S=2 state.

Consequently, the bonding Fe=O ($\sigma^*_{z^2}$) destabilises, thereby stabilizing the anti-bonding acceptor orbital. As HAT is a single electron transfer process, the lower the energy of the acceptor orbital in oxidant implies the more efficient abstractor. The figure also shows an excellent linear correlation between the energy of activation and the energy of the acceptor

orbital as the value of R^2 is almost unity. So, we can safely claim here that due to successive falls of E_{LUMO} from N_4 to S_4, the HAT observed reactivity pattern comes to play.

3.3.11 Triplet-quintet Energy Difference

The difference in energy between the ground triplet and excited quintet state oxidants determines the spin inversion probability which is essential as the reaction follows TSR. The $\Delta E_{T\text{-}Q}$ values from N_4 to S_4 (12.4, 9.1, 10.0, 7.8, and 1.5 kcal mol^{-1}) show an almost consistent reduction of the energy gap with S-ligation. A plot between the energy of activation changes with spin state energy difference is presented in Fig. 3.13.

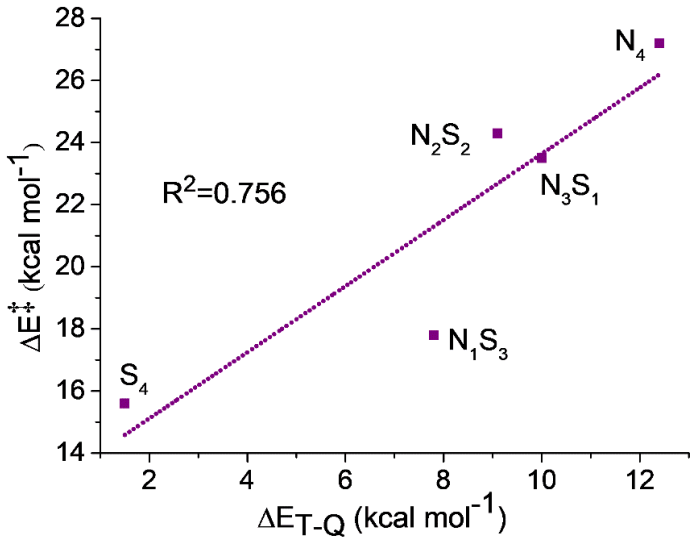

Figure 3.13: A plot of activation energy ($\Delta E^{\ddagger}$) vs. the triplet-quintet energy difference ($\Delta E_{T\text{-}Q}$)

The figure shows good correlations which explain the reactivity order as well as verified the presence of TSR. From the aforementioned discussion, it is clear that all the factors favour the increment of reactivity towards S-rich complexes and explain the overall insights into the reactivity.

3.4 Conclusions

Most of the bio-inspired Fe(IV)O complexes synthesised to the date involve nitrogen as a donor atom of the macrocyclic ligand attached either in an equatorial or axial manner to the metal atom. Indeed, it is important to find out the role of other donor atoms e.g., S, O etc. Herein we have demonstrated a DFT-B3LYP investigation to generalise the influence of equatorial Sulfur substitution on the reactivity pattern of C-H activation. A Fe(IV)=O complex with macrocyclic cyclam ligand has been chosen for this purpose along with DHA as the substrate. We have taken into account the complexes obtained by the sequential replacement of N by S i.e., N_4, N_3S_1, N_2S_2, N_1S_3 and S_4 framework. The significant outcomes of our investigations can be described as follows:

In this hydrogen atom transfer, C-H bond activation mechanism both the electron and proton travelled simultaneously where H linked with O and electron shifted to metal –d orbital.

The expected two state reactivity driven by the exchange enhanced interaction by the presence of unpaired electrons in the C-H activation catalysed by Fe(IV)O complexes is followed here. A spin crossover is perceived from ground S=1 to excited S=2 state during the progress of the reaction. Finally, the most interesting findings are the trend of reactivity which showed an increase in an orderly manner with increased substitution of the N atoms by the S atom. The reasons behind this increment of reactivity have been justified using the activation strain model analysis, the radical character of the abstractor which is here directly associated with the spin density upon 'O" of Fe=O and the energy of the electron acceptor orbital (E_{LUMO}). It has been found that in the case of sulfur reached macrocyclic ligand complexes, quite less energy is required to achieve the transition state geometry. The spin density on oxygen at the transition state increases continuously from N_4 to S_4 which facilitates the electron transfer as well as the overall reactivity. The spin state energy gap between S=1 and S=2 state oxidants consistently fall with S-ligation which implies a higher spin inversion probability as well as reactivity through TSR in S-rich complexes. The most powerful proof has been the consequent diminution of acceptor orbital energy with S substitution which facilitates the HAT i.e., electron transfer from the substrate to oxidant. Our computational data has also been able to replicate the available experimental outcomes as it shows a clear agreement in explaining the fact that N_2S_2 (1-trans) is more reactive than N_4 (2-trans). This investigation articulates predictions, which if validated, will encourage the design, synthesis and investigations of more and more bio-inspired mimics having Sulfur rich-macrocycle ligated compounds to develop the optimum catalyst for C-H bond activation.

References

1. K. Rydel-Ciszek, *React. Kinet. Mech. Catal*., **2021**, 133, 579–600.
2. H. Schwarz, S. Shaik, *Acc. Chem. Res.*, **2000**, 33, 139–145.
3. A. N. Biswas, M. Puri, K. K. Meier, W. N. Oloo, G. T. Rohde, E. L. Bominaar, E. Münck,L. Que., *J. Am. Chem. Soc.* **2015**, 137, 2428–2431.
4. E. Masferrer-Rius, M. Borrell, M. Lutz, M. Costas, R. J. M. Klein Gebbink, A*dv. Synth. Catal*., **2021**, 363, 3783–3795.
5. W. Nam, Y. M. Lee, S. Fukuzumi, *Acc. Chem. Res*. **2014**, 47, 1146–1154.
6. C. Arunkumar, Y. M. Lee, J. Y. Lee, S. Fukuzumi, W. Nam, *Chem. - A Eur. J.*, **2009**, 15, 11482–11489.
7. Y. Wang, K. Han, *J. Biol. Inorg. Chem.*, **2010**, 15, 351–359.

8. A. Ali, W. Akram, H. Y. Liu, *Molecules*, **2019**, 24, 2770.
9. A. R. McDonald, L. Que, *Coord. Chem. Rev.*, **2013**, 257, 414–428.
10. S. Shaik, *Nat. Publ. Gr.*, **2010**, 2, 347–349.
11. X. Shan, L. Que, *J. Inorg. Biochem.*, **2006**, 100, 421–433.
12. E. Andris, K. Segers, J. Mehara, L. Rulíšek, J. Roithová, *Angew. Chemie*, **2020**, 132 ,23337–23344.
13. C. Empel, S. Jana, R. M. Koenigs, *Molecules*, **2020**, 25, 900.
14. J. Serrano-Plana, A. Aguinaco, R. Belda, E. García-España, M. G. Basallote, A. Company, M. Costas, *Angew. Chemie*, **2016**, 128, 6418–6422.
15. E. B. Bauer, *Isr. J. Chem.* **2017**, 57, 1131–1150.
16. J. England, J. Prakash, M. A. Cranswick, D. Mandal, Y. Guo, E. Münck, S. Shaik, L. Que, *Inorg. Chem*., **2015**, 54, 7828–7839.
17. S. T. Kleespies, W. N. Oloo, A. Mukherjee, L. Que, *Inorg. Chem.,* **2015**, 54, 5053–5064.
18. K. Ray, J. England, A. T. Fiedler, M. Martinho, E. Münck, L. Que, *Angew. Chemie - Int. Ed.*, **2008**, 47, 8068–8071.
19. J. U. Rohde, J. H. In, M. H. Lim, W. W. Brennessel, M. R. Bukowski, A. Stubna, E. Münck, W. Nam, L. Que, *Science*, **2003**, 299, 1037–1039.
20. E. Kent Barefield, *Coord. Chem. Rev*., **2010**, 254, 1607–1627.
21. J. Cho, R. Sarangi, W. Nam, *Acc. Chem. Res*. **2012**, 45, 1321–1330.
22. J. England, J. O. Bigelow, K. M. Van Heuvelen, E. R. Farquhar, M. Martinho, K. K. Meier, J. R. Frisch, E. Münck, L. Que, *Chem. Sci*., **2014**, 5, 1204–1215.
23. S. Hong, H. So, H. Yoon, K. Bin Cho, Y. M. Lee, S. Fukuzumi, W. Nam, *Dalt. Trans*., **2013**, 42, 7842–7845.
24. A. Takahashi, D. Yamaki, K. Ikemura, T. Kurahashi, T. Ogura, M. Hada, H. Fujii, *Inorg. Chem.*, **2012**, 51, 7296–7305.
25. S. Taktak, M. Flook, B. M. Foxman, L. Que, E. V. Rybak-Akimova, *Chem. Commun*., **2005**, 42, 5301–5303.
26. T. A. Jackson, J. U. Rohde, S. S. Mi, C. V. Sastri, R. DeHont, A. Stubna, T. Ohta, T. Kitagawa, E. Münck, W. Nam, L. Que, J. *Am. Chem. Soc.*, **2008**, 130, 12394–12407.
27. H. Hirao, L. Que, W. Nam, S. Shaik, *Chem. - A Eur. J.*, **2008**, 14, 1740–1756.
28. S. P. De Visser, J. U. Rohde, Y. M. Lee, J. Cho, W. Nam, *J. Am. Chem. Soc.,* **2013**, 135, 5762–5767.
29. H. Park, D. Lee, *Chem. - A Eur. J.*, **2020**, 26, 5916–5926.
30. R. Kumar, B. Pandey, A. Sen, M. Ansari, S. Sharma, G. Rajaraman, *Coord. Chem. Rev.* , **2020**, 410, 213218.
31. C. V. Sastri, J. Lee, K. Oh, J. L. Yoon, J. Lee, T. A. Jackson, K. Ray, H. Hirao, W. Shin, J. A. Halfen, J. Kim, L. Que, S. Shaik, W. Nam, *Proc. Natl. Acad. Sci.*, **2007**, *104*, 19181–19186.

32. D. Mandal, R. Ramanan, D. Usharani, D. Janardanan, B. Wang, S. Shaik, J. *Am. Chem. Soc.*, **2015**, *137*, 722–733.

33. S. P. De Visser, R. Latifi, L. Tahsini, W. Nam, *Chem. - An Asian J.*, **2011**, *6*, 493–504.

34. C. A. Joseph, M. J. Maroney, *Chem. Commun.***, 2007**, 32, 3338–3349.

35. A. R. Stampfli, W. Blankenfeldt, F. P. Seebeck, *Curr. Opin. Struct. Biol.* **2020**, *65*, 1–8.

36. M. T. Green, J. H. Dawson, H. B. Gray, *Science*, **2004**, *304*, 1653–1656.

37. K. L. Stone, R. K. Behan, M. T. Green, *Proc. Natl. Acad. Sci.*, **2005**, *102*, 16563–16565.

38. Y. Shi, Z. Jiang, X. Hu, X. Hu, R. Gu, B. Jiang, L. Zuo, X. Li, H. Sun, C. Zhang, L. Wang, L. Wu, B. Hong, *Angew. Chemie - Int. Ed.*,**2021**, *60*, 15399–15404.

39. L. Müller, S. Hoof, M. Keck, C. Herwig, C. Limberg, *Chem. - A Eur. J.*, **2020**, *26*, 11851–11861.

40. M. Sallmann, S. Kumar, P. Chernev, J. Nehrkorn, A. Schnegg, D. Kumar, H. Dau, C. Limberg, S. P. De Visser, *Chem. - A Eur. J.*, **2015**, *21*, 7470–7479.

41. S. P. De Visser, M. G. Quesne, B. Martin, P. Comba, U. Ryde, *Chem. Commun.*, **2014**, *50*, 262–282.

42. D. Kumar, G. N. Sastry, D. P. Goldberg, S. P. De Visser, *J. Phys. Chem. A***, 2012**, *116*, 582–591.

43. D. Kumar, W. Thiel, S. P. De Visser, *J. Am. Chem. Soc.*, **2011**, *133*, 3869–3882.

44. J. Annaraj, S. Kim, M. S. Seo, Y. M. Lee, Y. Kim, S. J. Kim, Y. S. Choi, H. G. Jang, W. Nam, *Inorganica Chim. Acta*, **2009**, *362*, 1031–1034.

45. J. Deutscher, P. Gerschel, K. Warm, U. Kuhlmann, S. Mebs, M. Haumann, H. Dau, P. Hildebrandt, U. P. Apfel, K. Ray, *Chem. Commun.*, **2021**, *57*, 2947–2950.

46. D. Schröder, S. Shaik, H. Schwarz, *Acc. Chem. Res.*, **2000**, *33*, 139–145.

47. F. M. Bickelhaupt, K. N. Houk, *Angew. Chemie - Int. Ed.*, **2017**, *56*, 10070–10086.

48. A. D. Becke, *J. Chem. Phys*. **1993**, *98*, 1372–1377.

49. A. K. Pal and A. Datta, *J. Chem. Phys*., **2024**, 160, 164720.

50. A. Altun, J. Breidung, F. Neese, W. Thiel, J. *Chem. Theory Comput*., **2014**, *10*, 3807–3820.

51. Y. Yang, M. N. Weaver, K. M. Merz, *J. Phys. Chem. A*, **2009**, *113*, 9843–9851.

52. P. J. Hay, W. R. Wadt, *J. Chem. Phys.*, **1985**, *82*, 299–310.

53. B. D. Dunietz, M. D. Beachy, Y. Cao, D. A. Whittington, S. J. Lippard, R. A. Friesner, *J. Am. Chem. Soc.*, **2000**, *122*, 2828–2839.

54. A. V. Marenich, R. M. Olson, C. P. Kelly, C. J. Cramer, D. G. Truhlar, *J. Chem. Theory Comput.*, **2007**, *3*, 2011–2033.

55. A. V. Marenich, C. J. Cramer, D. G. Truhlar, *J. Phys. Chem. B*, **2009**, *113*, 6378–6396.

56. D. Janardanan, D. Usharani, H. Chen, S. Shaik, *J. Phys. Chem. Lett.*, **2011**, *2*, 2610–2617.

57. D. Mandal, S. Shaik, *J. Am. Chem. Soc.*, **2016**, *138*, 2094–2097.

58. D. Mandal, D. Mallick, S. Shaik, *Acc. Chem. Res.*, **2018**, *51*, 107–117.

59. S. Maeda, Y. Harabuchi, Y. Ono, T. Taketsugu, K. Morokuma, **2015**, *115* 258–269.
60. M. J. Frisch, *Gaussian 16, Revision B.01*, Gaussian, Inc., Wallingford CT, **2016**.
61. G. A. Andrienko, *Chemcraft Molecular Visualization Program*, version 1.8 (build 445).
62. A. Sirjoosingh, S. Hammes-Schiffer, *J. Phys. Chem. A*, **2011**, *115*, 2367–2377.
63. J. M. Mayer, *Acc. Chem. Res.*, **2011**, *44*, 36–46.
64. D. Usharani, D. Janardanan, C. Li, S. Shaik, *Acc. Chem. Res.*, **2013**, *46*, 471–482.
65. C. Geng, S. Ye, F. Neese, *Angew. Chemie - Int. Ed.*, **2010**, *49*, 5717–5720.
66. S. P. De Visser, J. *Am. Chem. Soc.*, **2006**, *128*, 15809–15818.
67. D. Janardanan, Y. Wang, P. Schyman, L. Que, S. Shaik, *Angew. Chemie*, **2010**, *122*, 3414–3417.
68. S. Ye, C. Y. Geng, S. Shaik, F. Neese, *Phys. Chem. Chem. Phys.*, **2013**, *15*, 8017–8030.
69. S. A. Wilson, J. Chen, S. Hong, Y. M. Lee, M. Clémancey, R. Garcia-Serres, T. Nomura, T. Ogura, J. M. Latour, B. Hedman, K. O. Hodgson, W. Nam, E. I. Solomon, *J. Am. Chem. Soc.*, **2012**, *134*, 11791–11806.
70. S. Shaik, H. Chen, D. Janardanan, *Nat. Chem.*, **2011**, *3*, 19–27.

Chapter 4

A Density Functional Theory Analysis of the C-H Activation Reactivity of Iron(IV)-Oxo Complexes with 'O' Substituted Tetramethyl-cyclam Macrocycle

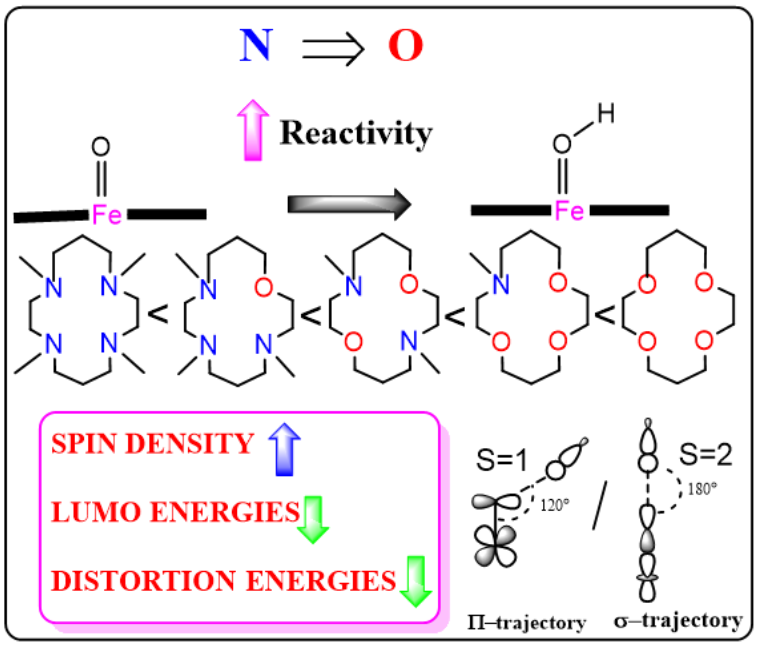

4.1 Introduction

Metal-oxo species of transition metal series are vastly studied, the earlier members more prominently than the later ones owing to the oxo wall and the high-valent Fe(IV)O intermediates being studied in depth widely.[1-12] These complexes have been successfully presented in many articles wherein they act as the active oxidants in the catalytic cycles of mononuclear non-heme and heme enzymes.[13-15] Multiple studies have also been conducted towards understanding the structural and electronic parameters of these metal-oxo complexes to get an idea how they can drive us towards a better reactivity by accessing the mechanisms involved. For example, several octahedral/trigonal bipyramidal geometries have been explored wherein both S =1 (triplet) or S=2 (quintet) ground spin states have been taken into account.[16,17] It has been proven as such that spin states of Fe(IV) ions is an important governing factor affecting the catalytic activity of Fe(IV)O complexes. Studies reveal many changes have also been projected in the coordination sphere directly in the form of axial as well as equatorial ligands in the last decade, whilst other changes on secondary level by manipulating the ligand architecture have also been proven to have significant effect on the mechanistic pathways.[18,19]

Other factors such as the oxidative capabilities among different redox states have also gained attention with larger oxidation state enhancing the reactivity owing to the electrophilicity and reduction potentials.[20,21] Multiple DFT and experimental studies have been made to explore and enhance the C-H activation processes carried out by such complexes, in which the reactivity process is significantly influenced by the thermodynamics of bond formation (O-H) and breakage (C-H). These reactions proceed mostly with simultaneous transfer of electron and proton (HAT or cPCET mechanisms) that have been studied from time to time.[22-24] Here we see how electron and proton when transferred together as a true H atom are referred as Hydrogen Atom Transfer but when travelling differently are called Proton Coupled Electron Transfer. However, it has also been established that in contrast to these mechanisms, proton and electron transfer can take place stepwise [25-26] wherein the transfer involves two steps. These involve PT followed by ET (basic mechanism) or ET followed by PT(oxidative mechanism) as summed in the Scheme 4.1 herein. There might even be asychronicity involved with the TS consisting of either more electron or proton transfer.

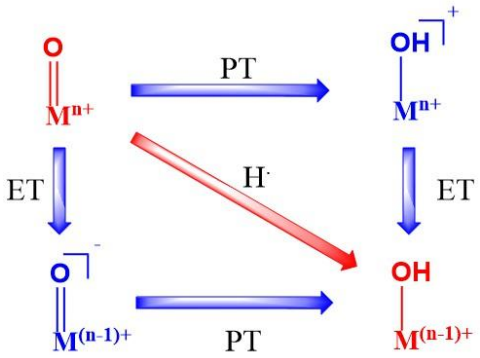

Scheme 4.1: Various types of mechanisms possible for H transfer.

PT signifies proton transfer whereas ET is for Electron transfer. Also, the red arrow shows synchronous behaviour and purple the asynchronous. Such mechanisms have a significant role in some cases wherein the otherwise lower oxidation potential is balanced by factors as the basicity of the metal oxo complexes (via PT followed by ET).[27-30]

The developments in this field have given considerable momentum in both understanding and the application of the Fe(IV)O chemistry for homogeneous catalytic oxidations. Now, let's take into contemplation the well-known fact that the biological Fe=O oxidants in the (IV) oxidation state of the iron atom usually consists O-based ligands (week field in nature) for e.g., carboxylate, water located cis to the oxo donor (Scheme 4.2(a)).[31,32]

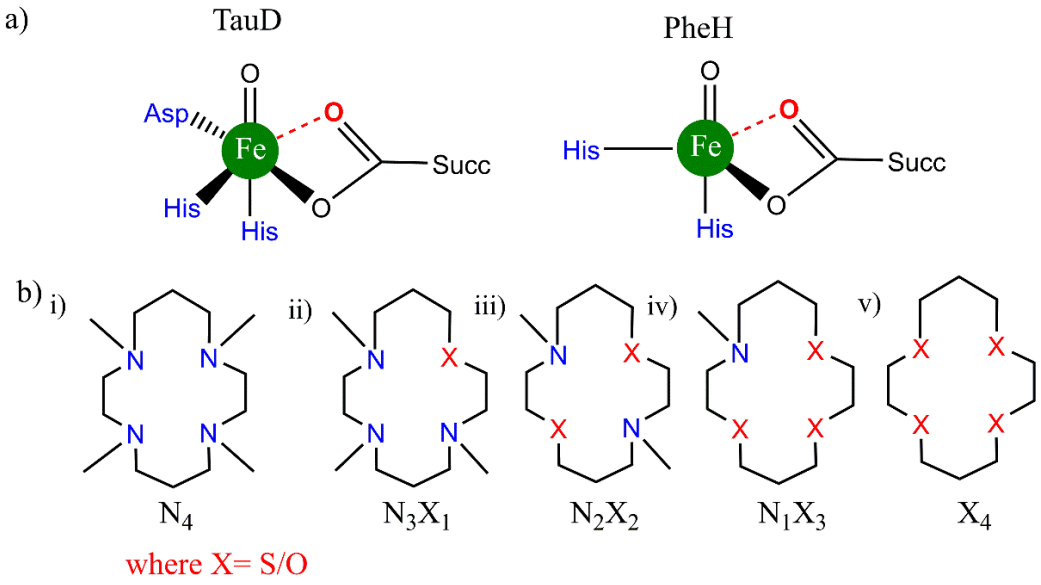

Scheme 4.2: Structures of a) biological enzymes Taurine: αKG dioxygenase and phenylalanine hydroxylase b) bioinspired TMC complexes with equatorial substitution.

In our previous work in this field of hetero-substitution, inspired by the study of Ray and co-workers, we highlighted how alterations made in the primary coordination sphere of TMC like complexes in a sequential order (using S) of equatorial ligands imparted us better reactivity trends for the C-H activation process.[33] We successfully established that hetero-substitution led to lower reaction barriers and hence opened the door to the use of alternate atoms in the vastly studied ferryl processes.[34] In a combined experimental and computational study performed by Prez et al., substitution of the N-CH_3 donor in the TMC and TMCN macrocycles was studied to depict how this O substitution led to better reactivity patterns. The details of the structures have been presented in Scheme 4.3.

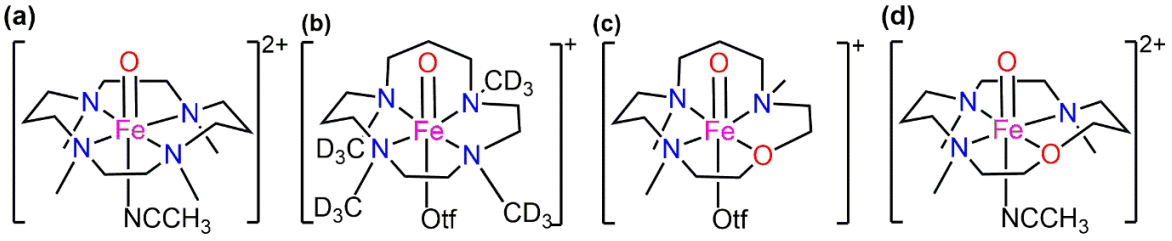

Scheme 4.3: a) TMC with CH_3CN as axial ligand b) TMCN with -OSO_2CF_3 as axial ligand c) TMCO with -OSO_2CF_3 as axial ligand d) TMCO complexes in similar conformation and axial ligand with TMC.

Other than the N/O donor atom, there is also a significant difference in structure between traditional TMC (Scheme 4.3a) and TMCO (Scheme 4.3(c)). The propylene and ethylene linkers are in adjacent positions in TMCO, however they are in alternate positions in TMC.[35]

The axial ligands were also different. In TMCN, CD_3 substituents on the donor N atoms are attached equatorially in place of CH_3. (Scheme 4.3(b)). This encouraged us to investigate the effects on C-H activation reactivity after substituting oxygen for the equatorial donor atom nitrogen. For this purpose, anti-geometrical isomers (anti-position of methyl groups w.r.t the Fe=O unit) of the base molecule with the same axial ligand have been used. The mostly investigated, TMC (Scheme 4.3(a)) macrocycle has been selected as the base compound that makes the TMCO complex as presented in Scheme 4.3(d). The primary goal here is to determine whether oxygen-substituted iron-oxo TMC complexes may offer us a better C-H activation catalyst and whether these improvements will happen in a sequential manner. The dihydroanthracene (DHA) is used as a C-H bond source and the reaction has been modelled in the presence of the solvent acetonitrile. Reactivity studies have been performed on both lower (S=1) and higher (S=2) spin states. The interplay of various other factors has also been taken into consideration which include- spin density on the abstractor atoms, frontier orbitals and deformation energies to obtain the transition states. Mulliken charges and spin have been carefully analysed guiding us to the correct identification of the electronic states. Effect of N, O-substituted macrocycles on quantum mechanical tunneling and H/D kinetic isotope effect studies have also analysed.[36]

4.2 Computational Details

DFT method has been used to carry out geometry optimizations for all the species wherein the popular B3LYP functional (Becke's three-parameter exchange with Lee-Yang, and Parr's correlation functional) has come to practice.[37-39] Several independent studies support this functional for C-H activation reaction catalysed by this type of complexes, hence it is a significant benchmark.[40,41] For the basis set we have taken i) LANL2DZ with ECP for Fe and Pople's double zeta 6-31G* for all the other atoms C, H, N, O, F and S marked as B1 for convenience.[42,43] the effect of acetonitrile solvent has been computed during optimization using the self-consistent reaction field i.e., SCRF and SMD model.[44,45] Further single-point calculations have also been done for energy refinement using ii) Def2tzvpp for all the atoms marked as B2 and iii) 6-311++G(2d,2p) for all atoms and ECP containing SDD for iron marked as B3. The same solvent model like B1 has been also implemented in B2 and B3. Triflate ($CF_3SO_3^-$) counterions are poised at the bottom parts of the axial ligands to make the system neutral. The usage of solvents with counterions usually diminish the secondary interactions by neutralising the charges.[46] Frequency calculations are very detrimental for validating the nature of the optimised structures wherein one imaginary frequency indicates the transition states

(TS), which have been performed at the B1 level of theory. The zero-point vibrational energy (ZPVE), as well as thermal and entropic corrections to the Gibbs free energy at T = 298K (25°C) have been evaluated for valid determination of the potential energy surface. Intrinsic reaction coordinate (IRC) calculations have also been carried out to further verify if the TS are connecting to the proper minima as required.[47] This entire DFT study has been performed using Gaussian 16[48] program packages and for the generation as well as visualisation of natural orbitals, Chemcraft software[49] has been used. For rate, isotope effect and quantum mechanical tunneling studies have been performed using KiSTheLP software.[50] The kinetics calculations have been performed using the following eqn.[51]

$$k = \kappa\sigma \frac{k_b T}{h} \exp\left(\frac{-\Delta G^{\ddagger}}{RT}\right) \quad (Eq.\ 1)$$

where κ and σ stand for the transmission coefficient and reaction symmetry, respectively. The transmission coefficient has been calculated using the 1D (one-dimensional) asymmetric Eckart method[52] which has been used in various H-transfer processes successfuly.[53-55] ZPE corrected energies of the reactant, transition states, and products in addition to the imaginary frequency are used in this method, which in turn build up the mass weighted intrinsic reaction coordinate (IRC).[56] The H/D kinetic isotope effect (KIE) values have been calculated from the respective rate constants from H and D variants as:

$$KIE = \frac{k_H}{k_D} \quad (Eq.\ 2)$$

For calculating the reduction of activation barrier, we have used the following equation where R is the universal gas constant, T is the absolute temperature

$$\Delta\Delta E^{\ddagger}_{tun} = -RT \ln \kappa(T) \quad (Eq.\ 3)$$

For calculating stability constant log β, the following equation have been used.[57]

$$\log \beta = (\log_{10} e) \frac{-\Delta G}{RT} = \frac{-\Delta G}{2.303RT} \quad (Eq.\ 4)$$

where R is the universal gas constant and T temperature. ΔG has been calculated for the reactions using the following equation.

$$\Delta G = G(ML) + 4 \times G(H_2O) - G\{M(H_2O)_4\} - G(L) \quad (Eq.\ 5)$$

Where ML represents the Fe(IV)O(TMC) complexes and L are the respective N_4, N_3O, N_2O_2, NO_3, O_4 tetradentate macrocyclic ligands.

Distortion energies for the transition state have been calculated using the following equation:

$$\Delta E^{\ddagger}_{dist} = (E^{\ddagger}_R + E^{\ddagger}_S) - (E_R - E_S) \quad (Eq.\ 6)$$

where $E^{\ddagger}_R$ and $E^{\ddagger}_S$ refer to the reactant and substrate counterparts in the T.S. structure.

4.3 Results

At first, we searched for the potential for production of each of the five Fe(IV)O complexes by figuring out their stability constants, which are represented by log β in the equation 4. Since the constant shows how the ligation of the individual TMC complexes (with varied donor atoms) to the Fe=O unit would affect the free energy of formation, higher values of the constant indicate more favourable complex formation. In all five complexes, stability constant values were determined to be approximately 28.2 as depicted in Table 4.1.

Table 4.1: Stability constants for all the complexes.

Complex	log β
N_4	28.19
N_3O	28.19
N_2O_2	28.17
NO_3	28.17
O_4	28.16

Kirby et. al., in a study of few U(VI) complexes showed comparable values of log β.[57] It is also observed in their case that the calculated values are overestimated with respect to the experimentally observed ones. Here, we are unable to adequately support the absolute values of log β because there is a dearth of literature about stability constants for Fe(IV)O. Aside from the absolute value, however, we can declare with confidence that the O-substituted TMC macrocycle can ligate with Fe(IV)O in a manner similar to that of the most popular N_4 TMC frameworks.

The optimised geometries of the quintet oxidants with important parameters have been presented in the following Fig. 4.1.

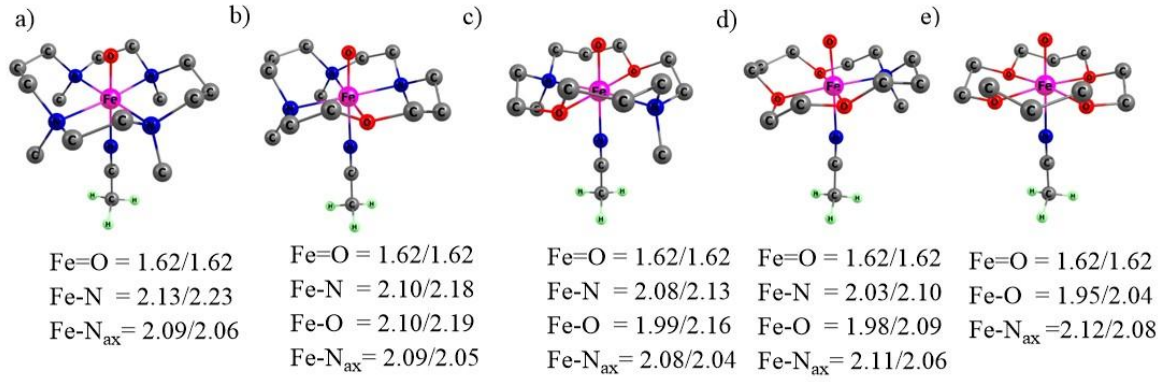

Figure 4.1: The optimised oxidants with geometrical parameters with S=1/S=2 wherein distances are in Å for quintet oxidants a) N_4 b) N_3O_1 c) N_2O_2 d) N_1O_3 and e) O_4. Hydrogen atoms are omitted to maintain the clarity.

While the average Fe-N/Fe-O distance (equatorially linked) decreased progressively, the Fe=O and Fe-N_{ax} bond lengths (axially connected) are almost the same in all complexes.

4.3.1 Spin State Reactivity

In general, the four unpaired electrons in Fe(IV) can be occupied in a variety of ways, resulting in two distinct spin states, S=1 and S=2. Thus, the hydrogen atom transfer mechanism can occur in either or both states[58] and the electron transfer pathways have already been presented in Figure 1.6. The panel a showed the low spin i.e., triplet state pathways where a β electron from the $\sigma_{C\text{-}H}$ bond moves to one of the π* orbital of Fe. This is referred as π pathway/trajectory since the transfer takes place to the π* orbital.[59] As depicted; the orientation of the substrate occurs at a Fe-O-H angle of ~120°. The panel b showed the high spin path i.e., quintet pathway where one α electron from the $\sigma_{C\text{-}H}$ bond of the DHA shifts to the σ^*_{z2} anti-bonding orbital of Fe. Here, as DHA approaches the oxidant through the upper side with a Fe-O-H angle ~180°, this pathway is named as σ pathway/trajectory. To confirm these trajectories sno plots are studied which confirm the proposed arrangement for S=2 have been presented in Fig. 4.2.

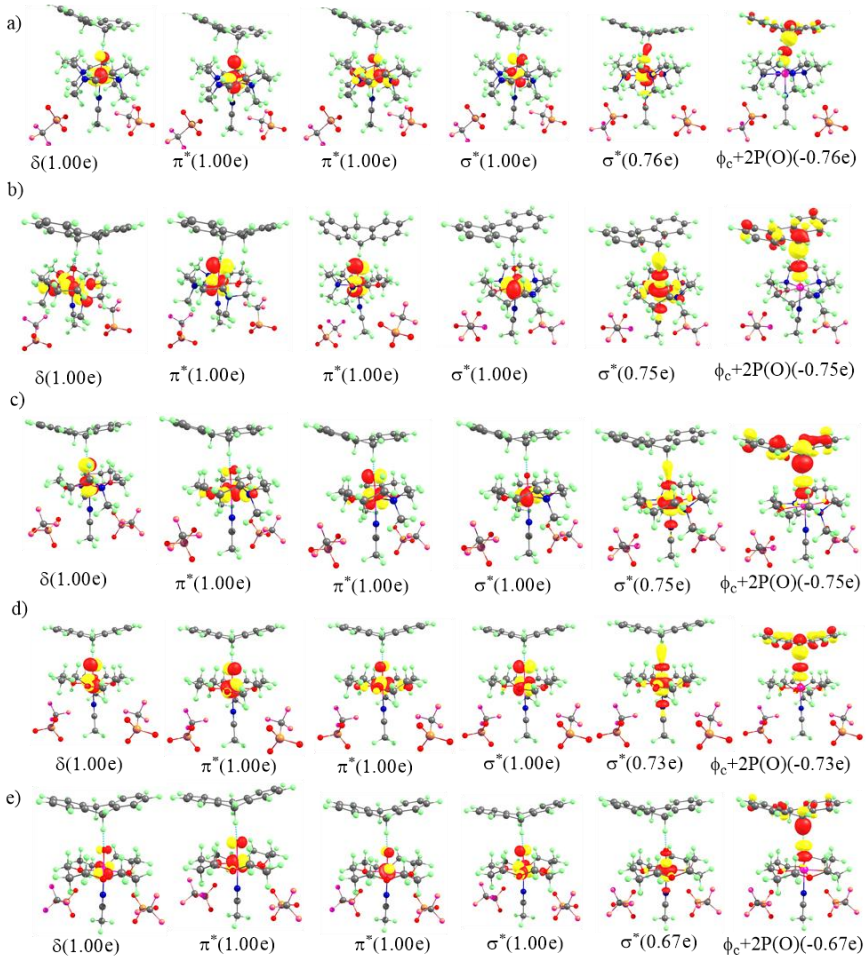

Figure 4.2: Spin Natural orbitals and their occupations in transition states for ^{5}TS of a) N_4 b) N_3O_1 c) N_2O_2 (d) NO_3 and e) O_4 framework.

4.3.2 Reactivity Pattern

Reactants in the quintet state typically have higher energy than reactants in the triplet state for Fe(IV)=O complexes; however, this is reversed in the transition state and product, leading to the Two-State-Reactivity (TSR) phenomenon. Fig. 4.3 depicts all the relevant potential energy surfaces for the rate determining step of the C-H activation process catalysed by all five complexes.

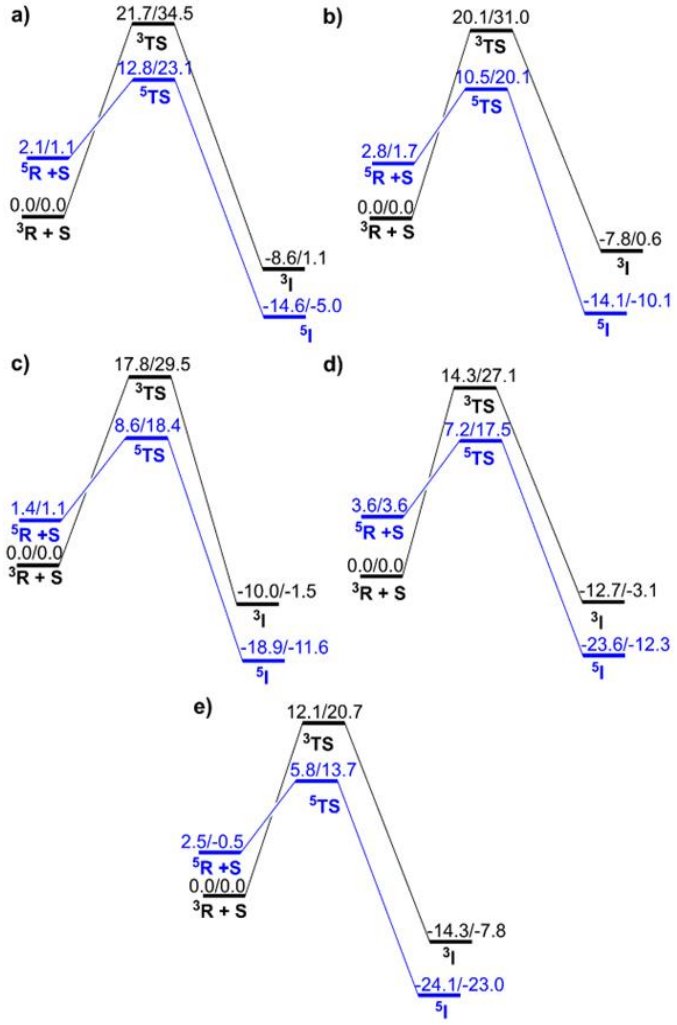

Figure 4.3: The potential energy surface for the C-H activation catalysed by Fe(IV)O complex with a) N_4 b) N_3O_1 c) N_2O_2 d) N_1O_3 and e) O_4 macrocyclic ligands. The black and blue line represents the S=1 and S=2 state pathways, respectively. The energy values are given as $\Delta E(B2+ZPE)/\Delta G_{298K}(B2)$. The PESs are plotted with respect to the energy of ^3R + DHA.

The S=1 is observed as ground state is in all oxidants, and the spin state energy gaps (ΔE_{Q-T}) are 2.1, 2.8, 1.4, 3.6, and 2.5 for N_4, N_3O_1, N_2O_2, N_1O_3, and O_4 respectively. As a manifestation of Exchange enhanced Reactivity[60] TSR is observed here.[61-64] In this instance an interesting reactivity pattern is observed. The C-H activation barrier catalysed by five different oxidants was shown to decrease in a sequential manner with the increasing amount of oxygen

substitution in the TMC macrocycle. Regardless of the choice of the basis set or thermodynamic parameters used, such as free energy or ZPE corrected energy, the reactivity pattern remains consistent. In B2 level of theory the barrier of activation values kept decreasing as 12.82 (23.14) (N_4) > 10.50 (20.06) (N_3O_1) > 8.59 (18.38) (N_2O_2) > 7.19 (17.52) (N_1O_3) > 5.79 (13.73) (O_4) wherein the values in the brackets indicate free energies. Even on comparing the values for triplet states of all the complexes respectively we observed the same trend of reactivity i.e., N_4< N_3O_1< N_2O_2< N_1O_3< O_4. Additional details are presented in Table 4.2.

Table 4.2. Relative energies (in kcal mol^{-1}) of oxidants, TS and intermediates computed at different levels of theory.

Reactions	Spin State	Species	B1 + ZPE	B2 +ZPE	G_{298K} (B2)	B3 + ZPE	G_{298K} (B3)
N4	S=1	^{3}R+S	0.0	0.0	0.0	0.0	0.0
		^{3}TS	25.9	21.7	34.5	20.2	33.2
		^{3}IH	1.2	-8.6	1.1	-6.2	3.0
	S=2	^{5}R+S	5.5	2.1	1.1	0.7	0.0
		^{5}TS	19.0	12.8	23.1	9.0	20.9
		^{5}IH	1.8	-14.6	-5.0	-9.0	0.1
N_3O	S=1	^{3}R+S	0.0	0.0	0.0	0.0	0.0
		^{3}TS	23.7	20.1	31.0	18.6	29.5
		^{3}IH	-1.0	-7.8	0.6	-20.8	-15.2
	S=2	^{5}R+S	5.0	2.8	1.7	1.2	0.2
		^{5}TS	16.6	10.5	20.1	6.2	15.8
		^{5}IH	-11.3	-14.1	-10.1	-10.4	-2.0
N_2O_2	S=1	^{3}R+S	0.0	0.0	0.0	0.4	0.6
		^{3}TS	21.1	17.8	29.5	16.3	28.5
		^{3}IH	-3.0	-10.0	-1.5	-12.2	-3.4
	S=2	^{5}R+S	3.6	1.4	1.1	0.0	0.0
		^{5}TS	14.4	8.6	18.4	4.6	14.8
		^{5}IH	-16.4	-18.9	-11.6	-25.5	-17.8
NO_3	S=1	^{3}R+S	0.0	0.0	0.0	2.8	4.3
		^{3}TS	17.1	14.3	27.1	12.4	25.3
		^{3}IH	-6.6	-12.7	-3.1	-15.5	-5.8
	S=2	^{5}R+S	6.4	3.6	3.6	0.0	0.0
		^{5}TS	13.0	7.2	17.5	2.8	13.2
		^{5}IH	-21.3	-23.6	-12.3	-30.9	-19.7
O_4	S=1	^{3}R+S	0.0	0.0	0.5	0.0	0.7
		^{3}TS	14.7	12.1	20.8	10.0	22.3
		^{3}IH	-8.2	-14.3	-7.8	-17.3	-9.3
	S=2	^{5}R+S	5.3	2.5	0.0	0.8	0.0
		^{5}TS	11.3	5.8	13.7	1.4	12.2
		^{5}IH	-24.3	-24.1	-23.0	-39.5	-34.4

Here B1 is 6-31G*/LANL2DZ(Fe) and B2 is Def2tzvpp and B3 is 6-311++G(2d,2p)/SDD(Fe). This fascinating reactivity trend led us to divulge into the contributing cause of this kind of fascinating pattern. As the spin state gaps are identical in all the complexes and the S = 1 is the ground state for reactants and then we observe a cross over to the S = 2 surface during TSR, this leads us to take into consideration factors other than triplet-quintet gap which are discussed in detail below.

4.3.3 LUMO Energies

The acceptor orbital's energy has a significant impact on the reactivity of electron transfer processes. In S=2 state of these oxidants, the electron acceptor orbital ($\sigma^*_z{}^2$) is the lowest unoccupied molecular orbital (LUMO), and its lower energy values make the electron transfer from the substrate easier. Therefore, the trend -3.56 (N_4) to -3.58 (N_3O_1) to -3.96 (N_2O_2) to -4.24 (N_1O_3) to -4.60 (O_4) shows that the process of accepting electrons from DHA became more convenient as we continued to replace N atoms with O. This is one of the prominent reasons for the increased reactivity with this hetero-substitution.[33,34] The lowering tendency in the LUMO's energy could have resulted from oxygen having a weaker field effect than nitrogen, which in turn stabilises the anti-bonding acceptor orbital. This can be explained on the basis of charge transfer. Fig. 4.4's depiction of the linear relationship between activation energy and LUMO energy provides insight into reactivity.

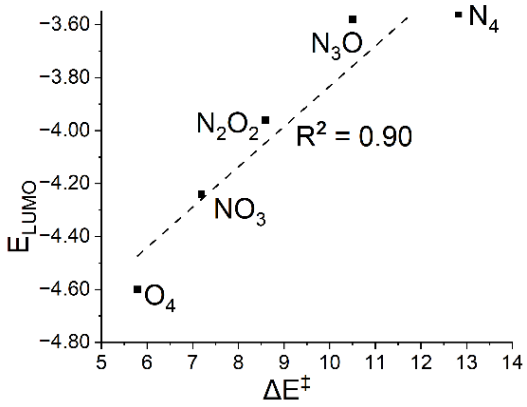

Figure 4.4: A plot of activation energy ($\Delta E^{\ddagger}$) versus the energy of the LUMO i.e., electron acceptor orbital (E_{LUMO}) of the oxidants at S=2 state.

We performed NBO and Mulliken population analysis to see how on moving from N_4 to O_4 the charge transferred from the ligands attached to the metal centre. As more and more charge was transferred trend at the Fe atoms being 0.55 (N_4) to 0.61 (N_3O_1) to 0.64 (N_2O_2) to 0.73 (N_1O_3) to 0.81 (O_4) it is safe to say the ligand field kept on weakening sequence wise resulting in more electrophilic metal centre and hence more reactivity.

4.3.4 Spin Density

The spin density on the abstractor i.e., on the oxygen of Fe=O has a key role to play in the reaction dynamics.[65]. On evaluating these values on the O atom of the ferryl group in the TS we observe sequential increase from 0.28 (N_4) to 0.30 (N_3O_1) to 0.33 (N_2O_2) to 0.35 (N_1O_3) to 0.40 (O_4). Plotted in this Fig. 4.5, we notice a sufficiently linear connection ($R^2 = 0.93$) between the spin density on abstractor and the energy of activation.

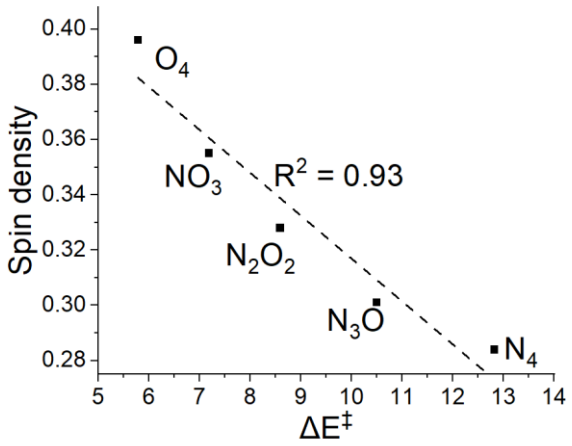

Figure 4.5: A plot of activation energy ($\Delta E^{‡}$) versus spin density at the 'O' of the Fe=O unit in the S=2 transition state.

4.3.5 Distortion Energies

To further validate our results, we then used equation 6 from the computational details section to determine the distortion energies ($\Delta E^{‡}_{dist}$) of the oxidants and substrate in order to reach the transition states. A plot of $\Delta E^{‡}_{dist}$ and the energy of activation have been presented in the Fig. 4.6.

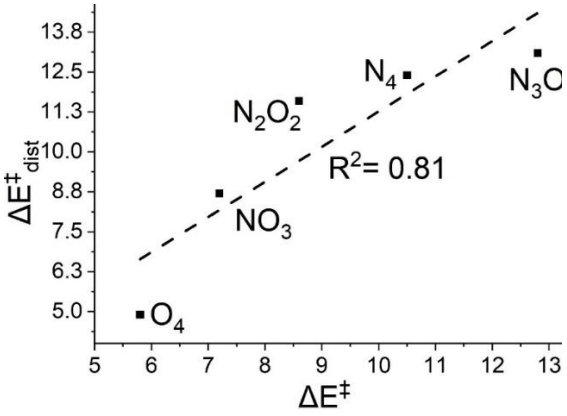

Figure 4.6: A plot of activation energy ($\Delta E^{‡}$, in kcal mol^{-1}) versus the distortion energies ($\Delta E^{‡}_{dis}$, in kcal mol^{-1}) of the oxidants at S=2 state.

Fig. 4.6 demonstrates a consistent decrease in $\Delta E^{\ddagger}_{dist}$, with the greatest value of 13.1 in N_4; other values include 12.4 for N_3O_1, 11.6 and 8.7 for N_2O_2 and N_1O_3, respectively, and the 4.9 for O_4. Lower distortion energies in the oxygen substituted complexes show how the distortion undergone is minimum in these cases and hence the formation of transition state more favourable. Our findings also show good consistency with earlier research in related complexes, which published theoretical calculations and experimentally validated investigations for TMC and TMCO complexes (Schemes 4.3a and 4.3c). The B3LYP/TDZP estimated free energy of activation for the cyclohexene substrate indicates that the TMCO complex was more favourable than the TMC-N_4 by 6.3 kcal mol^{-1}.[35] Here for DHA substrate we found similar value as 5.1 kcal mol^{-1} in B3 level of theory.

4.3.6 Quantum Chemical Tunneling

We were also curious to look for the impact of 'O' substitution on quantum mechanical tunneling. The data related to the tunneling calculation of H-abstraction reaction catalysed by all five complexes are collected in the Table 4.3.

Table 4.3: The value of rate constants for the H-abstraction reactions (k_H and k_D in cm^3 $molecule^{-1}$ sec^{-1}) transmission coefficients (κ_H and κ_D), kinetic isotope effect (KIE_{ECK}), barrier lowering quantity ($\Delta\Delta E^{\ddagger}_{tun}$), and the effective barrier (ΔE- $\Delta\Delta E^{\ddagger}_{tun}$).

COMPLEX	k_H	k_D	κ_H	κ_D	KIE_{ECK}	$\Delta\Delta E^{\ddagger}_{tun}$	ΔE- $\Delta\Delta E^{\ddagger}_{tun}$
N_4	$8.12x10^{-25}$	$6.48x10^{-26}$	6.61	2.96	12.5 (10)*	1.12	11.7
N_3O	$3.44x10^{-23}$	$4.38x10^{-24}$	3.04	2.03	7.9	0.66	9.8
N_2O_2	$2.20x10^{-22}$	$4.15x10^{-23}$	2.05	1.64	5.3	0.42	8.2
NO_3	$2.17x10^{-20}$	$6.55x10^{-21}$	1.19	1.64	3.3	0.10	7.1
O_4	$3.65x10^{-20}$	$1.82x10^{-20}$	1.03	1.02	2.0	0.01	5.8

* The values in the parenthesis are experimental value[66]

Standard TMC complexes (N4) have a tunneling corrected H/D kinetic isotope effect of 12.5, which is in good accord with an earlier empirically reported value of 10.[66] It's interesting to note that when 'O' is substituted on TMC, the transmission coefficient and KIE fall progressively. The values of the tunneling adjusted KIE are 12.5 (N_4), 7.9 (N_3O_1), 5.3 (N_2O_2), 3.3 (N_1O_3), and 2.0 (O_4) if we search for it in column 6 of Table 4.3.

It is revealed that the imaginary frequency of the transition states, which regulates the potential energy surface's curvature, is the cause of this pattern. Higher tunneling is insinuated by a

narrower curvature, which is implied by a higher imaginary frequency value.[40] Fig. 4.7 presents the transition state structures with significant geometrical features and imaginary frequencies.

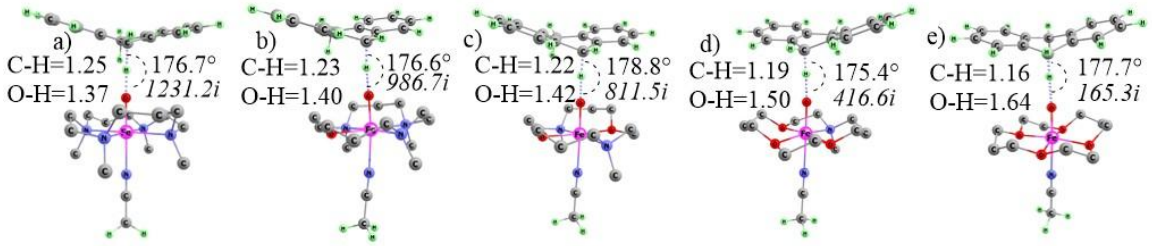

Figure 4.7: Quintet TS with their imaginary frequencies where a) N_4 b) N_3O_1 c) N_2O_2 d) N_1O_3 and e) O_4 macro cyclic ligands with C-H (breaking) and O-H (forming) bond lengths.

The imaginary frequency value for N_4 is 1231.2i, and it decreases steadily to 986.7i for N_3O_1, 811.5i for N_2O_2 and 416.6i for O_4 and 165.3i for N_1O_3. In context of the breaking C-H and forming O-H bond parameters in the transition state it is clear that the transition state for N_4 is most symmetric. The C-H bond keeps becoming shorter from N_4 to O_4, and oppositely, the O-H bond distances keep increasing, making TS's product-like in prior cases but reactant-like in the latter. So, the decreasing frequencies with the substitution taking place hints towards the role of quantum tunneling since it's a well-known fact that the mechanism of QM tunneling (quantum mechanical tunneling) relies on the path function and potential energy surfaces (PES) depend on the imaginary frequencies. The higher imaginary frequencies indicate a sharper PES, i.e., atom has to tunnel through a lesser distance making the phenomenon more favourable. The tunneling coefficients for H and D isotope counterpart with Eckart corrected values of KIE are reported herein. We have also calculated the tunneling corrected barrier. When switching from N_4 to O_4, the calculated natural charges on Fe in the S=2 oxidant are nearly equal with oxygen replacement, i.e., 0.95, 0.94, 0.93, 0.95, and 0.97. It follows that anti-electrophilicity has no influence on tunneling in this situation.[40] Although the reduction of the activation barrier by tunneling (column 7 in table 4.3) is higher in N_4 (due to the higher transmission coefficient), the overall effective barrier (column 8 in Table 4.3) is not able to alter the earlier reactivity pattern obtained from classical thermodynamics.

4.4 Conclusions

This computational study has been devoted to investigating the reactivity of the oxygen substituted iron(IV)-Oxo N_4 macrocycle in order to design a better catalyst for C-H activation. A well-known TMC compound, $[Fe(IV)=O(TMC\text{-}N_4)(CH_3CN)]^{2+}$, has been taken into consideration for base compounds. Additionally, the method of sequentially replacing the equatorial N atoms with O atoms results in the formation of four additional compounds with

frameworks consisting of N_4, N_3O_1, N_2O_2, N_1O_3, and O_4. The computed values of the stability constants support the formation of these complexes, which proved to be as beneficial as the main compound N_4. The hydrogen atom transfer from dihydroanthracene i.e., the rate determining step of the C-H activation has been investigated in both triplet and quintet spin states. Due to the presence of exchange enhanced reactivity and two-state-reactivity phenomenon S=2 was found to be more reactive in all five cases. An interesting reactivity trend, namely, the C-H activation reactivity gradually increases with the enrichment of the 'O' in TMC macrocycles i.e., $N_4 < N_3O_1 < N_2O_2 < N_1O_3$, and O_4, irrespective of all the computed levels of theories. The increased reactivity in the substituted compounds may be to some extent explained by the TS being a reactant like with the oxygen substituted TMC, as seen by the length of the breaking and forming bonds. This is further reflected in the form of distortion energy pattern which requires progressively less energy for the substituted TMC complexes. Since spin state gap is identical in all the complexes it is not the main governing factor in this case. Additionally, the energy of the electron acceptor orbital, or LUMO energy, which progressively drops with the number of oxygen-enriched macrocycles, was likewise connected with the reactivity pattern. The weak ligand field on moving from N_4 to O_4 is evident from the charge transfer values. An interesting pattern was also observed in case of quantum mechanical tunneling (QMT) and H/D KIE, which continually decreases with transformation from N_4 to O_4. This might be explained by the broad H-transfer curvature as predicted by the low imaginary frequencies in the transition states. The barrier cutting amount by QMT was not significant enough to alter the classical reactivity trend. Our results are also in lines with the previous studies conducted on TMC like complexes. At last, these studies if carried out experimentally will make path for alternate complexes other than typical N complexes and hence lead to new choices in this bioinorganic field.

References

1. V. A. Larson, B. Battistella, K. Ray, N. Lehnert and W. Nam, *Nat. Rev. Chem.*, **2020**, 4, 404–419.
2. H. Hirao, F. Li, L. Que and K. Morokuma, *Inorg. Chem*., **2011**, 50, 6637–6648.
3. H. Schwarz, S. Shaik, *Acc. Chem. Res*., **2000**, 33, 139–145.
4. T. Z. H. Gani and H. J. Kulik, *ACS Catal*., **2018**, 8, 975–986.
5. J. England, J. O. Bigelow, K. M. Van Heuvelen, E. R. Farquhar, M. Martinho, K. K. Meier, J. R. Frisch, E. Münck and L. Que, *Chem. Sci*., **2014**, 5, 1204–1215.
6. W. Nam, Y. M. Lee and S. Fukuzumi, *Acc. Chem. Res*., **2014**, 47, 1146–1154.
7. K. Rydel-Ciszek, React. Kinet. Mech. *Catal.*, **2021**, 133, 579–600.
8. A. N. Biswas, M. Puri, K. K. Meier, W. N. Oloo, G. T. Rohde, E. L. Bominaar, E. Münck and L. Que, *J. Am. Chem. Soc*., **2015**, 137, 2428–2431.

9. Y. Wang and K. Han, *J. Biol. Inorg. Chem*., **2010**, 15, 351–359.
10. S. P. de Visser, M. G. Quesne, B. Martin, P. Comba and U. Ryde, *Chem. Commun.*, **2014**, 50, 262–282.
11. E. Masferrer-Rius, M. Borrell, M. Lutz, M. Costas and R. J. M. Klein Gebbink, *Adv. Synth. Catal*., **2021**, 363, 3783–3795.
12. C. A. Joseph and M. J. Maroney, *Chem. Commun*., **2007**, 3338–3349.
13. M. Sallmann, S. Kumar, P. Chernev, J. Nehrkorn, A. Schnegg, D. Kumar, H. Dau, C. Limberg and S. P. De Visser, *Chem. - A Eur. J.*, **2015**, 21, 7470–7479.
14. A. J. Johansson, M. R. A. Blomberg and P. E. M. Siegbahn, *J. Phys. Chem. C*, **2007**, 111, 12397–12406.
15. W. Nam, *Acc. Chem. Res*., **2007**, 40, 522–531.
16. S. Impeng, S. Siwaipram, S. Bureekaew and M. Probst, *Phys. Chem. Chem. Phys*., **2017**, 19, 3782–3791.
17. K. Warm, A. Paskin, U. Kuhlmann, E. Bill, M. Swart, M. Haumann, H. Dau, P. Hildebrandt and K. Ray, *Angew. Chemie - Int. Ed*., **2021**, 60, 6752–6756.
18. H. Park and D. Lee, *Chem. - A Eur. J.*, **2020**, 26, 5916–5926.
19. C. V. Sastri, J. Lee, K. Oh, J. L. Yoon, J. Lee, T. A. Jackson, K. Ray, H. Hirao, W. Shin, J. A. Halfen, J. Kim, L. Que, S. Shaik and W. Nam, *Proc. Natl. Acad. Sci. U. S. A.*, **2007**, 104, 19181–19186.
20. R. Kumar, B. Pandey, A. Sen, M. Ansari, S. Sharma and G. Rajaraman, *Coord. Chem. Rev*., **2020**, 419.
21. A. Ansari, A. Kaushik and G. Rajaraman, *J. Am. Chem. Soc*., **2013**, 135, 4235-4249.
22. M. Mandal, C. E. Elwell, C. J. Bouchey, T. J. Zerk, W. B. Tolman and C. J. Cramer, *J. Am. Chem. Soc*., **2019**, 141, 17236–17244.
23. J. E. M. N. Klein and G. Knizia, *Angew. Chemie - Int. Ed*., **2018**, 57, 11913–11917.
24. J. M. Mayer, *Acc. Chem. Res.*, **2011**, 44, 36–46.
25. D. Usharani, D. C. Lacy, A. S. Borovik and S. Shaik, *J. Am. Chem. Soc*., **2013**, 135, 17090-17104.
26. M. K. Goetz and J. S. Anderson, *J. Am. Chem. Soc*., **2019**, 141, 4051−4062.
27. T. H. Yosca, J. Rittle, C. M. Krest, E. L. Onderko, A. Silakov, J. C. Calixto, R. K. Behan and M. T. Green, *Science*, **2013**, 342, 825−829.
28. M. T. Green, J. H Dawson and H. B. Gray, *Science*, **2004**, 304, 1653−1656.
29. P. J. Donoghue, J. Tehranchi, C. J Cramer, R. Sarangi, E. I. Solomon and W. B. Tolman, *J. Am. Chem. Soc*., **2011**, 133, 17602−17605.
30. D. Dhar, G. M. Yee, T. F. Markle, J. M. Mayer and W. B. *Tolman, Chem. Sci*., **2017**, 8, 1075−1085.
31. N. I. Burzlaff, P. J. Rutledge, I. J. Clifton, C. M. H. Hensgens, M. Pickford, R. M. Adlington, P. L. Roach and J. E. Baldwin, *Nature*, **1999**, 401, 721–724.
32. P. L. Roach, I. J. Clifton, C. M. H. Hensgens, N. Shibata, C. J. Schofield, J. Hajdu and J. E. Baldwin, *Nature*, **1997**, 387, 827–830.
33. J. Deutscher, P. Gerschel, K. Warm, U. Kuhlmann, S. Mebs, M. Haumann, H. Dau, P. Hildebrandt, U. P. Apfel and K. Ray, *Chem. Commun.*, **2021**, 57, 2947–2950.
34. L. Kaur and D. Mandal, *Inorg. Chem*., **2022**, 61, 14582–14590.

35. I. Monte Pérez, X. Engelmann, Y. M. Lee, M. Yoo, E. Kumaran, E. R. Farquhar, E. Bill, J. England, W. Nam, M. Swart and K. Ray, *Angew. Chemie - Int. Ed.*, **2017**, 56, 14384–14388.
36. A. Katoch and D. Mandal, *Dalton Trans.*, **2022**, 51, 11641–11649.
37. A. D. Becke, *J. Chem. Phys.*, **1993**, 98, 1372–1377.
38. A. D. Becke, *J. Chem. Phys.*, **1996**, 104, 1040–1046.
39. S. Banerjee and K. Vanka, *ACS Catal.*, 2018, 8, 6163–6176.
40. J. E. M. N. Klein, D. Mandal, W. M. Ching, D. Mallick, L. Que and S. Shaik, *J. Am. Chem. Soc.*, **2017**, 139, 18705–18713.
41. D. Mandal, D. Mallick and S. Shaik, *Acc. Chem. Res.*, **2018**, 51, 107–117.
42. Y. Yang, M. N. Weaver and K. M. Merz, *J. Phys. Chem. A*, **2009**, 113, 9843–9851.
43. P. J. Hay and W. R. Wadt, *J. Chem. Phys.*, **1985**, 82, 299–310.
44. A. V. Marenich, C. J. Cramer and D. G. Truhlar, *J. Phys. Chem. B*, **2009**, 113, 6378–6396.
45. A. V. Marenich, R. M. Olson, C. P. Kelly, C. J. Cramer and D. G. Truhlar, *J. Chem. Theory Comput.*, **2007**, 3, 2011–2033.
46. D. Janardanan, D. Usharani, H. Chen and S. Shaik, *J. Phys. Chem. Lett.*, **2011**, 2, 2610–2617.
47. S. Maeda, Y. Harabuchi, Y. Ono, T. Taketsugu and K. Morokuma, *Int. J. Quantum Chem.*, **2015**, 115, 258–269.
48. E. B. Bauer, *Isr. J. Chem.*, **2017**, 57, 1131–1150.
49. J. P. Cerón-Carrasco and D. Jacquemin, *Phys. Chem. Chem. Phys.*, **2013**, 15, 4548–4553.
50. S. Canneaux, F. Bohr, and E. Hénon, *J. Comp. Chem.*, **2014**, 35, 82-93.
51. H. Eyring, *J. Chem. Phys.*, **1935**, 3, 63–71.
52. C. Eckart, *Phys. Rev.*, **1930**, 35, 1303–1309.
53. D. K. Maity, R. L. Bell and T. N. Truong, *J. Am. Chem. Soc.*, **2000**, 122, 897–906.
54. F. Zhang and T. S. Dibble, *Phys. Chem. Chem. Phys.*, **2011**, 13, 17969–17977.
55. A. G. Vandeputte, M. K. Sabbe, M. F. Reyniers, V. Van Speybroeck, M. Waroquier and G. B. Marin, *J. Phys. Chem. A*, **2007**, 111, 11771–11786.
56. C. Gonzalez and H. B. Schlegel, *J. Chem. Phys.*, **1991**, 95, 5853–5860.
57. M. E. Kirby, A. Simperler, S. Krevor, D. J. Weiss and J. L. Sonnenberg, *J. Phys. Chem. A*, **2018**, 122, 8007–8019.
58. A. Sirjoosingh and S. Hammes-Schiffer, *J. Phys. Chem. A*, **2011**, 115, 2367–2377.
59. S. A. Wilson, J. Chen, S. Hong, Y. M. Lee, M. Clémancey, R. Garcia-Serres, T. Nomura, T. Ogura, J. M. Latour, B. Hedman, K. O. Hodgson, W. Nam and E. I. Solomon, *J. Am. Chem. Soc.*, **2012**, 134, 11791–11806.
60. D. Janardanan, Y. Wang, P. Schyman, L. Que and S. Shaik, *Angew. Chem.*, **2010**, 122, 3414–3417.
61. D. Mandal, R. Ramanan, D. Usharani, D. Janardanan, B. Wang and S. Shaik, *J. Am. Chem. Soc.*, **2015**, 137, 722–733.
62. C. Geng, S. Ye and F. Neese, *Angew. Chem. Int. Ed.*, **2010**, 49, 5717–5720.
63. S. P. De Visser, *J. Am. Chem. Soc.*, **2006**, 128, 15809–15818.
64. S. Ye, C. Y. Geng, S. Shaik and F. Neese, *Phys. Chem. Chem. Phys.*, **2013**, 15, 8017–8030.
65. J. England, J. Prakash, M. A. Cranswick, D. Mandal, Y. Guo, E. Münck, S. Shaik and L. Que, *Inorg. Chem.*, **2015**, 54, 7828–7839.

66. C. V. Sastri, J. Lee, K. Oh, J. L. Yoon, J. Lee, T. A. Jackson, K. Ray, H. Hirao, W. Shin, J. A. Halfen, J. Kim, L. Que, S. Shaik and W. Nam, *Proc. Natl. Acad. Sci. U. S. A.*, **2007**, 104, 19181–19186.

Chapter 5

Computational studies on the impact of commutes in ligand structure on C-H activation in non-heme and heme Iron(IV)-oxo complexes

a) Impact of Ring Size Modifications on the C-H Activation Reactivity of Non-heme Iron(IV)−Oxo Complexes: A Computational Study with TMC Macrocycles

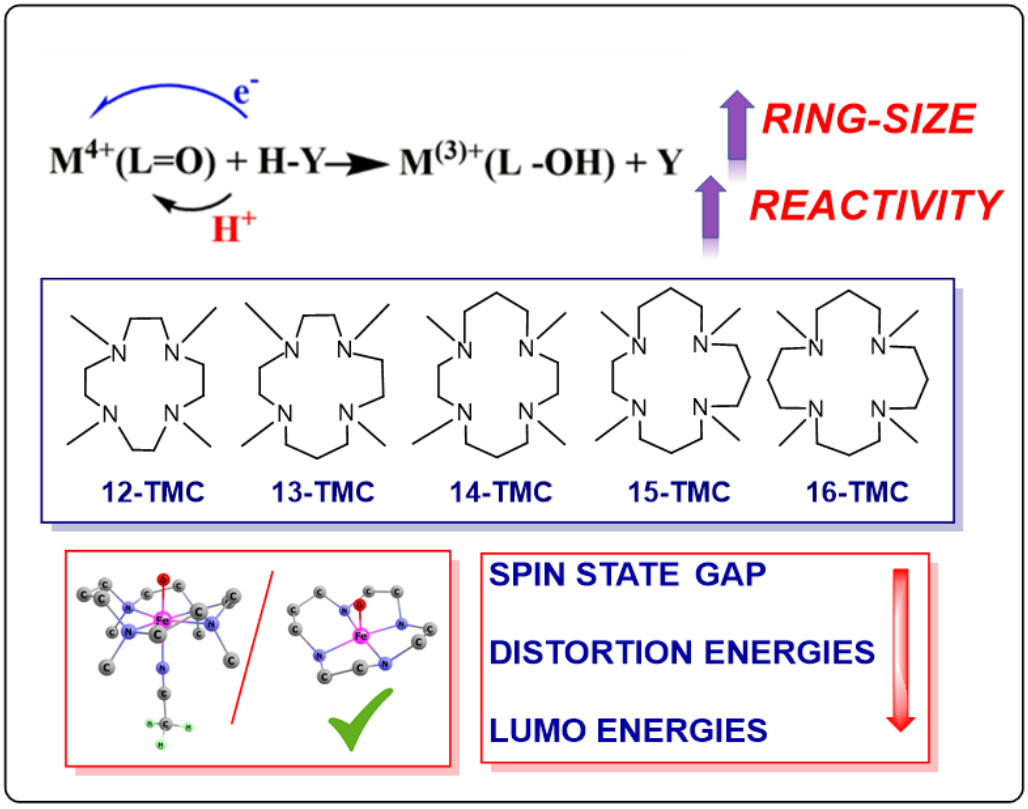

5.1 Introduction

Iron–oxo species in high valent states are one of the most common intermediates in the enzyme catalytic cycles for various oxidation reactions, including C-H activation.[1-11.] These frameworks in mononuclear complexes have been characterised for multiple heme and nonheme enzymes. Lending strong evidence for the notion, we have had numerous studies over the past 15 years where these complexes serve as ideals for reactive intermediates.[12-15] In this biomimetic field, the first crystal structure ([FeIV(O)(TMC)(NCMe)]$^{2+}$ (where TMC is 1,4,8, 11-tetramethyl 1,4,8, 11-tetraazacyclotetradecane; 1-NCMe) was reported by Rohde et al.[16] Since then, several studies of 1-NCMe and analogous complexes have been carried out towards C-H activation.[17-19] These intermediates have been intensively investigated to understand their structures, mechanisms of interconversion, and the factors that control their chemical

reactivities in oxidation reactions. This vastly studied example shows that TMC and its derivatives have proven to be versatile ligands in biomimetic chemistry.[21-22] A few of the most studied ligands have been collected in Scheme 5.1. Various advanced spectroscopic characterization techniques, such as Mossbauer, resonance Raman, X-ray absorption, etc., have demonstrated that the iron (IV)–oxo state can be synthetically accessible in both heme and nonheme ligand environment, i.e., with or without a porphyrin ring with different structural alterations as in Scheme 5.1(a).[23-28] Studies have also shown that supporting ligands of the metal oxo play a vital role in tuning the geometric and electronic structures, stabilities, and reactivities of the oxygen-coordinating metal complexes.

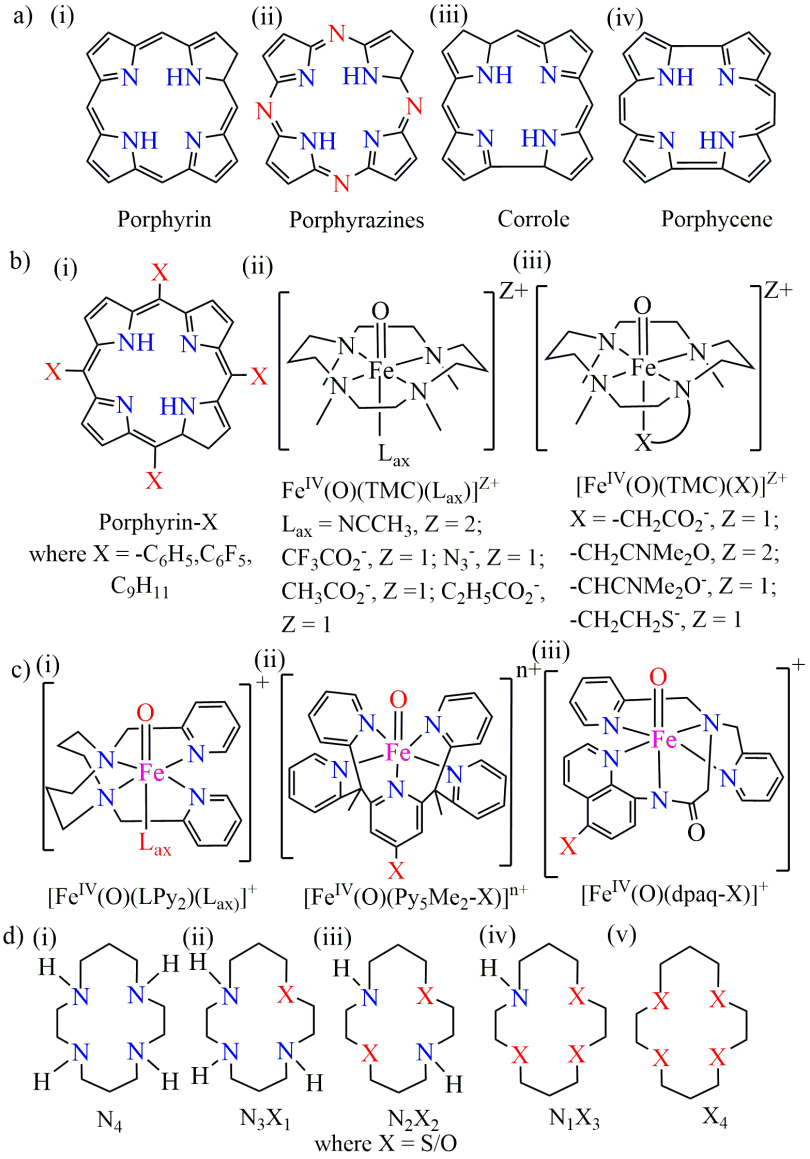

Scheme 5.1: Some of the most commonly used macrocycles make bioinspired high-valent metal oxo complexes for C-H activation. a) Porphyrin and its few analogues b) substituted porphyrin, TMC with different axial ligands, and TMC with tethered axial ligands; (c) a few pyridine-based macrocycles; (d) cylam and S/O substituted cyclam ligands.

Such changes can be made at the axial and equatorial level ligands.[29-32] Vastly studied commutes are supplanting the most common 6th ligand acetonitrile in the axial position (Scheme 5.1(b)) with other ligands, e.g., N_3^- and SR^-, etc., wherein rates of hydrogen atom transfer from dihydroanthracene (DHA) increased upon introducing more electron-donating axial ligands.[33-35] While changes included alterations in the primary coordination sphere, changes were also made in the secondary coordination sphere, directly impacting the reactivity parameters (Scheme 5.1(c)). Modifications were also made at the equatorial position by changing the donor atoms in TMC-like ligands. (Scheme 5.1(d)).[36-37] To dive further in, such derivatives have occasionally been studied in various ring sizes.[38] The ring size effect of such macrocyclic TMC ligands in nonheme iron(IV)- oxo complexes has been examined in the hydrogen atom transfer (HAT) and oxygen atom transfer (OAT) reactions of **13** (without axial ligand) and **14** membered (with axial ligand) rings by S. Hong, et al.[39] With regard to the N-CH_3 and Fe=O moiety, these $[Fe(IV)O\text{-}\mathbf{13}\text{-}TMC]^{2+}$ and $[Fe(IV)O\text{-}\mathbf{13}\text{-}TMC(CH_3CN)]^{2+}$ are in their syn and anti forms, respectively. As a result, a consistent and comprehensive assessment of the C-H activation reactivity of Fe(IV)O complexes with diverse ring sized macrocycles and in the presence as well as the absence of the axial ligands becomes necessary. Hence in this article, we consider the possibility of a ring size ligand effect (n-TMC) with n = **12**, **13**, **14**, **15**, and **16**, as presented in scheme 5.2.

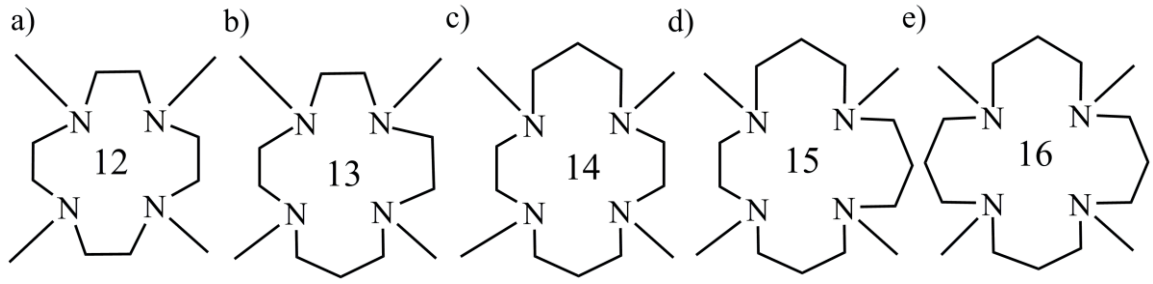

Scheme 5.2. Proposed structures of complexes from ring sizes n = **12** to **16** in our studies.

The reactivity and mechanism of C-H activation have been examined utilizing derivative complexes created sequentially extending the ring size framework, i.e., **12**, **13**, **14**, **15**, and **16**, membered TMC rings, with DHA as substrate. A step wise increase in ring size would allow us to establish a trend in how ring size influences reactivity and kinetics. Many factors influence reactivity, including various spin state paths, deformation energy to produce transition states, and, most critically, acceptor orbital energies, all of which have been thoroughly investigated herein. To better understand the typical trend, modifications were made for complexes without the axial ligand CH_3CN (n = **13** and **14**) as well. We have also extended the investigation to

verify the experimental observation related to the higher C-H activation reactivity of syn [Fe(IV)O(**13**-TMC)]$^{2+}$ compared to the anti [Fe(IV)O(**14**-TMC)CH_3CN]$^{2+}$.[39]

5.2 Computational Details

Geometry optimizations for all the species have been conducted using the DFT-B3LYP method. The B3LYP functional is based on Becke's three-parameter exchange with Lee-Yang, and Parr's correlation functional.[40,41] A benchmark and several independent studies support this functional for a model C-H activation reaction catalysed by iron-oxo complexes, proving its use here. To further validate some novel spin state gaps, DFT methods, e.g., M06-L and TPSSH, have also been brought into practice, as these have been reported to be the most suitable functionals in this type of system.[42] The LANL2DZ[43] with the same ECP (for Fe) and Pople's double zeta 6-31G (d,p) (for the rest of the atoms) basis set (labelled as B1) have been used.[44-46] The presence of acetonitrile as a solvent is also computed using the self-consistent reaction field (SCRF) and CPCM model.[47] Further energy refinement with the help of single-point calculations has also been done using 6-311++G (2d,2p) for all atoms and ECP containing SDD for iron using the same solvent model (B2). Free energy values are also computed using the all-electron basis set Def2TZVPP,[48] labelled as B3. Additionally, geometries have also been optimised using SDD for Fe and 6-31G (d,p) for the rest of the atoms (B4) and refined using SDD for iron and 6-311++G (2d,2p) for the rest of the atoms using the same solvent model (B5).The empirical dispersion has also been incorporated using Grimme's GD3BJ method.[49] A detailed study of the $[Fe^{IV}(O)N_4Py]^{2+}$ complex has shown that the usage of counterions in order to neutralise the charge of the oxidants caused secondary interactions to vanish,[50] so to deal with these effects, here we neutralised the charge of the iron (IV)−oxo reagents with triflate ($CF_3SO_3^-$) counterions held at the bottom parts of the axial ligands as depicted in Fig. 5.1.

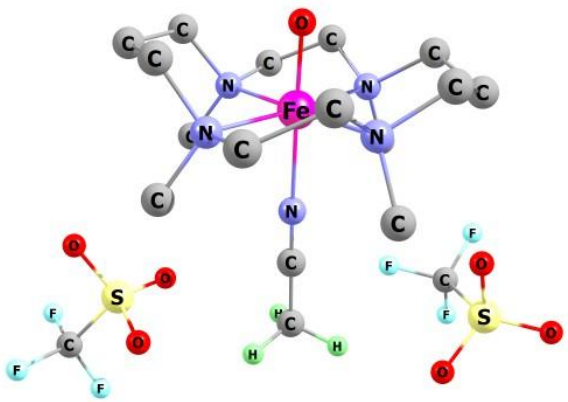

Figure 5.1: Depiction of placement of counter ions w.r.t to Oxidant 14-TMC.

A subsequent frequency calculation has also been carried out at the same B1 level to confirm the nature of the optimised structures as local minima (no imaginary frequency) or transition states (one imaginary frequency) and to evaluate the zero-point vibrational energy (ZPVE), as well as thermal and entropic corrections to the Gibbs free energy at T = 298.15 K. Intrinsic reaction coordinate (IRC) calculations have been performed to further verify if the transition states are connecting the proper minima or not. Spin densities and Mulliken charges have been analysed[51] for the correct identification of the electronic states. All computations were carried out using Gaussian 16 program packages[52] while Chemcraft software was used for the visualization and production of natural orbitals.[53] The percentage of buried volumes (%Vbur) has been calculated using the SambVca 2.1 program.[54]

5.3 Results and Discussions

We first analysed the structure of oxidants. Since many conformations are possible considering the position of substituents on the donor atom atoms (CH_3) with respect to the O atom (of Fe=O) so that we can study the most stable conformations for our analysis. Most stable structures turn out to be anti from n =**12-14** and mixed in n =**15**,**16.** The optimised structures with these conformations for different ring sizes have been presented in the following Fig. 5.2.

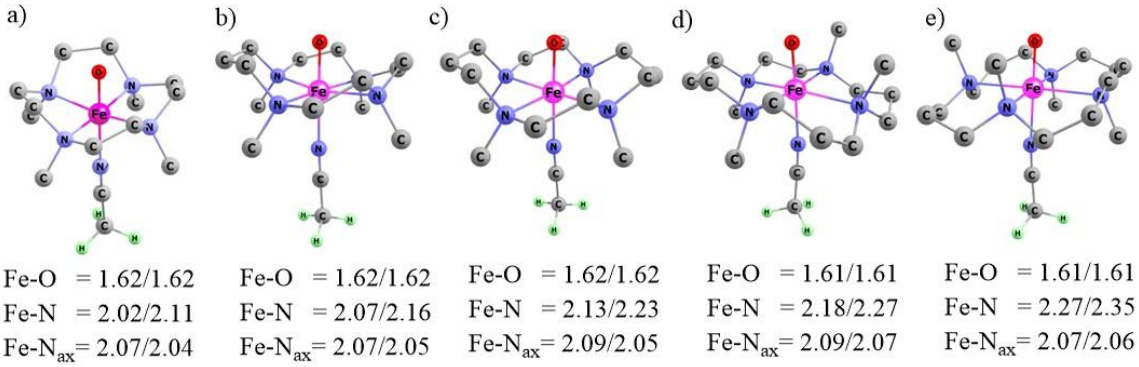

Figure 5.2: Structures of TMC complexes with different ring sizes along with structural parameters a) **12** b) **13** c) **14** d) **15** and e) **16**, wherein parameters are represented as triplet/quintet states, respectively.

The bond parameters have been compared with the previously reported X-ray structure data of **14**-TMC, and it is safe to say that the values are in agreement with the previously reported ones as they differ merely by 0.029-0.044 Å as depicted in the Table 5.1.[16] [Cambridge Crystallographic Data Centre (CCDC) reference number: 192768] Looking at the quintet oxidants, one common observation is that the Fe-O bond distance is identical in all the species, i.e., Fe-O = 1.61-1.62. Å. However, as the ring size becomes bulkier, the Fe-N average distances ($Fe\text{-}N_{av}$) increase stepwise from 2.11 to 2.16 to 2.23 to 2.27 to 2.35 Å, going on from

n = **12** to **16**, which might have an influence on the reactivity pattern by weakening the ligand effect.

Table 5.1. Crystallographic and computational parameters for $[FeO(IV)(\mathbf{14}\text{-TMC})(CH_3CN)]^{2+}$

Bond	Crystallographic	Computational
Fe-O	1.646 (3)	1.617
$Fe\text{-}N_{av}$	2.088 (3)	2.132
$Fe\text{-}N_{ax}$	2.058 (3)	2.089

Looking at the quintet oxidants, one common observation is that the Fe-O bond distance is identical in all the species, i.e., Fe-O = 1.61-1.62. Å. However, as the ring size becomes bulkier, the Fe-N average distances ($Fe\text{-}N_{av}$) increase stepwise from 2.11 to 2.16 to 2.23 to 2.27 to 2.35 Å, going on from n = **12** to **16**, which might have an influence on the reactivity pattern by weakening the ligand effect.

5.3.1 Spin State Reactivity

We have determined the favourable spin states of the central metal, Fe, as Fe (IV) complexes can have both low spin (S =1, triplet state) and high spin (S = 2, quintet state) states for the hydrogen atom transfer (HAT) mechanism.[55-56] The electron rearrangement in both spin states has been presented using Figure 1.6. We showed two probable paths for this reaction mechanism relying on the spin state. Panel a) of Figure 1.6 demonstrates the low spin, i.e., S=1 pathways where a β electron from the $\sigma_{C\text{-}H}$ bond shifts to one of the π* orbitals of the central metal, which is the π pathway/trajectory. Here, the Fe-O-H angle has an orientation of ~120°. Panel b) is for the high spin path where one α electron from the $\sigma_{C\text{-}H}$ bond of the substrate shifts to the σ^*_{dz2} anti-bonding orbital of Fe=O. Here, the substrate accesses the oxidant through the upper side with a Fe-O-H angle ~180° angle. This pathway is counted as σ pathway/trajectory. Mostly, for the Fe(IV)O complexes, reactants at the S=2 state possess higher energy than S=1, which becomes lower through the transition state and is where two-state reactivity (TSR) comes into play[57-60] The TSR phenomenon may become more critical due to the steric inhibition of π trajectory or submissiveness when there is no substantial hindrance.[61,62]

5.3.2 Spin State Energy Difference

Here, we have observed that as we move from the ligand size **12** through **13**, **14**, **15** to **16**, the spin state gap ($\Delta E_{T\text{-}Q}$) goes on decreasing (13.4 < 9.7 < 5.5 < 0.7 in kcal/mol) in a sequential manner, and for n = **16** the S = 2 become more stable by 4.0 kcal/mol. At the higher level (B3)

ΔG_{298} values, for **12-14**, S = 1 is found to be more stable by 10.8, 6.0, and 0.5 kcal/mol, respectively, whereas S =2 dominates from n = **15**, **16** holding stability by 2.8 and 7.9 kcal/mol. To further verify these outcomes, we have also used M06-L and TPSSH density functionals for **15** and **16** TMC complexes and observed the same trend, i.e. **15** and **16** -TMC complexes have quintet as their ground state. The data related to spin state gaps is collected in the Table 5.2 below.

Table 5.2: ΔE_{T-Q} gaps for n=15,16 in (B5+ZPE/G_{298K}) format.

Ring Size	B3LYP	M06-L	TPSSH
15-TMC	-2.8/-3.6	-1.6/-2.4	-0.3/-1.2
16-TMC	-7.4/-6.3	-6.8/-5.7	-5.2/-4.1

The physical insight into this typical ΔE_{T-Q} pattern might be hidden in the energy gap between the d_{xy} and $d_{x^2-y^2}$ orbitals of the oxidant, which is basically considered orbital promotion energy. On moving from **12**-TMC to **16**-TMC, the energy gap between the said orbitals drops, making it feasible for the incoming electron to enter the $d_{x^2-y^2}$ orbital, which thereby formed a high spin species. A correlation diagram of ΔE_{T-Q} with the orbital promotion energy has been presented in Fig. 5.3.[63]

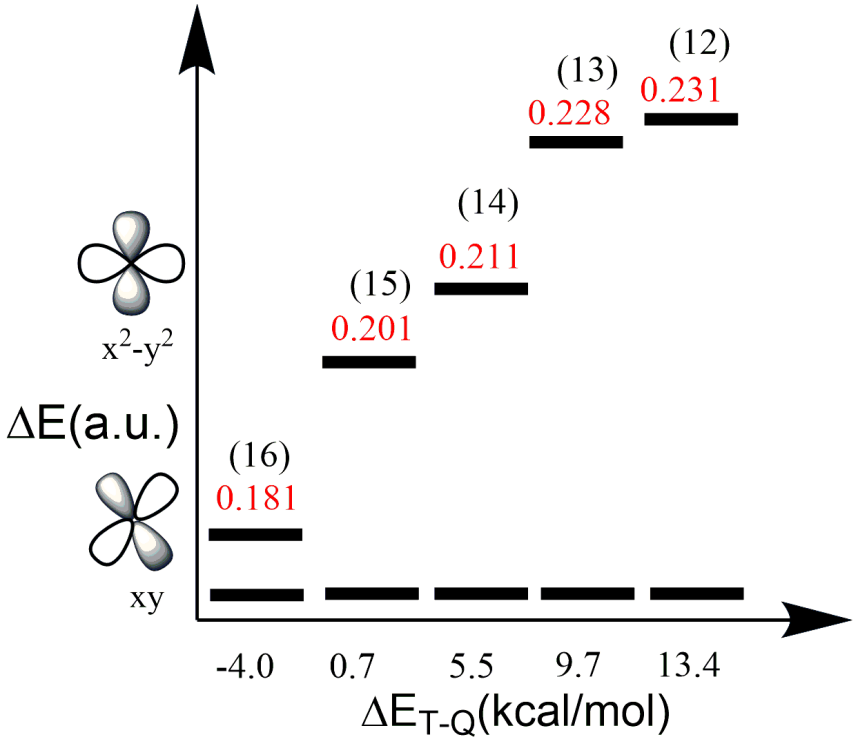

Figure 5.3: Depiction of spin state gaps alongside the orbital promotion energy of the $[Fe(IV)O(n\text{-}TMC)(CH_3CN)]^{2+}$ complexes for n =**12-16.**

5.3.3 Transition State (TS) Parameters

Quintet TS are depicted in Figure 5.4 along with the parameters and imaginary frequencies. On observing the parameters of the quintet TS, we observe that there is no significant difference or trend in the C-H, O-H and Fe=O bond distances. The values of imaginary frequencies can be depicted as *815.2i* (n =**12**), *1139.3i* (**13**), *882.4i* (**14**), *606.1i* (**15**), and *388.6i* (**16**). Fe-N distances in the rings go on increasing from 2.12 to 2.17 to 2.24 to 2.30 to 2.37 on a sequence wise increase in size to overcome steric hinderance.

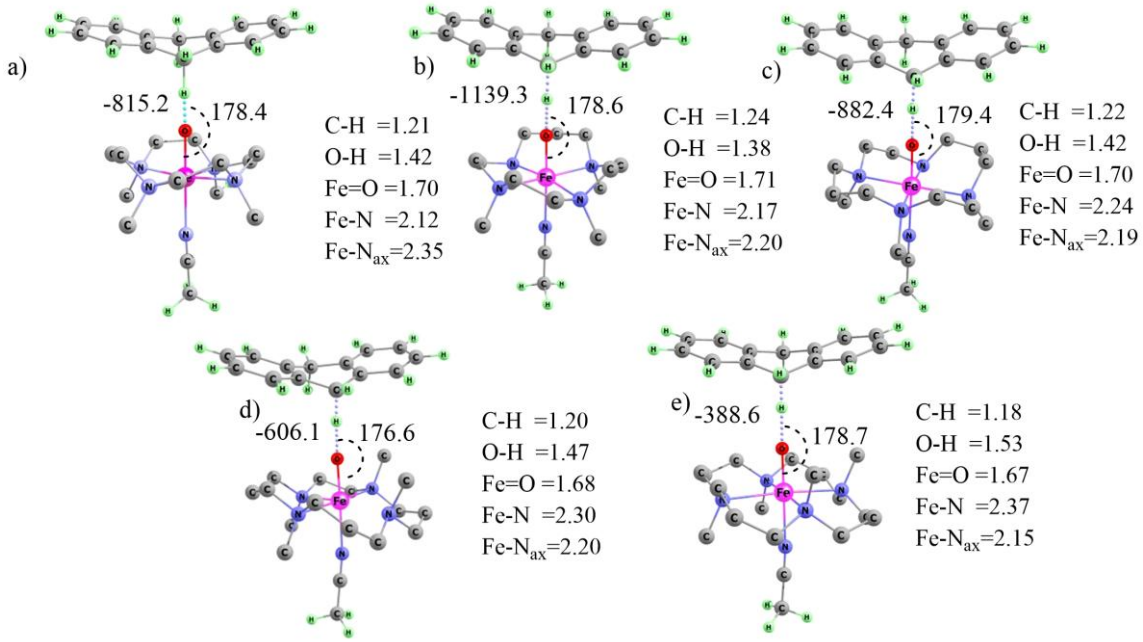

Figure 5.4: Quintet TS with parameters of a) **12**, b) **13**, c) **14**, d)**15**, and e) **16** ring sizes with axial ligands.

5.3.4 Reactivity Pattern

Regarding the order of reactivity in terms of transition state stability, we have researched both states. At B1, S=1 is slightly more reactive in the case of n =**12**, whereas S =2 has lower activation barriers for the rest as depicted in the Figure 5.5 here. The energy values are given for ΔG_{298K}(B3). The trend of the reactivity looks like 23.1 (**12**), 23.0 (**13**), 16.0 (**14**), 8.2 (**15**), and 6.7 (**16**), and for ΔG_{298K} (B2) , S=2 is always more reactive and the activation energy possesses 27.3 (**12**), 24.1 (**13**), 18.5 (**14**), 15.4 (**15**), and 13.3 (**16**) in kcal/mol. Talking about ΔG_{298K} (B3) the trend is 32.5 (**12**), 28.5 (**13**), 21.3 (**14**), 18.6 (**15**), and 15.7 (**16**) in kcal/mol. The number in the bracket defines the ring size. These patterns can be seen in the potential energy surface presented in Figure 5.5.

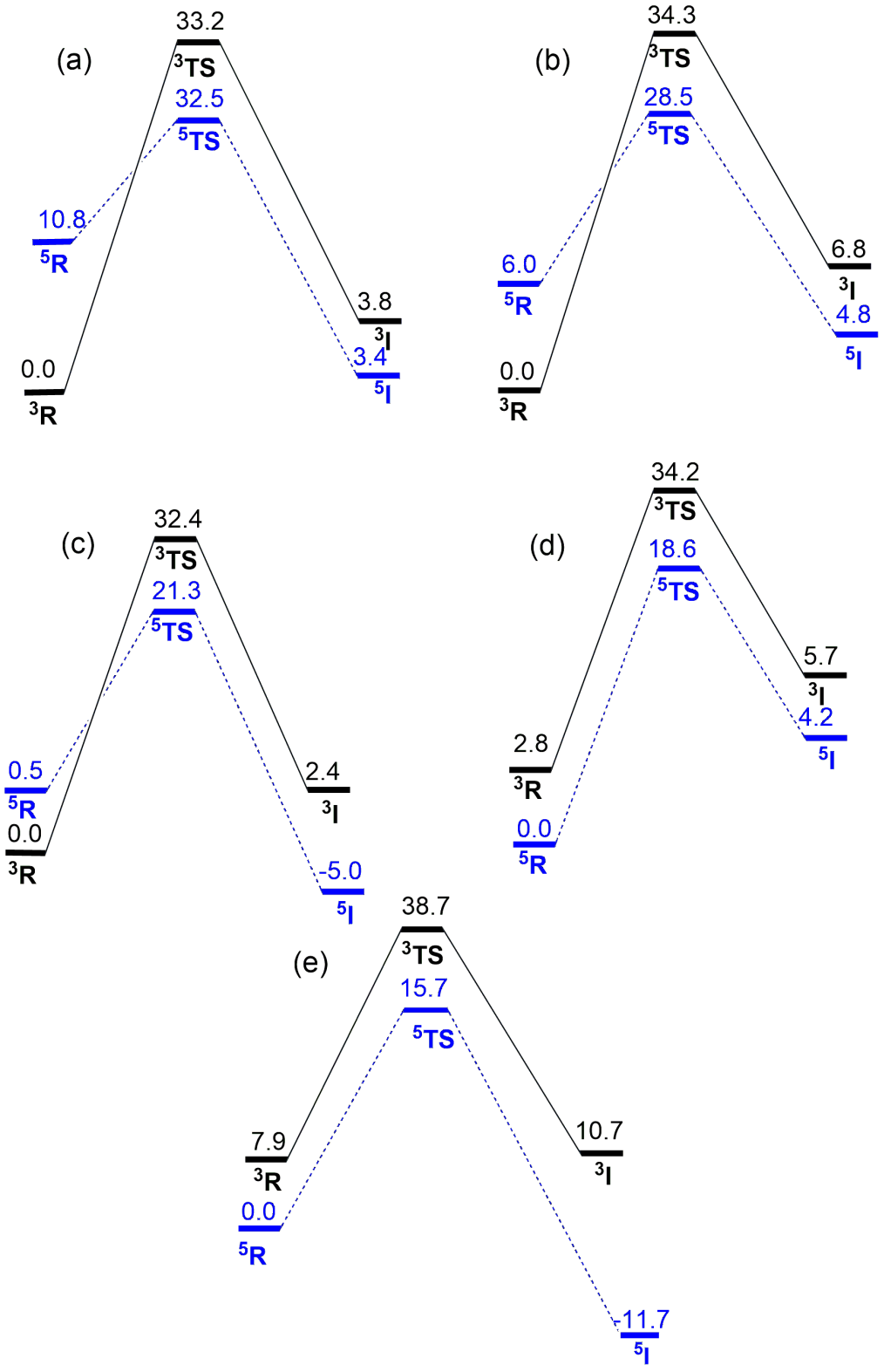

Figure 5.5: The potential energy surface, and the geometry of transition states with corresponding imaginary frequencies for the C-H activation are catalysed by the Fe(IV)O complex framed with a) **12** b) **13** c) **14** d) **15** and e) **16** membered rings. The black and blue lines represent the S=1 and S=2 state pathways, respectively.

Further details, encompassing B4 and B5 are presented in the subsequent Table 5.3.

Table 5.3. Relative energies (in kcal mol^{-1}) of oxidants, transition states and intermediates for the C-H activation catalysed by Fe(IV)O with different ring macrocycle and presence of axial ligand CH_3CN computed at different levels of theory where B4 is 6-31G**/SDD(Fe) and B5 is 6-31++G(2d,2p)/SDD(Fe).

Reactants	Spin State	Species	B4 + ZPE	B5 + ZPE	$G5_{298K}$	$G5^{dis}{}_{298K}$
12-TMC	S=1	^{3}R+S	0.0	0.0	0.0	0.0
		^{3}TS	24.9	19.5	31.6	18.6
		^{3}IH	-1.4	-7.3	-0.2	-9.7
	S=2	^{5}R+S	10.8	10.5	9.6	10.5
		^{5}TS	24.7	19.0	28.5	18.1
		^{5}IH	-12.6	-16.0	-13.3	-19.2
13-TMC	S=1	^{3}R+S	0.0	0.0	0.0	0.0
		^{3}TS	23.7	20.1	34.7	19.0
		^{3}IH	-0.4	-7.4	1.9	-8.9
	S=2	^{5}R+S	5.9	5.5	4.3	7.1
		^{5}TS	19.1	13.6	24.5	13.1
		^{5}IH	-0.8	-8.6	-1.8	-13.1
14-TMC	S=1	^{3}R+S	0.0	0.0	0.7	2.7
		^{3}TS	24.2	19.3	32.2	20.0
		^{3}IH	-1.7	-8.9	2.6	-6.4
	S=2	^{5}R+S	1.7	0.9	0.0	0.0
		^{5}TS	12.3	6.9	18.2	6.2
		^{5}IH	-8.1	-15.3	-5.6	-16.7
15-TMC	S=1	^{3}R+S	2.7	2.8	3.6	1.2
		^{3}TS	24.0	19.6	32.9	16.0
		^{3}IH	-0.9	-7.5	4.0	-8.8
	S=2	^{5}R+S	0.0	0.0	0.0	0.0
		^{5}TS	7.4	3.0	13.7	2.9
		^{5}IH	-13.9	-20.9	-10.5	-19.7
16-TMC	S=1	^{3}R+S	7.2	7.4	6.3	4.6
		^{3}TS	26.6	23.6	34.7	19.3
		^{3}IH	3.3	-2.9	5.2	-6.8
	S=2	^{5}R+S	0.0	0.0	0.0	0.0
		^{5}TS	5.8	3.6	10.1	2.1
		^{5}IH	-22.6	-31.8	-26.3	-32.1

5.3.5 Reactivity of the Complexes Without Axial Ligands

We have also performed the reactivity analysis without the axial ligand counterparts of the complexes for n =**13** and **14**, providing two important conclusions. First, the notion that reactivity increases with the increment in ring size is also supported here as the barriers for the more reactive states (S=2) are 19.4, and 14.1 kcal/mol. The free energy barrier (ΔG_{298K}) at B2 (S = 2) is 16.6, and 13.0 kcal/mol. The second fascinating observation is that these complexes are more reactive than those with axial ligands. We have represented the barrier as with axial/without axial ligand, and the values are 23.0/19.4 (**13**), and 16.0/14.1 (**14**). For ΔG_{298} at B2, 24.1/16.6 (**13**), and 18.5/13.0 (**14**). Further details are presented here in Table 5.4.

Table 5.4. Relative energies (in kcal mol^{-1}) of oxidants, transition states and intermediates for the C-H activation catalysed by Fe(IV)O complex with different sized macrocycle in absence of axial ligand computed at different levels of theory where B1 is 6-31G**/LANL2DZ(Fe) and G_{298K} is calculated using 6-31++G(2d,2p)/SDD(Fe).

Reactants	Spin State	Species	B1 + ZPE	ΔG_{298K}
13-TMC	S=1	^{3}R+S	0.0	0.0
		^{3}TS	19.8	24.4
		^{3}IH	-4.8	-8.9
	S=2	^{5}R+S	13.7	7.0
		^{5}TS	19.4	16.6
		^{5}IH	-5.6	-23.1
14-TMC	S=1	^{3}R+S	0.0	0.0
		^{3}TS	19.5	25.0
		^{3}IH	-6.1	1.0
	S=2	^{5}R+S	10.4	2.9
		^{5}TS	14.1	13.0
		^{5}IH	-12.2	-28.5

5.3.6. Comparison with Experiment

Experiment studies have been conducted on syn $[Fe(IV)(O)(\mathbf{13}\text{-TMC})]^{2+}$ and anti $[Fe(IV)O(\mathbf{14}\text{-TMC})(CH_3CN)]^{2+}$.[39] When comparing the C-H reactivity of the two at a temperature of -40°C, the reactivity order varied by approximately 3.0×10^3 times, which indicates that the syn $[Fe(IV)(O)(\mathbf{13}\text{-TMC})]^{2+}$ exhibited a higher level of reactivity. In an attempt to validate these results, we performed theoretical studies on the same complexes. It was found out that the first complex possesses a reaction barrier of 11.8 kcal/mol for H-abstraction from DHA, whereas for the second complex it is 12.3 kcal/mol giving us the reactivity order agreeing with the in vitro results. This reactivity pattern might have been observed due to the axial ligand effect, as reported in the current investigation and has been depicted in Table 5.5.

Table 5.5. Relative energies (in kcal mol^{-1}) of oxidants, transition states and intermediates for $[Fe(IV)(O)(13\text{-TMC})]^{2+}$ (syn) and $[Fe(IV)O(14TMC)(CH_3CN)]^{2+}$ (anti) computed at different levels of theory where B1 is 6-31G**/SDD(Fe) and B2 is calculated using 6-31++G(2d,2p)/SDD(Fe).

Reactions	Spin State	Species	B1 + ZPE	B2 + ZPE
13-TMC	S=1	^{3}R+S	0.0	0.0
		^{3}TS	13.3	6.9
		^{3}IH	-9.5	-17.4
	S=2	^{5}R+S	7.1	5.7
		^{5}TS	11.8	4.2
		^{5}IH	-17.9	-27.5
14-TMC	S=1	^{3}R+S	0.0	0.0
		^{3}TS	24.2	19.3
		^{3}IH	-1.7	-8.9
	S=2	^{5}R+S	1.7	0.9
		^{5}TS	12.3	6.9
		^{5}IH	-8.1	-15.3

5.3.7 Insights into the Reactivity

We have tried to understand the reason behind the reactivity pattern through several factors, including:

a) Steric Hindrance

To educate us about the steric hindrance inside the first coordination sphere of the various iron complexes, the percentage of buried volumes (%Vbur) has been calculated for macrocycles with axial ligand present. These values reflect the fraction of the sphere around the metal center occupied by the ligand. The results showed the steric bulk of the various ring size. As the ring size increased, so did the accessibility of Fe=O for the HAT reactions, as %Vbur changed from 81.2 to 80.3 to 78.9 to 78.3 to 76.2 on moving from ring size **12** to **16**, thereby supporting the predicted reactivity trend.

b) Distortion Energy

To dive further into the reason behind the reactivity pattern, we have looked for the trend of distortion energy, $\Delta E^{\ddagger}_{dis}$, of the two reactants in their quintet transition state (^{5}TS) geometries relative to their geometries at the S = 2 reactant state which would signify the change in the geometry undergone. The computed $\Delta E^{\ddagger}_{dis}$ have been probed, and the lowest $\Delta E^{\ddagger}_{dis}$ has been found for **16** (5.9 kcal/mol), whereas the highest is for **12** (18.1 kcal/mol) for **13**, **14**, and **15**; the values are 12.9, 10.1 kcal/mol and 6.8 kcal/mol respectively as seen in the plot given in Fig.5.6. This might be a good explanation of the sequential order of predicted reactivity.

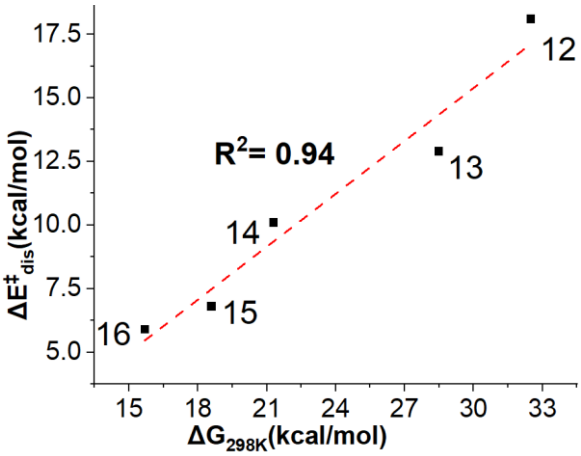

Figure 5.6: A plot of free energy (ΔG_{298K}) versus distortion energy ($\Delta E^{\ddagger}_{dis}$) for the S=2 pathways. Both the values are presented in kcal/mol.

Further classification of the contribution of substrate and oxidant towards the distortion energies indicates that both substates and oxidants required less deformation energy to achieve

the transition structure for higher ring sized complexes. The values have been shown in the Table 5.6.

Table 5.6: Distortion energy values (in kcal/mol) for substrates and oxidants of various ring sizes with axial ligands. *

Complex	Substrate	Oxidant
12	5.28	12.81
13	6.33	6.60
14	4.89	5.21
15	2.88	3.89
16	2.96	2.98

*The values have been calculated as $E_{dist} = (E_{R'} + E_{S'}) - (E_R + E_S)$ where R' and S' refer to the reactant and substrate counterparts in the TS structure.

c) The Energy of the Electron Acceptor Orbital

As we observed sequence wise increase in the distances of Fe with equatorial N (Fe-N average) as higher ring size ligand offers bigger cavity in the centre, this must have made the ligand effect weaker which mostly decreases the energy of the acceptor orbital i.e., LUMO to facilitate the reaction. To confirm if this is the case we considered the energy of the electron acceptor orbitals to gain further insight into the reactivity pattern. As reactions mostly proceed through the quintet state, the lowest unoccupied molecular orbital (LUMO), i.e., $\sigma^*_{z^2}$ orbital, plays the role of acceptor orbitals. The energies of the LUMO show a consequent reduction in the sequential enhancement in the ring size.

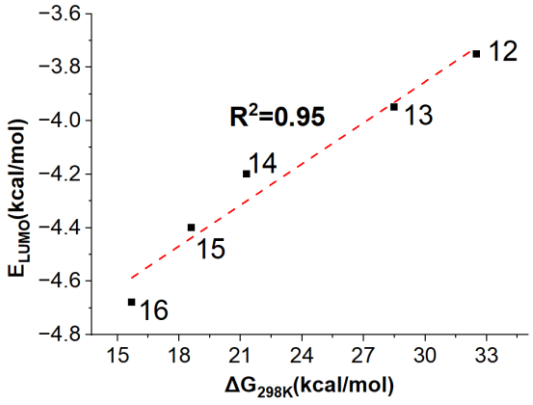

Figure 5.7: A plot of ΔG_{298K} (kcal/mol) versus the energy of the LUMO (E_{LUMO} in kcal/mol) of the oxidants.

It is reasonably expected that the lower energy of the acceptor orbital in an oxidant implies the more efficient nature of the abstractor. The values for n = **12**, **13** decrease from -3.75 to -3.95 eV, and there is an apparent reduction further on as we move on from n =**14** to **16** (values being -4.20, -4.40, and -4.68 eV, respectively). So, it's safe to claim here that we get the observed reactivity pattern due to successive falls of E_{LUMO} from **12** to **16**, as manifested in Figure 5.8. The LUMO values for without axial counterparts agree with our results too, with values being -4.62 for n =**13** (without) which is significantly lower than -3.95 (with) as mentioned above. Likewise, -4.89 for n =**14** (without) and -4.20 (with). Hence it is safe to say that the presence of the axial ligand modulates the energy of accepter orbital, thereby effecting the reaction dynamics.

d) Quantum Mechanical Tunneling

We have also performed calculations to see if quantum mechanical tunneling plays a role. The values thereby obtained for Wigner calculations for S=1/S=2 was 9.00/4.92 (**12**), 9.00/6.29 (**13**), 9.07/5.02 (**14**), and 9.02/3.82 (**15**). Eckart values for the same were 962.77/5.43 (**12**), 376.10/9.35 (**13**), 297.37/5.75 (**14**), and 153.64 (**15**); hence we can see it is negligible in the more reactive quintet state. So, we can conclude that tunneling does not correlate with the ring size. The calculated tunneling corrected kinetic isotope values for S = 2 show less than 10, which is also in good agreement with the earlier experiment and computation.[4,64]

5.4 Conclusions

Theoretical explication of the geometric structures and hydrogen-abstraction mechanisms for the $[Fe(IV)=O(n\text{-}TMC)(CH_3CN)]^{2+}$ complexes with different ring sizes (n =**12** to **16**) has been addressed here. Furthermore, these studies have also been extended in the presence and absence of the axial ligand wherever possible. DHA is the substrate used for comparing the C-H activation reaction rates of the said complexes, in which both the electron and proton traveled simultaneously, where H linked with O and the electron shifted to metal –d orbital. The expected two-state reactivity that has the exchange enhanced interaction by the presence of unpaired electrons in the C-H activation catalysed by Fe(IV)O complexes has played its part. A spin crossover was witnessed from ground S =1 to the excited S =2 state as the reaction proceeded. Coming to the observations, DFT calculations revealed that reactivity followed an increased trend by moving on from n = **12** to **16**. The activation energy lowered sequentially from **12** to **13** to **14** to **15** to **16** membered rings as explained through several perspectives, e.g., spin state gap, accessibility of the abstractor Fe=O, energy of the electron acceptor orbital, deformation energies, etc. In continuation, the reactivity in the absence of axial ligands follows

the same trend as barriers lower from **13** to **14**. The complexes also show higher reactivity in the absence of axial ligands compared to their axially ligated counterparts. Our computation was also able to replicate the experimentally observed higher reactivity of syn **13**-TMC complexes compared to anti-**14** TMC complexes. This pattern was observed due to their specific conformation along with absence and presence of axial ligands, which also follow the energy of the acceptor orbital trend. We also calculated the KIE for these reactions. Both Wigner and Eckart-corrected values were considered, implying the ring sizes did not impact these values, and hence the contribution was negligible in this case. In conclusion, we can confidently infer from this prediction that compounds with larger ring sizes will exhibit stronger C-H activation catalysis if and when their synthesis is feasible.

References

1. J. England, J. O. Bigelow, K. M. Van Heuvelen, E. R. Farquhar, M. Martinho, K. K. Meier, J. R. Frisch, E. Münck, and L. Que, *Chem. Sci.*, **2014**, 5, 1204–1215.
2. K. Ray, J. England, A. T. Fiedler, M. Martinho, E. Münck, and L. Que, *Angew. Chem. Int. Ed.*, **2008**, 47, 8068–8071.
3. A. Decker, J. U. Rohde, E. J. Klinker, S. D. Wong, L. Que, E. I. Solomon, *J. Am. Chem. Soc.*, **2007**, 129, 15983–15996.
4. T. Z. H. Gani, H. J. Kulik, *ACS Catal.*, **2018**, 8, 975–986.
5. J. England, J. Prakash, M. A. Cranswick, D. Mandal, Y. Guo, E. Münck, S. Shaik, L. Que, *Inorg. Chem.*, **2015**, 54, 7828–7839.
6. K. Rydel-Ciszek, *React. Kinet. Mech. Catal.*, **2021**, 133, 579–600.
7. A. N. Biswas, M. Puri, K. K. Meier, W. N. Oloo, G. T. Rohde, E. L. Bominaar, E. Münck, L. Que, *J. Am. Chem. Soc.*, **2015**, 137, 2428–2431.
8. W. Nam, Y. M. Lee, S. Fukuzumi, *Acc. Chem. Res.*, **2014**, 47, 1146–1154.
9. J. U. Rohde, S. Torelli, X. Shan, H. L. Mi, E. J. Klinker, J. Kaizer, K. Chen, W. Nam, L. Que, *J. Am. Chem. Soc.*, **2004**, 126, 16750–16761.
10. C. V. Sastri, M. J. Park, T. Ohta, T. A. Jackson, A. Stubna, M. S. Seo, J. Lee, J. Kim, T. Kitagawa, E. Münck, L. Que, W. Nam, *J. Am. Chem. Soc.*, **2005**, 127, 12494–12495.
11. T. A. Jackson, J. U. Rohde, S. S. Mi, C. V. Sastri, R. DeHont, A. Stubna, T. Ohta, T. Kitagawa, E. Münck, W. Nam, L. Que, *J. Am. Chem. Soc.*, **2008**, 130, 12394–12407.
12. Y. Wang, K. Han, *J. Biol. Inorg. Chem.*, **2010**, 15, 351–359.
13. M. Sallmann, S. Kumar, P. Chernev, J. Nehrkorn, A. Schnegg, D. Kumar, H. Dau, C. Limberg, S. P. De Visser, *Chem. Eur. J.*, **2015**, 21, 7470–7479.
14. A. J. Johansson, M. R. A. Blomberg, P. E. M. Siegbahn, *J. Phys. Chem. C*, **2007**, 111, 12397–12406.
15. C. A. Joseph, M. J. Maroney, *Chem. Commun.*, **2007**, 12, 3338–3349.

16. J. U. Rohde, J. H. In, M. H. Lim, W. W. Brennessel, M. R. Bukowski, A. Stubna, E. Münck, W. Nam, L. Que, *Science*, **2003**, 299, 1037–1039.
17. C. Empel, S. Jana, R. M. Koenigs, *Molecules*, **2020**, 25, 4080.
18. S. P. De Visser, *J. Am. Chem. Soc.*, **2006**, 128, 15809–15818.
19. J. E. Schneider, M. K. Goetz, J. S. Anderson, *Chem. Sci.*, **2021**, 12, 4173–4183.
20. S. Taktak, M. Flook, B. M. Foxman, L. Que, E. V. Rybak-Akimova, *Chem. Commun.*, **2005**, 304, 5301–5303.
21. D. Mandal, R. Ramanan, D. Usharani, D. Janardanan, B. Wang, S. Shaik, *J. Am. Chem. Soc.*, **2015**, *137*, 722–733.
22. S. Shaik, H. Hirao, L. Que, W. Nam, *Chem. Eur. J.*, **2008**, 14, 1740–1756.
23. M. T. Green, J. H. Dawson, H. B. Gray, *Science*, **2004**, 304, 1653–1656.
24. S. T. Kleespies, W. N. Oloo, A. Mukherjee, L. Que, *Inorg. Chem.*, **2015**, 54, 5053–5064.
25. A. R. McDonald, L. Que, *Coord. Chem. Rev.*, **2013**, 257, 414–428.
26. A. Takahashi, D. Yamaki, K. Ikemura, T. Kurahashi, T. Ogura, M. Hada, H. Fujii, *Inorg. Chem.*, **2012**, 51, 7296–7305.
27. S. Hiroto, Y. Miyake, H. Shinokubo, *Chem. Rev.*, **2017**, 117, 2910–3043.
28. M. Liao, J. D. Watts, M. Huang, *J. Phys. Chem.*, **2005**, 104, 7988–8000.
29. H. Park, D. Lee, *Chem. Eur. J.*, **2020**, 26, 5916–5926.
30. R. Kumar, B. Pandey, A. Sen, M. Ansari, S. Sharma, G. Rajaraman, *Coord. Chem. Rev.*, **2020**, 419, 213397.
31. C. V. Sastri, J. Lee, K. Oh, J. L. Yoon, J. Lee, T. A. Jackson, K. Ray, H. Hirao, W. Shin, J. A. Halfen, J. Kim, L. Que, S. Shaik, W. Nam, *Proc. Natl. Acad. Sci. USA*, **2007**, 104, 19181–19186.
32. D. Kim, J. Cho, Y. M. Lee, R. Sarangi, W. Nam, *Chem. Eur. J.*, **2013**, 19, 14112–14118.
33. S. P. De Visser, R. Latifi, L. Tahsini, W. Nam, *Chem. Asian J.*, **2011**, 6, 493–504.
34. A. Katoch, D. Mandal, *Dalton Trans.*, **2022**, 51, 11641–11649.
35. Y. Zhou, X. Shan, R. Mas-Ballesté, M. R. Bukowski, A. Stubna, M. Chakrabarti, L. Slominski, J. A. Halfen, E. Münck, L. Que, *Angew. Chem. Int. Ed.*, **2008**, 47, 1896–1899.
36. J. Deutscher, P. Gerschel, K. Warm, U. Kuhlmann, S. Mebs, M. Haumann, H. Dau, P. Hildebrandt, U. P. Apfel, K. Ray, *Chem. Commun.*, **2021**, 57, 2947–2950.
37. L. Kaur, D. Mandal, *Inorg. Chem.*, **2022**, 61, 14582–14590.
38. T. Marino, M. G. Fortino, N. Russo, M. Toscano, M. E. Alberto, *Int. J. Mol. Sci.*, **2019**, 20, 3955.
39. S. Hong, H. So, H. Yoon, K. Bin Cho, Y. M. Lee, S. Fukuzumi, W. Nam, *Dalton Trans.*, **2013**, 42, 7842–7845.
40. A. D. Becke, *J. Chem. Phys.*, **1993**, 98, 1372–1377.
41. C. Lee, W. Yang, R. G. Parr, *Phys. Rev. B*, **1988**, 37, 785–789.

42. H. Chen, W. Lai, S. Shaik, *J. Phys. Chem. Lett.* **2010**, 1, 1533–1540.
43. Y. Yang, M. N. Weaver, K. M. Merz, *J. Phys. Chem. A* **2009**, 113, 9843–9851.
44. P. J. Hay, W. R. Wadt, *J. Chem. Phys.* **1985**, 82, 299–310.
45. B. D. Dunietz, M. D. Beachy, Y. Cao, D. A. Whittington, S. J. Lippard, R. A. Friesner, *J. Am. Chem. Soc.* **2000**, 122, 2828–2839.
46. J. D. Dill, J. A. Pople, *J. Chem. Phys.* **1975**, 62, 2921–2923.
47. J. Tomasi, B. Mennucci, R. Cammi, *Chem. Rev.* **2005**, 105, 2999–3093.
48. F. Weigend, R. Ahlrichs, *Phys. Chem. Chem. Phys.* **2005**, 7, 3297–3305.
49. S. Grimme, S. Ehrlich, L. Goerigk, *J. Comput. Chem.* **2011**, 32, 1456–1465.
50. D. Janardanan, D. Usharani, H. Chen, S. Shaik, *J. Phys. Chem. Lett.* **2011**, 2, 2610–2617.
51. H. P. Hratchian, H. B. Schlegel, in *Theory and Applications of Computational Chemistry: The First 40 Years* (Eds.: C. E. Dykstra, G. Frenking, K. S. Kim, G. Scuseria), Elsevier, Amsterdam, **2005**, 115, 195–249.
52. M. J. Frisch, *Gaussian 16, Revision B.01*, Gaussian, Inc., Wallingford CT **2016**.
53. G. A. Andrienko, *Chemcraft Molecular Visualization Program*, version 1.8 (build 445).
54. L. Falivene, Z. Cao, A. Petta, L. Serra, A. Poater, R. Oliva, V. Scarano, L. Cavallo, *Nat. Chem.* **2019**, 11, 872–879.
55. J. M. Mayer, *Acc. Chem. Res.* **2011**, 44, 36–46.
56. A. Sirjoosingh, S. Hammes-Schiffer, *J. Phys. Chem. A* **2011**, 115, 2367–2377.
57. D. Usharani, D. Janardanan, C. Li, S. Shaik, *Acc. Chem. Res.* **2013**, 46, 471–482.
58. C. Geng, S. Ye, F. Neese, *Angew. Chem. Int. Ed.* **2010**, 49, 5717–5720.
59. D. Janardanan, Y. Wang, P. Schyman, L. Que, S. Shaik, *Angew. Chem.* **2010**, 122, 3414–3417.
60. S. Ye, C. Y. Geng, S. Shaik, F. Neese, *Phys. Chem. Chem. Phys.* **2013**, 15, 8017–8030.
61. S. A. Wilson, J. Chen, S. Hong, Y. M. Lee, M. Clémancey, R. Garcia-Serres, T. Nomura, T. Ogura, J. M. Latour, B. Hedman, K. O. Hodgson, W. Nam, E. I. Solomon, *J. Am. Chem. Soc.* **2012**, 134, 11791–11806.
62. D. Mandal, S. Shaik, *J. Am. Chem. Soc.* **2016**, 138, 2094–2097.
63. S. Shaik, H. Chen, D. Janardanan, *Nat. Chem.* **2011**, 3, 19–27.
64. J. E. M. N. Klein, D. Mandal, W. M. Ching, D. Mallick, L. Que, S. Shaik, *J. Am. Chem. Soc.* **2017**, 139, 18705–18713.

b) Insights into C-H Activation Reactivity of Fe (IV)O Porphyrinoid Complexes: A Computational Investigation

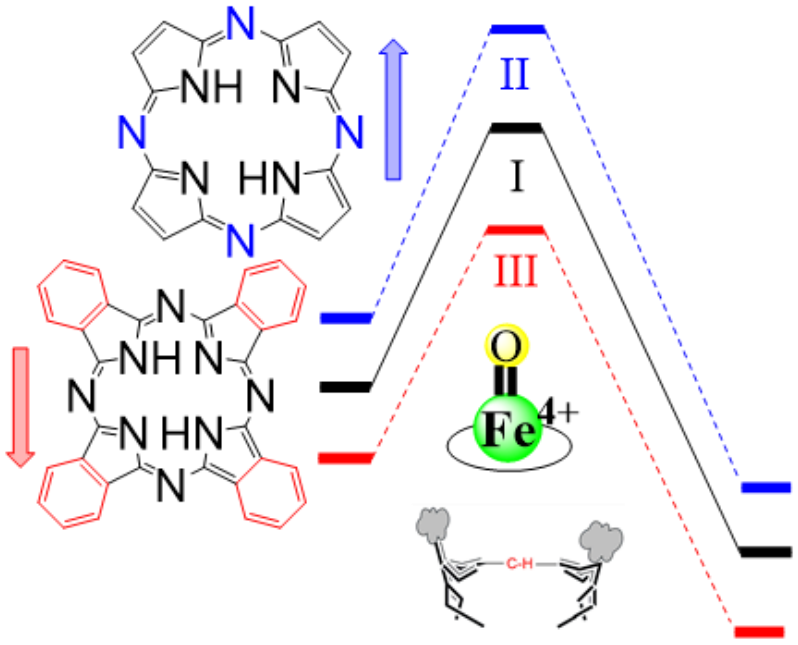

5.5 Introduction

Metalloenzymes, both heme and nonheme, have garnered significant attention within the fields of biology and chemistry owing to their ability to catalyse various oxidation reactions with high regioselectivity and stereoselectivity.[1–7] The heme iron complexes have abundant roles in nature, such as being essential for oxygen transport in mammals, and are found in structures like chlorophylls and haemoglobin, which are important for photosynthesis and oxygen transport.[8,9] Porphyrin (complex I), a macrocyclic ligand bound Fe ion in the heme enzyme, has been the subject of extensive research encompassing various scientific disciplines, including biocatalysis, photovoltaic cells, therapeutic agents, metal ligands, and many more.[10] This attention stemming from their biological importance, catalytic characteristics, and promising technological uses, as mentioned, paves the way for the need to find better alternatives that can further enhance their reactivity.[11] The C-H activation catalysed by the Fe(IV)-oxo porphyrin π cation radical, mostly known as 'compound I' in the P450 catalytic cycle, has been comprehensively explored in both experimental and computational investigations.[12,13] Various groups have thoroughly investigated the impact of changes in the ligand framework of Cpd I on its reactivity.[14–21] Several efforts have also been made to develop more reactive catalysts by modifying these complexes in various ways, such as replacing the central metal Fe with Mn or substituting the porphyrin ring with porphycene.[22] In line with this, we have initiated our investigations with the popular Fe(IV)O-porphyrin π cation radical

and extended to porphyrazine (complex II) and phthalocyanine (complex III) frameworks (presented in Scheme 5.3). These complexes differ at the equatorial level and have been the subject of theoretical comparative analysis in Fe(II) state, examining the orbitals involved.[23]

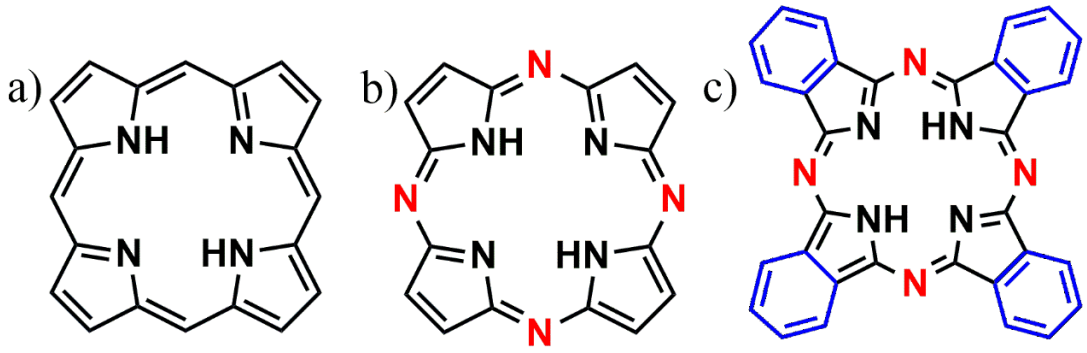

Scheme 5.3: Structures of bio inspired complexes a) Porphyrin (Complex I) b) Porphyrazine (Complex II) and c) Phthalocyanine. (Complex III)

Complex II is a direct adaptation of Complex I with nitrogen atoms in place of methine bridges. Studies have been conducted on porphyrin complexes incorporating benzene groups at the meso positions in the past, whereas such substitutions at peripheral positions have not yet been explored.[24] So, we have taken complex III into our studies with the incorporation of four benzene rings into the peripheral position of the aromatic system of complex II. The Fe(IV)OPHC π cation radical has already been synthesised and found stable[25] whereas the Fe(IV)O complex with complex II is yet to be synthesised . However, a similar complex in the Fe(III) state of complex II is available.[26] No studies on the C-H activation of these complexes have been reported so far. So, in order to understand how these modifications to the well-known porphyrin system affect the well-known HAT processes, a comprehensive DFT investigation is being conducted. The comparison of complex I with II would give us insight into the effects of hetero-substitution, and further comparison of complex II and III would reflect the effects of benzo-annulation. Chloride (Cl^-) has been chosen as the axial ligand for all the complexes to maintain consistency, as it was used in Fe(IV)O-PHC complex reported by Sorokin et al.[25] A reactivity comparison with the usual model compound I (Cpd I), which is Fe(IV)O-porphyrin π cation radical with an –SH axial ligand, has also been conducted in this study. The combination of several parameters, such as spin state, structural analysis, the study of SNO orbitals, distortion energies, and core diameters, have been considered to explain and validate our results.

5.6 Computational Details

For every species, geometry optimizations have been performed using the DFT approach, whereby the widely used B3LYP functional—three-parameter Becke's exchange with Lee-Yang and Parr's correlation functional—has been put into effect.[27,28] This functional for the C-H activation process catalysed by these kinds of complexes is supported by multiple independent studies, making it an important benchmark.[29] For the basis set, we have taken i) LANL2DZ with ECP for Fe[30] and Pople's double zeta 6-31G*[31] for all the other atoms C, H, N, O, and Cl marked as B1 for convenience.[32] The effect of acetonitrile solvent has been computed during optimization using the self-consistent reaction field, i.e., the SCRF and SMD models.[33] Further single-point calculations have also been done for energy refinement using Def2tzvpp[34] for all the atoms marked as B2. We have also implemented B2 using the same solvent model as B1. Frequency calculations, which have been done at the B1 level of theory, are highly significant for verifying the nature of the optimised structures, where one imaginary frequency represents the transition states (TS). The zero-point vibrational energy (ZPVE), as well as thermal and entropic corrections to the Gibbs free energy at T = 298K (25°C), have been evaluated for valid determination of the potential energy surface. Calculations of the intrinsic reaction coordinate (IRC) have also been performed to confirm whether the TS are connecting to the appropriate minima as needed. Kinetics calculations involve the following transition state theory eqn.[35]

$$k = \kappa\sigma \frac{k_b T}{h} \exp\left(\frac{-\Delta G^{\ddagger}}{RT}\right) \quad \text{(Eq 1)}$$

here κ and σ signify the transmission coefficient and reaction symmetry, respectively. The κ calculated here employs the 1D asymmetric Eckart method[36] The isotope effect values have been derived from the respective rate constants of H and D variants as:

$$KIE = \frac{k_H}{k_D} \quad \text{(Eq 2)}$$

Tunneling corrected barrier has been calculated with the following equation 3 where R is the universal gas constant and T is the absolute temperature.

$$\Delta\Delta E^{\ddagger}_{tun} = -RT \ln \kappa(T) \quad \text{(Eq 3)}$$

The entire DFT analysis was carried out with Gaussian 16[37] computer packages and Chemcraft software for the production and visualization of natural orbitals, respectively. We used Sambvca to determine the buried volumes.[38] For the Kinetic isotope effect and to further indulge in quantum mechanical tunneling studies Kisthelp[39] software has been used.

Unless otherwise stated, we will use the results from the B2 level of theory in all energy-related discussions.

5.7 Results and Discussions

5.7.1 Structural Parameters

Structurally, complex I differs from the other two (II and III) in having methine bridges instead of N, and it would be interesting to see how this hetero-substitution plays a part in the realm of C-H activation. Complex III further differs from II in having benzene rings attached to the main framework; however, the aza N atoms are the same in both complexes. Hence, the reactivity comparison in these would help us analyse the effects of benzo-annulation on such systems. The optimised geometries of all these three Fe(IV)O complexes along with key parameters are shown in Fig. 5.8.

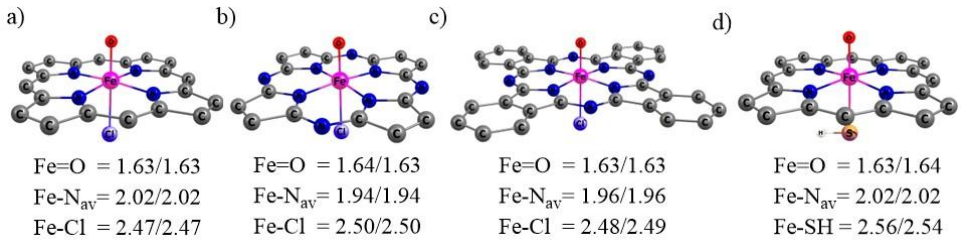

Figure 5.8: The optimised structures of oxidants with values of structural parameters for a) Complex I, b) Complex II and c) Complex III (d) Cpd I. The parameters are given as lower/higher spin state.

On reviewing the structural parameters, it was seen that there are no significant differences in the axial Fe=O and Fe-Cl bond lengths of the complexes. However, the Fe-N_{av} equatorial distances decrease slightly with the introduction of the electronegative N atom.

5.7.2 Spin States

These Fe(IV)O π cation radical complexes possesses three unpaired electrons, allowing it to exist in two low-lying spin states: doublet and quartet. The schematic presentations of the orbital diagrams are presented in the following Figure 5.9(a) In the doublet state, anti-ferromagnetically coupled unpaired electrons between the macrocycle and the iron centre result in a spin 1/2 systems. The quartet state arises when all three electrons in the system have the same spin, resulting in an overall spin 3/2 system. The macrocycle porphyrin structure typically determines the radical state of the iron(IV)-oxo porphyrin π-cation radical complex.[40] In our case, the unpaired electron is present in the a_{2u} orbital in the complex I. However, the electronegative atom at the meso position causes the radical state to be a_{1u} in the case of complex II and III as reflected in Fig. 5.9(b).

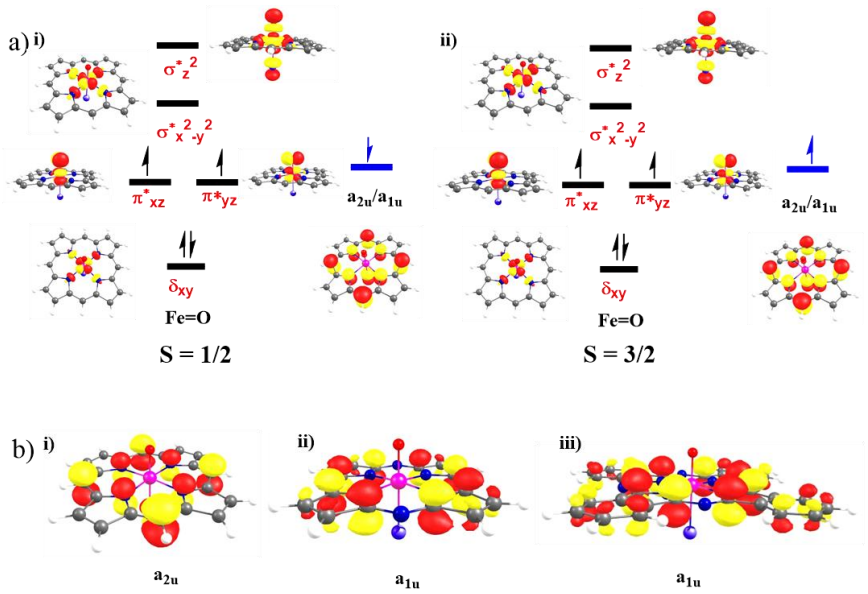

Figure 5.9 a) Valence electronic state and corresponding spin natural orbitals of the oxidants. b) radical state of i) Complex I, ii) Complex II and iii) Complex III.

As seen in Fig. 5.10, both spin states are degenerate, with the doublet state being slightly more energetically favourable.

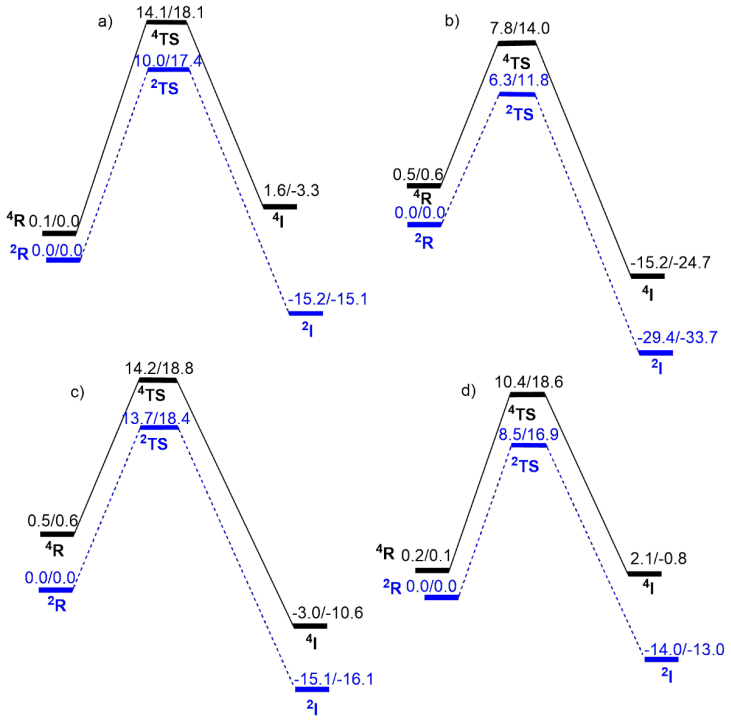

Figure 5.10: The potential energy surface for the C-H activation catalysed by a) Complex I b) II c) III and d) Cpd I. The blue and black line represents the doublet and quintet state pathways, respectively. Values are given as ΔE(B2 + ZPE)/ΔE(B1 +ZPE).

This remains consistent regardless of the axial ligand being either -Cl or -SH, as observed in comparison with compound I.[12,41] Therefore, we will mostly focus on discussing the doublet state, although the results for the quintet state are not significantly different.

5.7.3 Reactivity Pattern

Similar to earlier reports related to compound I, the low spin state is found to have slightly lower activation energy compared to the high spin states.[42] An interesting C-H activation reactivity pattern has been observed: complex II (6.3 kcal mol^{-1}) < complex I (10.0 kcal mol^{-1}) < complex III (13.7 kcal mol^{-1}), and this pattern is also seen in the quartet state. Complex II is found to be highly reactive compared to the others, even more so than the model Compound I (8.5 kcal mol^{-1}), as shown in Figure 5.10. Further details have been provided in Table 5.7.

Table 5.7: Relative energies (in kcal mol^{-1}) of oxidants, TS and intermediates computed at different levels of theory where B1 is 6-31G*/LANL2DZ(Fe) and B2 is Def2tzvpp.

Complex	Spin	Species	B1	B2
Porphine (I)	S=1/2	R+S	0.0	0.0
		TS	17.4	10.0
		IH	-15.4	-15.1
	S=3/2	R+S	0.0	0.1
		TS	18.1	14.1
		IH	-3.3	1.6
Porphyrazine (II)	S=1/2	R+S	0.0	0.0
		TS	11.8	6.3
		IH	-29.4	-33.7
	S=3/2	R+S	0.6	0.5
		TS	14.0	7.8
		IH	-24.7	-15.2
Phthalocyanine (III)	S=1/2	R+S	0.0	0.0
		TS	18.4	13.7
		IH	-15.1	-16.1
	S=3/2	R+S	0.6	0.5
		TS	18.8	14.2
		IH	-3.0	-10.6

To uncover the underlying reasons behind this reactivity pattern, we examine multiple factors in a thorough discussion as follows:

5.7.4 TS Parameters and Distortion Energy

The respective transition states for all the reactions along with key geometrical parameters have been depicted in the following Fig. 5.11.

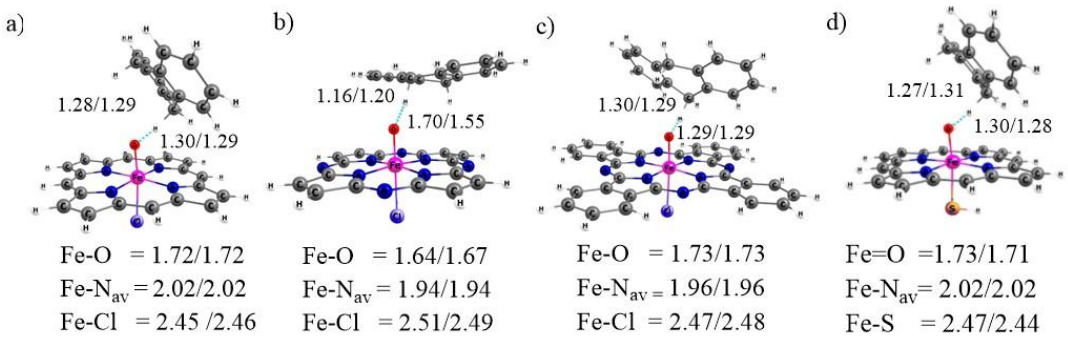

Figure 5.11: Various parameters of TS structures for a) Complex I, b) II, c) III, and d) Cpd I with bond lengths in Å for doublet/quartet.

Examining the breaking and forming bond distances, specifically the C--H and O--H bonds, in the transition state reveals a notable pattern. For complex II, a shorter C--H distance (1.16 Å) and a longer O--H distance (1.70 Å) is observed, whereas in all other cases, both distances are almost the same. Consequently, complex II has a more reactant-like transition state compared to the other three, undergoing fewer changes to reach the transition state, which results in a lower activation barrier. This is corroborated by the distortion energy values, which are lower in complex II (5.6 kcal mol^{-1}) as expected. For complexes I and III, the distortion energy values are higher, at 12.6 and 8.2 kcal mol^{-1}, respectively.

5.7.5 Nature of the electron acceptor orbital

The structure of the macrocycle largely determines the orbital to which the electron can transfer from the substrate. As seen in Figu 5.12, in complexes I and III, the incoming electron moves to the xz/yz orbital of the Fe=O moiety, leading to the formation of Fe(III)OH-Por.+.(HAT mechanism) In contrast, for complex II, the electron transfer occurs to the a_{1u} orbital of the porphyrazine ring, generating the species Fe(IV)OH-Por.(PCET mechanism). To investigate the underlying reason, we calculated the energy gaps between the involved orbitals, specifically xz/yz and a_{1u}/a_{2u}. The analysis reveals that in Complexes I and III, the energy difference between the a_{2u} and xz/yz orbitals is significantly high, at 1.21 eV and 1.52 eV, respectively. In contrast, in Complex II, the xz/yz and a_{1u} orbitals are almost degenerate, differing by only 0.15 eV. This close proximity may explain why the electron transfers into the a_{1u} orbital rather than the xz/yz orbitals.

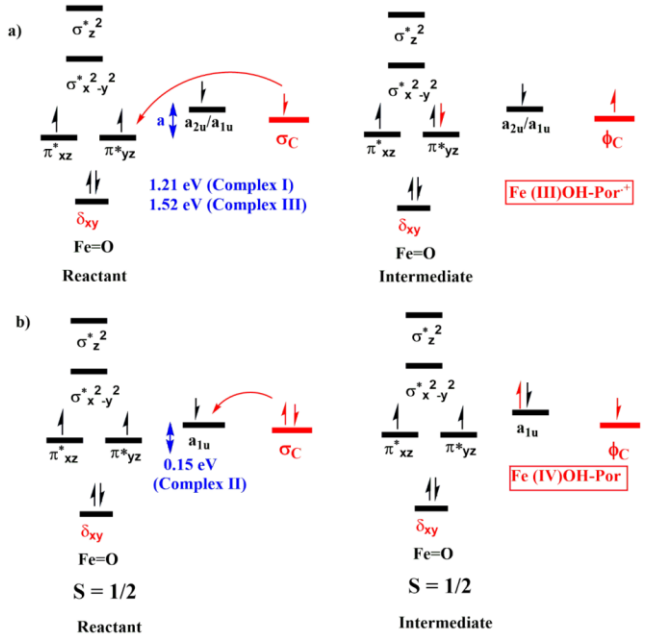

Figure 5.12: Electron transfer between the oxidant and substrate with the orbitals involved where case a) Complex I and III and b) Complex II.

The occupations in the spin natural orbitals (SNO) of the intermediates, shown in Figure 5.13, confirm this observation.

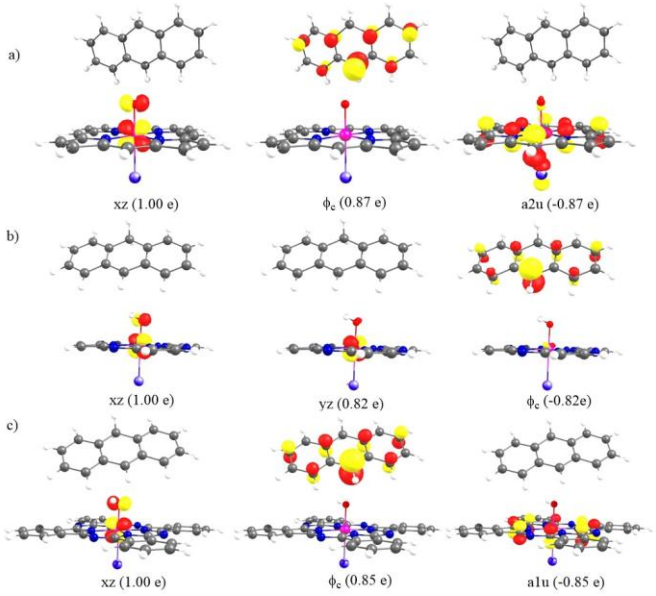

Figure 5.13: SNO plots of intermediates obtained for a) Complex I, b) Complex II, and c) Complex III.

This PCET-type electron transfer factor likely contributes to the observed pattern of reactivity. Consequently, we can conclude that C-H activation is favoured by the hetero (nitrogen) substitution at the meso position in the porphyrin ring.

5.7.6 Core size of the macrocycle

As very evident from the structure form itself the core size of the ring in complex III is more than the complex I and II. On examining the diagonal distances in the DFT optimised structures we get a value of 13.10 Å in III as opposed to just around 8.28 Å in I and II. This enlarged structure might make it difficult for the Fe=O bond to abstract the H atom and hence hinder the reactivity leading to III < I. The (percentage of buried volumes) $\%V_{bur}$ has also been calculated. These values depict the fraction of the sphere around the metal centre occupied by the ligand and were similar in the range of 82-86% in all three complexes; hence no conclusion can be drawn on this basis.

5.7.7 KIE

We were also inquisitive about how this substitution influenced quantum mechanical tunneling and if it has any role on the reactivity. Table 5.8 collects all related data of the H-abstraction reaction catalysed by all complexes at 298K.

Table 5.8: The value of imaginary frequencies, kinetic isotope effect KIE_{Wigner} and KIE_{Eckart}, ($\Delta\Delta E^{\ddagger}_{tun}$), and the effective barrier (ΔE- $\Delta\Delta E^{\ddagger}_{tun}$) for our complexes are reported herein

Complex	*v*	KIE_{Wigner}	KIE_{Eckart}	$\Delta\Delta E^{\ddagger}_{tun}$	ΔE- $\Delta\Delta E^{\ddagger}_{tun}$
I	1828*i*	9.3	119.1	3.3	14.1
II	1918*i*	6.4	19.7	2.9	8.1
III	1853*i*	9.4	154.0	3.6	14.8

Tunneling is quite prominent in Complexes I and III, as reflected by the kinetic isotope effect (KIE). Similar large, unusual KIEs have been previously reported in several Oxoiron(IV) Porphyrin Radical species[43]. In contrast, Complex II exhibits a much lower KIE, likely due to its low activation barrier and high exothermicity.[44] Even after incorporating tunneling correction, the reactivity trends remain unchanged.

From the aforementioned discussion, it is clear that replacing a carbon atom with a more electronegative nitrogen in the porphyrin significantly enhances reactivity. However, benzo-annulation on the porphyrazine diminishes this effect, making it less reactive.

5.8 Conclusions

A comprehensive DFT investigation has been presented to predict the C-H activation mechanism and reactivity pattern of a series of Fe(IV)O porphyrinoid complexes. Three complexes containing porphyrin (complex I), porphyrazine (complex II), and phthalocyanine

(complex III) frameworks with chloride as axial ligand have been selected here. The purpose of this selection is to find the effect of nitrogen atom at meso position of the porphyrin ring and further addition of aromatic ring (benzo-annulation) on pyridine on reactivity. To better understand the insight into reactivity, we turn wise studied how structural changes impacted the parameters and orbitals leading to different reactivity patterns. The results showed an exciting sequence of reactivity, i.e., complex II > complex I > complex III, depicting how more electronegative nitrogen-substitution led to an increase, whereas further benzo-annulation resulted in a decrease in the activation barriers. The reactivity of complex II is found even greater than the model Cpd I of P450 type heme-enzyme. Interestingly, complex II follows PCET type mechanism which might be the central cause behind the enhancement of the reactivity whereas the other two complexes follow HAT mechanism. It is also reflected from the structure of the transition state and distortion energies. These results also included the tunneling barriers as well. Careful analysis of the spin natural orbitals along with the determination of the ground state, which turned out to be doublet, was done. Reactivity patterns were also explored in the higher spin state, which again followed the same trend. These findings will encourage to further investigate the C-H activation chemistry of Fe(IV)O complexes with other porphyrinoid and substituted frameworks.

References

1. F. Ogliaro, M. Filatov and S. Shaik, *Eur. J. Inorg. Chem.*, **2000**, 2455–2458.
2. A. R. McDonald and L. Que, *Coord. Chem. Rev.*, **2013**, 257, 414–428.
3. L. Kaur and D. Mandal, *Dalt. Trans.*, **2024**, 53 , 7527-7535.
4. A. Katoch and D. Mandal, *Dalt. Trans.*, **2023**, 53, 2386–2394.
5. L. Kaur and D. Mandal, *Inorg. Chem.*, **2022**, 61, 14582–14590.
6. C. Krebs, D. G. Fujimori, C. T. Walsh and J. M. Bollinger, *Accounts of Chemical Research*, **2007**, 484–492.
7. N. M. DeVore, K. M. Meneely, A. G. Bart, E. S. Stephens, K. P. Battaile and E. E. Scott, *FEBS J.*, **2012**, 1621–1631.
8. A. L. Feig and S. J. Lippard, *Chem. Rev.*, **1994**, 94, 759–805.
9. G. A. F. Hendry and O. T. G. Jones, *J. Med. Genet.*, **1980**, 17, 1–14.
10. K. M. Paolesse, R, Kadish, K. M. Smith and R. Guilard, *Porphyr. Handbook. Acad. Press. Boston.*, **2000**, 2, 201–232.
11. C. C. Leznoff , A. B. P. Lever, *Phthalocyanines, Properties and Applications*, Volumes 1 - 4.
12. S. Shaik, S. Cohen, Y. Wang, H. Chen, D. Kumar and W. Thiel, *Chem. Rev*, **2010**, vol. 110.
13. J. S. Woon, O. R. Yon, R. Song and W. Nam, *J. Biol. Inorg. Chem.*, **2005**, 10, 294–304.
14. W. Nam, M. H. Lim, S. Y. Oh, J. H. Lee, H. J. Lee, S. K. Woo, C. Kim and W. Shin, *Angew. Chemie - Int. Ed.*, **2000**, 39, 3646–3649.

15. N. A. Stephenson and A. T. Bell, *Inorg. Chem.*, **2006**, 45, 2758–2766.
16. N. A. Stephenson and A. T. Bell, *J. Mol. Catal. A Chem.*, **2007**, 272, 108–117.
17. D. Kumar, G. N. Sastry and S. P. De Visser, *J. Phys. Chem. B*, **2012**, 116, 718–730.
18. H.-Y. Wang, J. Jin and M. Liu, *Artif. Intell. Chem.*, **2024**, 2, 100041.
19. Z. Ma, N. Nakatani, H. Fujii and M. Hada, *Phys. Chem. Chem. Phys.*, **2020**, 22, 12173–12179.
20. D. Mandal, D. Mallick and S. Shaik, *Acc. Chem. Res.*, **2018**, 51, 107–117.
21. T. Kamachi, T. Kouno, W. Nam and K. Yoshizawa, *J. Inorg. Biochem.*, **2006**, 100, 751–754.
22. C. Arunkumar, Y. M. Lee, J. Y. Lee, S. Fukuzumi and W. Nam, *Chem. - A Eur. J.*, **2009**, 15, 11482–11489.
23. M. S. Liao, J. D. Watts and M. J. Huang, *J. Phys. Chem. A*, **2005**, 109, 7988–8000.
24. A. Takahashi, D. Yamaki, K. Ikemura, T. Kurahashi, T. Ogura, M. Hada and H. Fujii, *Inorg. Chem.*, **2012**, 51, 7296–7305.
25. P. Afanasiev, E. V. Kudrik, F. Albrieux, V.R. Briois, O. I. Koifmanb and A. B. Sorokin, *Chem. Commun.*, **2012**, 48, 6088–90.
26. A. Theodoridis, J. Maigut, R. Puchta, E. V. Kudrik and R. Van Eldik, *Inorg. Chem.*, 2008, **47**, 2994–3013
27. A. D. Becke, *J. Chem. Phys.*, **1993**, 98, 1372–1377.
28. C. Lee, W. Yang, R. Parr, *Phys. Rev. B.*, **1998**, 785-789.
29. A. Altun, J. Breidung, F. Neese and W. Thiel, *J. Chem. Theory Comput.*, **2014**, 10, 3807–3820.
30. Y. Yang, M. N. Weaver and K. M. Merz, *J. Phys. Chem. A*, **2009**, 113, 9843–9851.
31. J.D. Dill, J.A. Pople, *J. Chem. Phys.* ,**1975**, 2921–2923.
32. P. J. Hay and W. R. Wadt, *J. Chem. Phys.*, **1985**, 82, 299–310.
33. A. V. Marenich, R. M. Olson, C. P. Kelly, C. J. Cramer and D. G. Truhlar, *J. Chem. Theory Comput.*, **2007**, 3, 2011–2033.
34. F. Weigend and R. Ahlrichs, *Phys. Chem. Chem. Phys.*, **2005**, 7, 3297–3305.
35. H. Eyring, *J. Chem. Phys*., **1935,** 3, 63–71.
36. C. Eckart, *Phys. Rev*., **1930**, 35, 1303–1309
37. Frisch, M.J. Gaussian 16, Revision B.01; Gaussian, Inc., Wallingford CT, **2016**.
38. Falivene, L. *Organometallics,* **2016**, 35, 2286–2293
39. S. Canneaux, F. Bohr, and E. Hénon , *J. Comp. Chem*., **2014,** 35**,** 82-93.
40. H. Fujii, *Coord. Chem. Rev.*, **2002**, 226, 51–60.
41. K. Bin Cho, H. Hirao, S. Shaik and W. Nam, *Chem. Soc. Rev.*, **2016**, 45, 1197–1210.
42. S. Shaik, D. Kumar, S. P. de Visser, A. Altun and W. Thiel, *Chem. Rev*, **2005**,. 105. 2279-2328.
43. Z. Pan, J. H. Horner and M. Newcomb, *J. Am. Chem. Soc*, **2008**, 130, 7776–7777.
44. R. Jaglan and D. Mandal, *Comput. Theor. Chem.*, **2020**, 1187, 112920.

Chapter 6

Conclusions and Outlooks

6.1 Conclusions

Transition metals have a wide range of applications across various fields, from materials science to medicine, due to their versatile chemistry and ability to facilitate complex reactions. Among these, iron oxo complexes stand out, particularly in the context of catalysis, as they play crucial roles in many biological processes. For instance, iron oxo species are central to the function of natural enzymes that catalyse critical reactions, such as C-H activation, which is essential for numerous biological transformations. This has led to the development of biomimetic catalysts that aim to replicate these natural processes. In our research, we have utilised density functional theory (DFT) to investigate C-H activation by iron(IV) oxo complexes, gaining insights into their reactivity and mechanism. In this field, we have concentrated on changes in ligand architecture. We explored how even slight adjustments in ligand design can profoundly impact the reaction pathways and overall efficiency. Since, most bio-inspired Fe(IV)O complexes explored to date have utilised nitrogen as the donor atom in their macrocyclic ligands. So, we have focused on substituting these nitrogen atoms with sulfur in (THC) complexes. This hetero-substitution has been shown to significantly enhance C-H activation reactivity. The increased reactivity was systematically demonstrated by a thorough analysis of the potential energy surfaces associated with the rate-determining steps of the reaction. These studies reveal a stepwise increase in reactivity, providing valuable insights into how sulfur substitution can modulate the overall catalytic activity of Fe(IV)O complexes. This approach not only broadens the scope of ligand design in bio-inspired catalysis but also offers a deeper understanding of the factors that influence reactivity in metal-oxo species. Similar studies were conducted on the well-known TMC complex, by utilising the oxygen atoms as donor atoms. These investigations revealed that modifications to the macrocycle's primary coordination sphere led to a noticeable and stepwise increase in reactivity. Next, by modifying the coordination environment of the TMC complex, we observed a notable enhancement in C-H activation reactions. Specifically, we altered the ring size of the TMC complex, varying the number of atoms in the macrocycle (n = 12-16). This adjustment resulted in a significant increase in reactivity as the ring size expanded. Interestingly, the complexes that lacked an axial ligand exhibited even lower activation energy barriers, further boosting their catalytic efficiency. This suggests that both the size of the macrocycle and the absence of an axial ligand

play critical roles in optimising the reactivity of the TMC complex, offering valuable insights for the design of more efficient catalytic systems. In the realm of heme complexes, detailed DFT studies were conducted to predict the C-H activation mechanism and reactivity of Fe(IV)O porphyrinoid complexes with porphyrin, porphyrazine, and phthalocyanine frameworks. The findings revealed that nitrogen substitution at the meso position enhances reactivity, while further benzo-annulation decreases it. These results underscore the influence of structural changes on reactivity and encourage further exploration of Fe(IV)O complexes with varied porphyrinoid frameworks. The available experimental data provided strong support for the observed reactivity patterns. This agreement between theoretical predictions and experimental results confirms the accuracy of our reactivity trends and enhances the reliability of our findings. This was further corroborated by the analysis of distortion energy, which aligned well with the trends in reactivity. Additionally, the energies of the LUMO orbitals were consistent with the predicted reactivity order. The spin densities on the oxygen atom of the ferryl group also reinforced the reactivity patterns, providing a comprehensive understanding of the factors influencing the catalytic behaviour of the complexes. This approach not only enhances our understanding of these catalytic systems but also aids in designing more efficient and selective catalysts inspired by biological systems.

6.2 Outlooks

Computations aimed at investigating the impact of ligand architecture modifications have led to the discovery of alternative metal complexes exhibiting intriguing structural and mechanistic variations. These computational insights provide a valuable foundation for guiding future experimental research and expanding our understanding of catalytic systems. Beyond the iron complexes discussed, density functional theory (DFT) calculations hold significant potential for exploring other metal frameworks, such as manganese, which has been extensively studied experimentally. Additionally, the scope of research can be broadened to include various metal-oxygen complexes, such as metal peroxo and superoxo species, provided that their stability constants are thoroughly investigated. Another promising avenue for exploration involves hetero-substitution in heme-type complexes, including porphyrin ring systems, which could be examined in both the primary and secondary coordination spheres. Such investigations could reveal further insights into the role of ligand modifications in influencing catalytic behaviour and optimising the performance of bio-inspired metal complexes.

Publications

Related to Thesis

1. L. Kaur and D. Mandal, Role of “S” Substitution on C−H Activation Reactivity of Iron (IV)−Oxo Cyclam Complexes: A Computational Investigation, *Inorg. Chem*., 2022, 61, 14582-14590. **(IF = 4.3)**
2. L. Kaur and D. Mandal, A Density Functional Theory Analysis of the C-H Activation Reactivity of Iron(IV)-Oxo complexes with 'O' Substituted Tetramethyl-cyclam Macrocycle, *Dalt. Trans*., 2024, 53, 7527-7535. **(IF = 3.5)**
3. L. Kaur and D. Mandal, Impact of Ring Size on the C-H Activation Reactivity of Iron(IV)−Oxo Complexes: A Computational Study with TMC Macrocycles, *Inorganica Chim. Acta.*, 2024, 572, 122292. **(IF = 2.7)**
4. L. Kaur and D. Mandal, Insights into C-H Activation Reactivity of Fe (IV)O Porphyrinoid Complexes: A Computational Investigation, *ChemPhysChem*.,2024. **(IF = 2.9)**

Others

1. I. Mohanta, N. Sahu, C. Guchhait, **L. Kaur**, D.Mandal, B. Adhikari, Ag+-Induced Supramolecular Polymers of Folic Acid: Reinforced by External Kosmotropic Anions Exhibiting Salting Out , *Biomacromolecules,* 2024 , 5, 6203-6215. **(IF = 5.5)**

Conferences and Workshops

1. Atomistic Modelling Workshop on Amsterdam Modelling Suite, organised by Nyro Research India, Kochi, and SCM, Netherlands, from June 07 to June 11, **2021**.
2. TCB (Theoretical Chemistry and Biology) Symposium organised by IISER Mohali on October 15, **2022**. **(Poster Presentation)**
3. International conference on Materials and Molecular Technology, organised by NIT, Kurukshetra, in April, **2023**. **(Poster Presentation)**
4. National Symposium on Theoretical Sciences by TIET, Patiala, in May, **2024**. **(Oral Presentation)**

PHD Thesis

ORIGINALITY REPORT

13%	6%	12%	1%
SIMILARITY INDEX	INTERNET SOURCES	PUBLICATIONS	STUDENT PAPERS

PRIMARY SOURCES

1	Mandal, Debasish, Rajeev Ramanan, Dandamudi Usharani, Deepa Janardanan, Binju Wang, and Sason Shaik. ""How Does Tunneling Contribute to Counterintuitive C-H Abstraction reactivity of Nonheme Fe(IV)O oxidants with alkanes?"", Journal of the American Chemical Society Publication	1%
2	Debasish Mandal, Akansha Katoch. "Impact of Carboxylate Ligation on the C-H Activation Reactivity of Non-heme Fe(IV)O Complex: A Computational Investigation", Dalton Transactions, 2024 Publication	1%
3	Debasish Mandal, Akansha Katoch. "Effect of Substituent on C-H Activation Catalysed by a nonheme Fe(IV)O Complex: A Computational Investigation of Reactivity and Hydrogen Tunneling", Dalton Transactions, 2022 Publication	1%
4	dalspace.library.dal.ca Internet Source	<1%

Dmandal